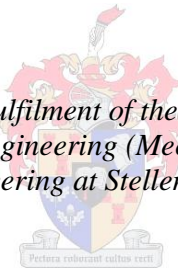


# **Numerical analysis of flow around infinite and finite cylinders at trans-critical Reynolds numbers with and without surface roughness**

by  
Abri André Spies Burger

*Thesis presented in partial fulfilment of the requirements for the degree  
of Master of Engineering (Mechanical) in the  
Faculty of Engineering at Stellenbosch University*



Supervisor: Prof. Hanno Carl Rudolf Reuter

March 2015

## **Declaration**

By submitting this thesis electronically, I declare that the entirety of the work contained therein is my own, original work, that I am the sole author thereof (save to the extent explicitly otherwise stated), that reproduction and publication thereof by Stellenbosch University will not infringe any third party rights and that I have not previously in its entirety or in part submitted it for obtaining any qualification.

Date: .....

Copyright © 2015 Stellenbosch University

All rights reserved

## Abstract

This thesis investigates the flow field and pressure distributions around cylinders at trans-critical Reynolds numbers using the  $k-\varepsilon$  Realizable turbulence model. A steady state 2-D and 3-D Fluent® model is successfully developed to evaluate the effects of changing various modelling parameters on the static pressure distribution around an infinite and finite cylinder. These parameters include surface roughness, cylinder rotation and air viscosity at the cylinder surface. The subsequent results obtained are compared to each other and to data trends from literature as well as measured experimental results and are found to be in good agreement. In addition a method for calibrating all developed methods based on their shear stress curves over a flat plate model is also successfully developed. The main objective is to find an appropriate single parameter which can be used for the rigorous adjustment of the pressure distribution around a cooling tower, which will allow for improved sensitivity analysis and modelling of cooling tower performance under wind conditions with and without meridional ribs located on the outer shell surface.

## Opsomming

Hierdie tesis ondersoek die vloeiveld en druk verdelings rondom silinders by trans-kritiese Reynolds getalle deur gebruik te maak van die  $k-\varepsilon$  Realizable turbulensie model. 'n Bestendige toestand 2-D en 3-D Fluent® model is suksesvol ontwikkel om die uitwerking van die verandering van verskeie model parameters op die statiese druk verdeling rondom 'n oneindige en eindige silinder te evalueer. Die laasgenoemde parameters sluit in oppervlak grofheid, silinder rotasie en lug viskositeit by die silinder wand. Die daaropvolgende resultate wat verkry word, word met data tendense uit die literatuur asook gemete data vanuit eksperimente vergelyk en goeie ooreenkoms i.t.v die data tendense is gevind. Verder is 'n metode vir die suksesvolle kalibrasie van die ontwikkelde numeriese tegnieke ontwikkel. Die laasgenoemde kalibrasie metode is gebaseer op die vergelyking van skuifspanning kurwes vir vloei oor 'n plat plaat model. Die hoofdoel van die navorsing is om 'n geskikte enkele parameter te vind wat gebruik kan word vir die effektiewe aanpassing van die druk verdeling rondom 'n koeltoring wat sal lei tot verbeterde sensitiviteits analise en modellering van koeltoring verrigting onder wind toestande met en sonder meridionale ribbes geleë op die buitenste dop oppervlak.

## **Acknowledgements**

I would like to thank the following people for their input and support:

- My heavenly Father for His guidance and support.
- My family and friends for their continued love and support.
- Prof. Reuter for his continued assistance, patience and guidance.

# Contents

List of Figures .....	vii
List of Tables .....	x
Nomenclature .....	xi
1 Introduction .....	1
1.1 Background .....	1
1.2 Natural draft cooling towers.....	5
1.3 Motivation .....	7
1.4 Objectives and scope.....	8
1.5 Thesis outline .....	8
2 Literature study.....	10
2.1 Investigations of flow around NDCTs .....	10
2.2 Investigations on the effect of wind ribs and surface roughness on the pressure distribution around CTs .....	11
2.3 Investigations of flow around infinite cylinders .....	13
2.4 Investigations of flow around finite cylinders .....	16
2.5 Conclusion.....	18
3 Numerical analysis of flow around an infinite cylinder .....	19
3.1 Modelling .....	19
3.1.1 Geometry, flow domain and boundary conditions.....	19
3.1.2 Mesh.....	21
3.2 Momentum adjustment procedure.....	24
3.3 Numerical results and discussion .....	24
3.3.1 Reference model compared to data from literature .....	25
3.3.2 Grid sensitivity analysis.....	28
3.3.3 Surface roughness analysis .....	32
3.3.4 Rotating cylinder analysis.....	35
3.3.5 Wall viscosity variation .....	37
3.3.6 Mesh coarsening using wall viscosity .....	38
3.3.7 Low Reynolds number modelling for the wall viscosity variation..	41
3.4 Physical modelling of ribbed surfaces .....	43
3.4.1 Flow domain and mesh .....	43
3.4.2 Results for a half cylinder with 36 ribs.....	44

3.5	Wall shear stress calibration using a flat plate model .....	47
3.6	Experimental investigation of the effect of surface roughening on pressure distribution .....	50
3.7	Conclusion.....	57
4	Numerical analysis of flow around a finite cylinder .....	59
4.1	Geometry, flow domain, boundary conditions and mesh .....	59
4.2	Pressure distribution variation along the cylinder height.....	60
4.2.1	Flow around a solid finite cylinder .....	61
4.2.2	Flow around an empty hollow finite cylinder with an inlet height..	66
4.3	Efficacy of a coarsened mesh.....	70
4.4	Effect of a non-uniform velocity profile .....	75
4.5	Conclusion.....	78
5	Conclusion and recommendations .....	80
5.1	Conclusion.....	80
5.2	Recommendations .....	81
6	References .....	83
	Appendix A: UDF for the wall viscosity technique .....	A.1
	Appendix B: 2-D CFD pressure distribution data .....	B.1
	Appendix C: Wind tunnel experiment .....	C.1
	Appendix D: Applying $k_s$ to an arbitrary mesh.....	D.1
	Appendix E: Mesh information for 3-D simulations .....	E.1
	Appendix F: Effect of using $\mu_{lam}$ instead of $k_s$ .....	F.1

## List of Figures

Figure 1.1: General $C_p$ trend with important flow variables.....	1
Figure 1.2: Airflow distortions at the tower outlet due to wind .....	4
Figure 1.3: Illustration of meridional ribs on a NDCT shell .....	4
Figure 1.4: Effect of surface roughness on: (a) Flow regimes; (b) Pressure drag ...	5
Figure 1.5: Typical HE bundle arrangements for a NDDCT .....	6
Figure 1.6: Typical fill arrangements for a NDWCT .....	6
Figure 1.7: Rugeley power plant in Great Britain .....	6
Figure 3.1: Model domain with descriptions .....	20
Figure 3.2: Region designations .....	21
Figure 3.3: Different grid types: (a) O-grid; (b) C-grid .....	22
Figure 3.4: Edges used for sizing.....	22
Figure 3.5: Meshing around the cylinder: (a) Mesh around cylinder; (b) Wall adjacent cells.....	23
Figure 3.6: Reference model $C_p$ curve for $Re = 8.4 \times 10^6$ .....	25
Figure 3.7: $C_p$ distributions: (a) Roshko (1960); (b) Störm (2010); (c) Jones (1969).....	26
Figure 3.8: Summary of $C_{p,min}$ and $C_{pb}$ values for cylinders at various Re-numbers (Güven, et al., 1980) .....	27
Figure 3.9: Results of Catalano at $Re = 1 \times 10^6$ .....	28
Figure 3.10: Boundary layer mesh detail.....	29
Figure 3.11: Radial wall element size variation .....	30
Figure 3.12: Cylinder wall division element size variation .....	30
Figure 3.13: Rough wall modelling in Fluent, Log-Law shift.....	32
Figure 3.14: Effect of surface roughness on static pressure coefficient .....	33
Figure 3.15: Variation of $C_{pb}-C_{p,min}$ and $C_d$ with increasing roughness.....	34
Figure 3.16: General pressure distribution trends with increasing roughness .....	34
Figure 3.17: Data of Zhao et al. (2012) .....	35
Figure 3.18: Effect of cylinder rotation on static pressure coefficient .....	36
Figure 3.19: Comparison between surface roughness and cylinder rotation .....	36
Figure 3.20: Effect of wall viscosity on the static pressure coefficient.....	37
Figure 3.21: Comparison of $\mu_{lam}$ method and $k_s$ method .....	38
Figure 3.22: Coarsened mesh using $\mu = 16\mu_{lam}$ .....	39
Figure 3.23: Coarsened mesh using $\mu = 16\mu_{lam}$ : $C_p$ distributions.....	40
Figure 3.24: Comparison of the coarse mesh with the refined mesh.....	41
Figure 3.25: Comparison between the SWF and the EWF.....	42
Figure 3.26: Edges used for meshing.....	43
Figure 3.27: Mesh with physical ribs: (a) Mesh surrounding the cylinder; (b) Near wall mesh .....	44
Figure 3.28: Static pressure distributions around ribbed cylinders .....	46
Figure 3.29: Comparison between physical rib and surface roughness techniques .....	47
Figure 3.30: Flow around ribbed structure: (a) Velocity vectors; (b) Control volume .....	48



Figure 3.31: $\tau_{wall}$ profiles comparison for $k_s = 1100 \mu\text{m}$ and $\mu = 70\mu_{lam}$ .....	48
Figure 3.32: $C_p$ distribution comparison ( $k_s = 1100 \mu\text{m}$ and $\mu = 70\mu_{lam}$ ).....	49
Figure 3.33: $\tau_{wall}$ curve comparison for $k_s = 60 \mu\text{m}$ and $k/a = 0.00934$ .....	49
Figure 3.34: $C_p$ distribution comparison: $\mu = 60 \mu\text{m}$ and $k/a = 0.00934$ .....	50
Figure 3.35: Sand paper roughening at $Re = 3.3 \times 10^5$ .....	52
Figure 3.36: Comparison of smooth cylinder experimental and numerical results at $Re = 3.3 \times 10^5$ .....	53
Figure 3.37: Comparison of 100 grit sand paper experimental and numerical results at $Re = 3.3 \times 10^5$ .....	54
Figure 3.38: Experimental data for ribs at $Re = 3.3 \times 10^5$ .....	55
Figure 3.39: Comparison for ribbed case at $Re = 3.3 \times 10^5$ .....	55
Figure 3.40: Calibrated rib case at $Re = 3.3 \times 10^5$ .....	56
Figure 4.1: 3-D cylinder mesh along the symmetry plane: (a) z-direction mesh edges for sizing; (b) Sample mesh .....	60
Figure 4.2: Velocity contours and vectors along the centreline of the smooth solid finite cylinder .....	61
Figure 4.3: $C_p$ distribution around a smooth solid finite cylinder .....	62
Figure 4.4: $C_p$ distribution near the smooth solid finite cylinder top end.....	63
Figure 4.5: Velocity contours of the rough ( $k_s = 500 \mu\text{m}$ ) solid finite cylinder ....	63
Figure 4.6: $C_p$ distribution around a rough ( $k_s = 500 \mu\text{m}$ ) solid finite cylinder ....	64
Figure 4.7: $C_p$ distribution near the rough solid finite cylinder tip.....	65
Figure 4.8: Velocity contours and vectors along the centreline for the smooth hollow finite cylinder .....	67
Figure 4.9: $C_p$ distribution around the smooth hollow finite cylinder .....	68
Figure 4.10: Velocity contours and vectors along the centreline for the rough hollow finite cylinder .....	69
Figure 4.11: $C_p$ distribution around a rough hollow finite cylinder.....	69
Figure 4.12: Velocity contours and vectors along the centreline for the coarse smooth hollow finite cylinder .....	71
Figure 4.13: $C_p$ distribution around a smooth hollow finite cylinder using a coarse mesh .....	72
Figure 4.14: Deviation plot for the smooth hollow finite cylinder .....	72
Figure 4.15: Velocity contours and vectors along the centreline for the coarse rough hollow finite cylinder .....	73
Figure 4.16: $C_p$ distribution around a rough hollow finite cylinder using a coarse mesh .....	74
Figure 4.17: Deviation plot for the rough hollow finite cylinder .....	75
Figure 4.18: Velocity contours and vectors along the centreline for the coarse rough hollow finite cylinder with a non-uniform velocity profile.....	76
Figure 4.19: $C_p$ distribution around a rough hollow finite cylinder using a coarse mesh with a non-uniform velocity profile .....	77
Figure 4.20: Deviation plot for the rough hollow finite cylinder with a non-uniform velocity profile .....	77
Figure C.1: Wind tunnel layout .....	C.1
Figure C.2: Mounted cylinder.....	C.2

Figure C.3: Sand paper applied to the cylinder surface .....	C.2
Figure C.4: Ribs applied to the cylinder surface .....	C.3
Figure C.5: PVC disc: (a) Disc; (b) Disc attached to the cylinder surface .....	C.3
Figure D.1: Effect of surface roughness using a coarse mesh .....	D.1
Figure E.1: Edges used for sizing: (a) x-y plane; (b) z-x plane .....	E.1
Figure F.1: Matching $C_p$ distributions for $k_s$ and $\mu_{lam}$ .....	F.1
Figure F.2: Velocity contours and vectors along the centreline for the coarse mesh using $\mu = 74 \mu_{lam}$ .....	F.2
Figure F.3: $C_p$ distribution around a rough ( $\mu = 74 \mu_{lam}$ ) hollow finite cylinder using a coarse mesh .....	F.3
Figure F.4: Deviation plot for the rough hollow finite cylinder with $\mu = 74 \mu_{lam}$ and $k_s = 500 \mu\text{m}$ .....	F.3

## List of Tables

Table 1.1: Flow regimes for smooth infinite cylinders.....	3
Table 3.1: Boundary conditions and dimensions.....	20
Table 3.2: Edge sizing and bias factors used.....	23
Table 3.3: Wake coarsening.....	31
Table 3.4: Coarse mesh using $\mu = 16\mu_{lam}$ .....	39
Table 3.5: $y^+$ range for the coarse mesh.....	40
Table 3.6: Comparison between the SWF and the EWF.....	43
Table 3.7: Roughness values investigated.....	45
Table 3.8: $k_s$ values of the sand paper grit used.....	51
Table 3.9: Rib geometry investigated.....	54
Table 4.1: Pressure drag coefficients at various cylinder heights.....	66
Table B.1: Smooth cylinder data.....	B.1
Table B.2: Rough cylinder data; $k_s = 500\mu m$ .....	B.3
Table B.3: Rough cylinder data; angular velocity of 275 rad/sec.....	B.6
Table B.4: Rough cylinder data; $\mu = 72\mu_{lam}$ .....	B.8
Table C.1: Wind tunnel dimensions.....	C.1
Table C.2: Rib geometries investigated.....	C.4
Table C.3: Data for ribbed cases and smooth case with paper, $Re = 3.3 \times 10^5$ ...	C.5
Table C.4: Data for sand paper and smooth case, $Re = 3.3 \times 10^5$ .....	C.6
Table C.5: Data for sand paper and smooth case, $Re = 4.3 \times 10^5$ .....	C.7
Table D.1: Coarse mesh edge sizings.....	D.1
Table E.1: Domain sizing for solid finite cylinder.....	E.2
Table E.2: Mesh edge sizing for solid finite cylinder.....	E.2
Table E.3: Domain sizing for hollow finite cylinder with an inlet height, fine mesh.....	E.3
Table E.4: Mesh edge sizing for hollow finite cylinder with an inlet height, fine mesh.....	E.3
Table E.5: Domain sizing for hollow finite cylinder with an inlet height, coarse mesh.....	E.4
Table E.6: Mesh edge sizing for hollow finite cylinder with an inlet height, coarse mesh.....	E.4

## Nomenclature

$a$	Rib spacing	[m] or [°]
$b$	Rib width	[m]
$C_d$	Pressure drag coefficient	
$C_p$	Static pressure coefficient	
$C_{p,min}$	Minimum pressure coefficient	
$C_{pb}$	Wake pressure coefficient	
$d$ or $D$	Diameter	[m]
$h$	Cylinder height	[m]
$k$	Rib height	[m]
$k_s$	Equivalent sand grain roughness	[ $\mu\text{m}$ ]
$P$	Static pressure	[Pa]
$V$	Velocity	[m/s]
$x$	Distance from plate leading edge	[m]

## Greek symbols

$\epsilon$	Surface roughness	
$\mu$	Dynamic viscosity	[kg/ms] or [Pa·s]
$\rho$	Density	[kg/m <sup>3</sup> ]
$\tau$	Shear stress	[Pa]
$\varphi$	Angle	[°]

**Dimensionless groups**

$Ma$	Mach number	$\frac{V}{V_{sound}}$
$Re_D$	Reynolds number for a cylinder	$\frac{\rho_{ref} V_{ref} D}{\mu_{ref}}$
$Re_x$	Reynolds number for a flat plate	$\frac{\rho_{ref} V_{ref} x}{\mu_{ref}}$

**Subscripts**

BL	Boundary Layer
CFD	Computational Fluid Dynamics
CT	Cooling Tower
HE	Heat Exchanger
NDCT	Natural draft cooling tower
RANS	Reynolds Averaged Navier-Stokes
Ref	Reference condition
RS	Radial section
T	Turbulent
UDF	User defined function

# 1 Introduction

Cylindrical structures are frequently encountered in the engineering practice. Some commonly encountered examples include wind turbine towers, central receiver towers, smoke stacks, natural draft cooling towers (NDCTs) and solar chimneys. An understanding of the pressure-distributions and -loads acting in on these structures are of paramount importance for effective and efficient structural, thermal and aerodynamic design.

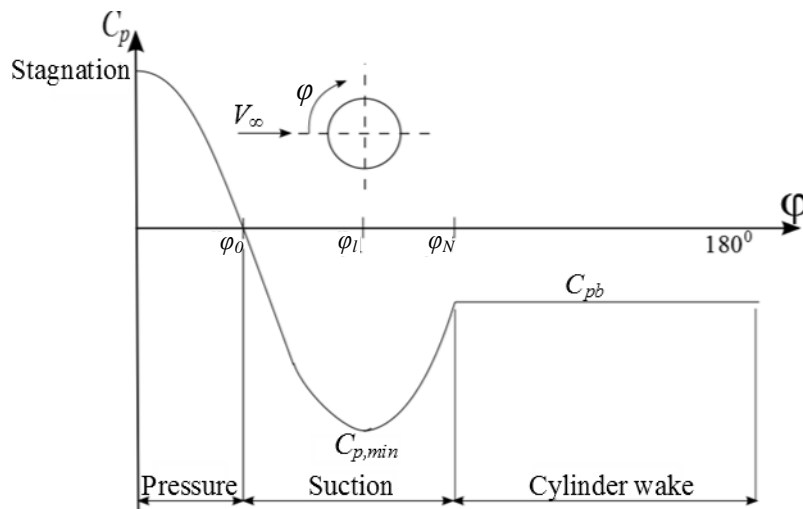
## 1.1 Background

Research has shown that external factors such as wind have a significant effect on both the pressure load and distribution around NDCTs.

In order to gain better insight into the effect wind has on the flow field around a cylindrical structure consider a typical static pressure distribution around the cylinder periphery (Figure 1.1) where the static pressure coefficient ( $C_p$ ) is defined as follows:

$$C_p = \frac{P - P_\infty}{0.5\rho V_\infty^2} \quad (1.1)$$

In equation (1.1),  $P$  represents the local static pressure at the cylinder wall and the remaining variables refer to the ambient conditions far from the cylinder.



**Figure 1.1: General  $C_p$  trend with important flow variables**

When airflow reaches the windward side of the cylinder it is forced to a complete stop, referred to as the stagnation point, where after the flow redirects and starts to accelerate along the cylinder wall. As the air flows along the cylinder periphery a viscous boundary layer (which can be laminar, turbulent or transitional) is formed due to the no-slip condition, which causes air to stick to the cylinder wall. During the acceleration span, the point of zero pressure ( $\phi_0$ ) is encountered and the

airflow eventually reaches the maximum suction pressure ( $C_{p,min}$ ) at an angle of  $\phi_l$ . The increase in suction pressure can be explained by considering the Bernoulli equation, according to which, accelerating flow causes the static pressure of a fluid to decrease or conversely a decelerating flow causes the static pressure to increase. It should be kept in mind that the Bernoulli equation is only valid for the external inviscid flow region, however, the external pressure field is impressed on the boundary layer (Schlichting, 1979). Once  $C_{p,min}$  is reached, the airflow has inadequate energy left, due to large frictional forces encountered in the boundary layer, to climb the “pressure hill” and starts to decelerate until the flow is forced to stop and change direction which results in flow separation at  $\phi_N$ . After the point of separation, the eddying wake region is encountered, characterized by the fairly constant wake pressure ( $C_{pb}$ ) which causes considerable suction behind the cylinder resulting in large pressure drag forces experienced by the structure. Changes in wind velocity can thus affect the maximum suction pressures on the side of a cylindrical structure as well as the flow separation point which leads to a change in the  $C_p$  distribution curve and subsequently the flow field around the structure. In addition changes in wind velocity also affect the Reynolds ( $Re$ ) regime and subsequently whether the boundary layer state is laminar, turbulent or a combination of the two.

The  $Re$  number is a dimensionless parameter used in fluid dynamics to determine whether viscous forces or inertial forces dominate the flow. The mathematical definition of the  $Re$  used to determine the state of a boundary layer is defined as stated in equation (1.2) where  $x$  represents the distance from the leading edge,  $\rho$  the density of the fluid,  $V$  the velocity of the fluid and  $\mu$  the fluid viscosity.

$$Re = \frac{\rho V x}{\mu} \quad (1.2)$$

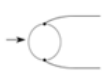
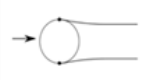



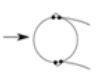

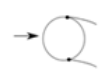
From this definition it can be seen that it relates the magnitude of inertial forces ( $\rho V x$ ) to the magnitude of viscous forces ( $\mu$ ). When the  $Re$  is sufficiently small ( $Re < 1 \times 10^5$ ) it can be assumed that the flow is dominated by viscous forces and the flow is labelled as laminar flow (Cengel and Cimbala, 2010). Alternatively when the  $Re$  is sufficiently large ( $Re > 3 \times 10^6$ ) the flow is dominated by inertial forces, with turbulent eddies present in the flow, and is therefore termed turbulent flow (Cengel and Cimbala, 2010). Furthermore, the boundary layer does not instantaneously change from a laminar to a turbulent state and subsequently there is another region termed transitional flow. However due to the difficulty in predicting how the boundary layer reacts in the latter region it is largely avoided. In general when a transition from laminar to turbulent conditions occurs, additional energy is gained by turbulent momentum exchange. This additional energy results in a larger capability to overcome the adverse pressure gradient behind the pressure minimum and results in the flow separation point shifting further downstream creating a wake region with a smaller width and subsequently smaller pressure drag force.

According to Achenbach (Achenbach in Niemann and Hölscher (1990)) four flow regimes can be defined based on the  $Re$  definition for flow around a circular cylinder, which is similar to equation (1.2) with  $x$  replaced by the cylinder diameter  $D$ :

1. Sub-critical
2. Critical
3. Super-critical
4. Trans-critical

Table 1.1 shows a summary of the above mentioned regimes with corresponding  $Re$  ranges and general characteristics such as pressure drag coefficient as well as the state of the boundary layer.

**Table 1.1: Flow regimes for smooth infinite cylinders (Niemann and Hölscher, 1990)**

	Subcritical	Critical (crit)				Supercrit	Upper transition	Trans critical
Regime region	1	2	3	4	5	6	7	8
BL state	Stable		Unstable	Bi-stable	Unstable	Stable	Unstable	Stable
$Re \times 10^5$	1.4		2.8	3.0	3.3	3.5	10	50
Mean $C_d$	1.2	1.2-1	1.0-0.7	0.5	0.5-0.4	0.22	0.22-0.52	0.5-0.85
Mean $C_L$	0			$\pm 1.3$	1.3-0.9	0	0.1-0.2	0.5
St	0.2			0.33	0.31	0.48	(0.1/0.45)	0.28
BL separation								
Separation type	Laminar	Laminar	Random	1-sided separation bubble	Random	2-sided separation bubble	Random	Turbulent

In the sub-critical regime viscous forces dominate the flow and only a laminar boundary layer is present up to the point of flow separation at approximately  $70^\circ - 80^\circ$  (Niemann and Hölscher, 1990), as measured from the windward stagnation point of the cylinder. At  $Re = 1.4 \times 10^5$  the flow enters the critical regime in which the laminar boundary layer slowly becomes unstable, due to larger inertial forces present, and eventually has a transition from a laminar boundary layer to a turbulent boundary layer. This transition can be observed experimentally and is characterized by a separation bubble in which the laminar boundary layer separates, closely followed by turbulent re-attachment of the flow.

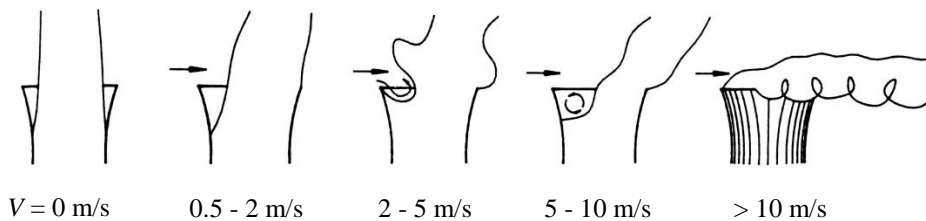
In short the laminar boundary layer breaks down and transitions to a turbulent boundary layer which now contains added energy to overcome the adverse pressure gradient along the cylinder circumference. The latter results in delayed flow separation points which in turn yield smaller wake regions and subsequently



lower pressure drag forces on the cylinder. In fact this regime extends to approximately  $Re = 3.5 \times 10^5$  which is defined as the point of lowest pressure drag (Niemann and Hölscher, 1990).

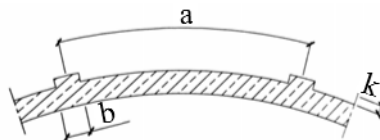
In the range  $3.5 \times 10^5 < Re < 1 \times 10^6$  the flow is classified as super-critical. This regime is characterized by low drag coefficients with double sided separation bubbles resulting in delayed separation points in the region of  $140^\circ$  (Niemann & Hölscher, 1990). In the upper transition region the point at which the laminar boundary layer transitions to a turbulent one shifts upstream until it is in the vicinity of the windward stagnation point. Once the latter is reached the flow is said to be in the trans-critical regime and now has an earlier separation point around  $110^\circ$  due to larger frictional losses experienced by the flow (Niemann & Hölscher, 1990). This earlier separation point also results in larger pressure drag forces on the cylinder.

Furthermore at the outlet of NDCTs the airflow distortions due to wind result in recirculation of the thermal plume, as shown in Figure 1.2, due to leading edge separation which can reduce thermal performance. In addition since wind can alter the wake region of the flow field due to changes in the flow separation point the path of a thermal plume is also negatively impacted.



**Figure 1.2: Airflow distortions at the tower outlet due to wind (Kröger, 2004)**

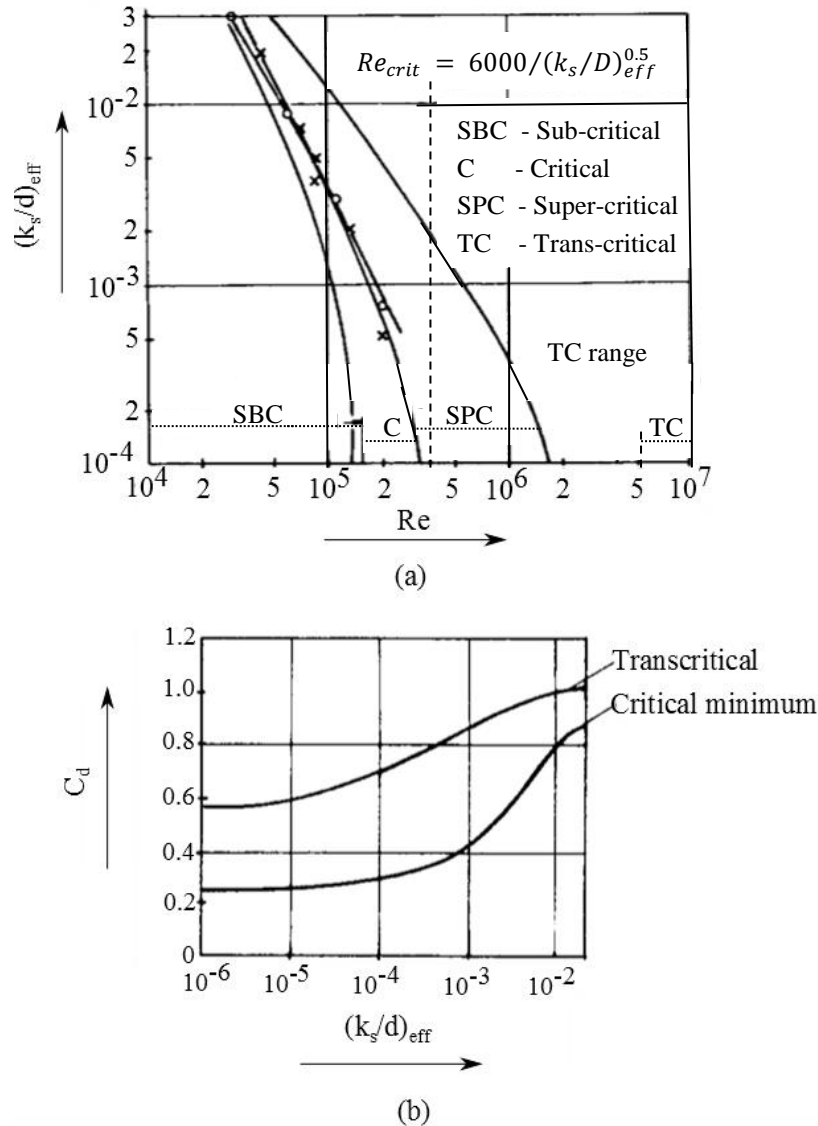
In order to strengthen cylindrical structures and reduce the large suction pressures in the presence of wind, meridional ribs (also referred to as wind ribs) are employed as shown in Figure 1.3 (Niemann, 1971). The presence of wind ribs effectively creates a larger flow resistance at the wall resulting in relieved suction pressures ( $C_{p,min}$ ) due to increased flow resistance at the wall as well as earlier flow separation angles ( $\phi_N$ ) resulting in larger pressure drag forces on the structure.



**Figure 1.3: Illustration of meridional ribs on a NDCT shell**

In general when surface roughening is applied, effectively resulting in increased flow resistance, the  $Re$  regime boundaries shift to lower  $Re$  numbers as shown in Figure 1.4 (a) below. This implies that theoretically surface roughness can be used

to simulate high  $Re$  regimes at flow conditions with lower  $Re$  numbers. Furthermore it has also been documented in literature that increasing surface roughness leads to increased critical and trans-critical pressure drag values as shown in Figure 1.4 (b).

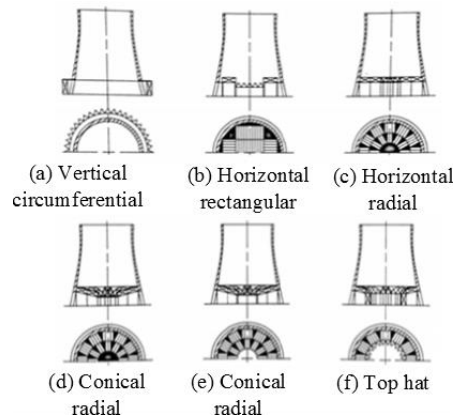


**Figure 1.4: Effect of surface roughness on: (a) Flow regimes; (b) Pressure drag (Niemann and Hölscher, 1990)**

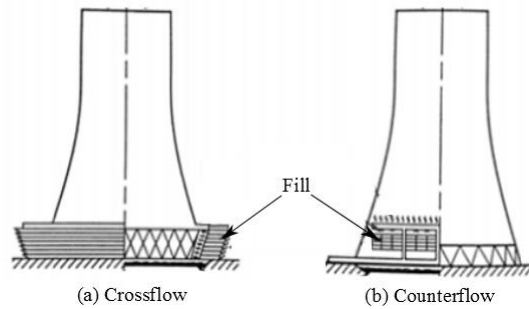
## 1.2 Natural draft cooling towers

NDCTs are large structures designed to remove “waste” heat from water such that the fluid can be reused to absorb heat elsewhere in the cooling system. Numerous types of cooling tower designs exist including natural draft wet- and dry-cooling towers which utilize various fill and heat exchanger (HE) bundle arrangements,

respectively. Typical HE bundle and fill arrangements found in NDCTs are shown in Figure 1.5 and Figure 1.6, respectively.

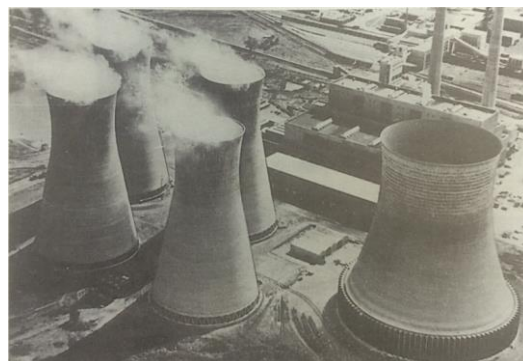


**Figure 1.5: Typical HE bundle arrangements for a NDDCT (Kröger, 2004)**



**Figure 1.6: Typical fill arrangements for a NDWCT (Kröger, 2004)**

Furthermore Figure 1.7 shows images of wet (left) and dry (right) NDCTs at the Rugeley power plant. Although the size of the towers can differ substantially, the base operation and functioning of both the wet and dry NDCT are similar. The main difference is that in wet towers heat is transferred through the combined processes of heat and mass transfer through spraying of water directly onto fills and allowing air to pass over these fills to cool the water by evaporation.



**Figure 1.7: Rugeley power plant in Great Britain (Kröger, 2004)**

Alternatively dry towers reject heat solely through convection heat transfer by passing the water through HE bundles and then through allowing air to flow across these bundles to cool the water. In both the above NDCT configurations the atmosphere is utilized as the heat sink and airflow is affected by means of natural draft through buoyancy effects.

In thermal power plants employing NDDCTs with HE bundles wet steam from the turbine exhaust is routed to a surface or shell-and-tube condenser where the steam is condensed to a liquid phase and then pumped back to the boiler. During condensation of the steam, latent heat is transferred to the secondary cooling water circulation loop passing through the condenser. The heated cooling water in this secondary loop is then pumped to the cooling tower where it flows through the HE bundle tubes. Sensible heat is then transferred from the cooling water to the airstream through convection heat transfer and the cooled water is again circulated through the condenser repeating the cycle.

However, in the case of a Heller system steam from the turbine exhaust is condensed in a direct contact jet condenser and pumped to a NDCT with vertically arranged HE bundles such that the condensate can be cooled and pumped back to the boiler to repeat the cycle.

In the case of a NDWCT wet steam from the turbine exhaust is routed to the condenser where the steam is condensed to a liquid phase and pumped back to the boiler. During condensation of the steam latent heat is transferred to the secondary cooling water circulation loop passing through the condenser. The heated cooling water in this secondary loop is then pumped to the cooling tower where it is sprayed onto fills. Heat is then transferred from the cooling water to the airstream through the combined processes of convection heat transfer and mass transfer. The cooled water falls through the spray, fill and rain zones under gravity before it is then collected at the base of the cooling tower in a pond and circulated back to the condenser repeating the cycle.

### **1.3 Motivation**

At present there exists a growing demand for efficient power generation throughout the world. With the increasing demand for water supplies leading to increased water cost, rapid increase in population leading to available land scarcity, dwindling supplies of fossil fuels, global warming and tendency towards more sustainable energy systems the need for efficiency has never been more critical. Traditionally the main focus for improvement was on the boiler and turbine of the system although more recently attention is being shifted towards the cooling end of the system where ample room for efficiency improvement may yet be uncovered. This is reflected in, mainly, the increasing numerical studies involving the computational fluid dynamic (CFD) modelling of cooling towers and the investigation of the effect of external factors such as CT support structures

located at the tower inlet, shape of the CT structure, effect of cross-winds and the effect of wind break walls on CT performance.

Airflow around and through cooling towers is one of the main parameters that drive the effectiveness of the heat transfer between the cooling water and atmospheric air. Wind is known to significantly reduce the thermal performance of natural draft cooling towers as it causes flow separation and recirculation at the tower outlet as well as uneven pressure distributions around the tower which disturbs the air flow patterns around the tower periphery as well as the wake behaviour behind the tower. Better computational fluid dynamics (CFD) performance models can help to improve CT designs for performance enhancement and life cycle cost reduction through effective parametric studies.

This research will provide better understanding and insight into airflow patterns and specifically pressure distributions around cylindrical structures which will subsequently contribute to improved CT designs, improved efficiency of current CTs, and possibly reduced life cycle costs.

## **1.4 Objectives and scope**

In order to develop a validated and improved CFD model to investigate airflow patterns and pressure distributions due to the effect of CT parameters such as meridional ribs on static pressure distribution the objectives for this thesis are to:

1. Develop a two dimensional (2-D) and three dimensional (3-D) CFD model to simulate and study airflow patterns and pressure distributions around infinite and finite cylinders with different surface roughness's.
2. Use numerical experiments to identify an adequate momentum source(s) term in order to incorporate the effect of structural ribs and surface roughness on the pressure distribution around a cylinder with reduced computational cost.
3. Perform a sensitivity analysis on the infinite and finite cylinder model in order to investigate the effect of different parameters on the static pressure distribution along the cylinder height.
4. Conduct experiments in a wind tunnel to compare experimental data to numerical data obtained for different surface roughness profiles.
5. Use measured experimental results to validate the effect roughness techniques have on pressure distributions and use the developed CFD models to determine what can be adjusted such that results correlate better.

## **1.5 Thesis outline**

### **Chapter 1: Introduction**

An introduction about the research and a brief background on the basic functioning of NDCTs is discussed. The motivation, objectives and summary of the thesis layout are provided.

## **Chapter 2: Literature review**

A literature review on past and current numerical and experimental investigations of CTs and cylinders is presented. This includes modelling techniques for cylinders and CTs, the effect wind has on CT performance, effect of wind ribs on the pressure distribution around CT structures, and the effect of surface roughening on cylinder pressure distribution.

## **Chapter 3: Numerical analysis of flow around an infinite cylinder**

A 2-D CFD model is developed in order to investigate the flow around an infinite cylinder at trans-critical Reynolds numbers. Various adjustments are made to the flow and mesh conditions and observations are discussed with respect to the effect they have on the static pressure distribution around the cylinder. In addition a CFD model incorporating physical ribs is developed and the practicality thereof discussed. Furthermore, a flat plate CFD model is developed which is used to calibrate wall shear models such that, for a set of variables, similar pressure distributions are generated. Lastly measured experimental results are also presented and discussed.

## **Chapter 4: Numerical analysis of flow around a finite cylinder**

A 3-D CFD model for a finite cylinder is developed using the principles in Chapter 3 in order to investigate the flow around a finite cylinder. The effects of height to diameter ratio are investigated with respect to the variation of static pressure distribution measured at various heights along the cylinder. In addition the effect of surface roughening as well as inlet height at the cylinder base is investigated. Furthermore the efficacy of using a drastically coarsened mesh to model the flow patterns is investigated. Lastly the effect of a power law wind profile, as opposed to a uniform wind profile, is investigated using the coarsened mesh.

## **Chapter 5: Conclusion and recommendations**

A brief overview of the work done as well as recommendations are provided.

## 2 Literature study

This section discusses previous work done by other researchers in the field of CT and cylinder modelling. The methods used are presented and the main findings summarized.

### 2.1 Investigations of flow around NDCTs

Du Preez and Kröger (1995) investigated the effect of cross winds by means of full scale measurements as well as numerically investigating the effect of windbreak walls on the performance of a NDDCT with horizontal and vertical heat exchanger (HE) bundle arrangements using the PHOENICS® CFD software. A non-uniform power law wind profile with an exponent of 0.16 was used as the velocity inlet condition. The study concluded that the addition of windbreak walls reduce the adverse effect of cross winds and made suggestions concerning both HE bundle and windbreak wall arrangements. In addition during the same period Wei et al. (1995) studied the unfavourable effects of wind on the cooling performance of NDDCTs. The study involved conducting full scale measurements on a CT as well as testing a wind tunnel model of a NDDCT with vertically arranged HE bundles. The study concluded that wind does indeed lower the performance of dry CTs due to, respectively, the unfavourable pressure distribution at the tower inlet, disruption of the hot plume rising from the CT outlet, and back flow of air at the tower outlet due to leading edge separation.

Furthermore Su et al. (1999) numerically simulated the fluid flow and temperature distribution of a dry-cooling tower with vertical HE bundles in 3-D using the finite volume method and  $k-\varepsilon$  turbulence model. The numerical domain simulated considered half the CT geometry through the use of a symmetry boundary condition. The results were verified by comparing full scale CT measurements to the numerical results and noting that the data compared satisfactory. The study concluded that under cross winds the air flow around the tower resembles that of the flow around a circular cylinder, with low pressure zones experienced on the tower sides resulting in almost no air entering the tower from these zones. Furthermore as the cross wind speed increased it resulted in an unfavourable secondary flow inside the tower decreasing tower performance.

More recently Al-Waked et al. (2004) performed a computational fluid dynamics (CFD) study on the effect of windbreak walls on the performance of NDDCTs with horizontally arranged HE bundles under cross winds (power law exponent used was 0.2). They used the Fluent® CFD software package and generated a 3-D model using the standard  $k-\varepsilon$  turbulence model. The results indicated that cross winds could lead to a decrease in performance of up to 30% for wind speed higher than 10 m/s measured at 10 m above ground level. In addition it was found that by the introduction of windbreak walls the adverse effects of cross winds can be reduced by up to 25%. Furthermore a parametric study was conducted to examine



the effect of cross wind power law profile on tower performance and it was found that representing the cross wind profile accurately has a significant effect on the thermal characteristics of a NDDCT where low wind velocities are concerned. Al-Waked also extended the study in order to quantify the cross wind effect on natural draft wet cooling tower (NDWCT) performance where he found that at velocities lower than 7.5 m/s the CT performance is reduced however at higher velocities the performance was actually enhanced (Al-Waked and Behnia, 2006).

Lu et al. (2013) studied the effect of using windbreak walls in a short NDDCT with horizontally arranged HE bundles with the use of a power law velocity profile with an exponent of 0.2. The investigation was carried out by developing a CFD model for the CT using Fluent® and concluded that by adding windbreak walls the negative effect of cross winds can be greatly reduced and can even be reversed into an enhancement tool for NDDCT performance. However it should be noted that the tower shell used in the study is cylindrical and not hyperbolic and the total tower height is limited to 15 m which is extremely small considering that CTs can reach heights of 200 m and more.

Furthermore Yang et al. (2013) investigated the thermo-flow performance of an indirect dry cooling system in a power plant. In the study they developed a CFD model using Fluent® and used a power law velocity profile with an exponent of 0.2. The CT simulated was a NDDCT with vertically arranged HE bundles. In addition they also included the flue stack situated in the centre of the tower as well as the surrounding turbine- and boiler-houses. The study found that at low wind velocities (below 12 m/s) the performance of the CT is decreased partly due to the low pressure zones forming at the sides of the tower resulting in little to almost no air flowing over these HE bundles. However at high wind velocities (above 12 m/s) the negative effect of wind can be reduced due to the large pressure difference created between the inlet and outlet of the tower forcing more air to flow through the tower.

## **2.2 Investigations on the effect of wind ribs and surface roughness on the pressure distribution around CTs**

Goudarzi and Sabbagh-Yazdi (2008) conducted a case study of wind effects on a CT in Iran using an unstructured mesh and ANSYS FLOTTRAN to investigate wind induced pressure load on a single CT. In their simulations the authors attempted to incorporate the effect of meridional wind ribs through the use of a surface roughness model which uses an equivalent sand grain roughness as roughness parameter. The data gathered from the CFD program was then compared to data generated by VGB (German guideline for CT design) code. The subsequent increase of surface roughness in the CFD model followed a trend of subsequently lower suction pressures on the sides of the CT. However the CFD results did have large discrepancies when compared to the VGB code when looking at the flow separation point and position of maximum suction. The pressure distribution trends of the CFD results and VGB code on the other hand



were similar. The discrepancy between results was suspected to be due to the VGB code using the coefficient of pressure for cylindrical towers whereas their model used a hyperbolic CT shape. In addition the fact that they did not consider airflow through the tower could have resulted in inaccurate modelling.

The above mentioned results are in agreement with research documented by Niemann and Hölscher (1990) which covers the effects of surface roughness on cylinders as well as the effect of ribs on CT pressure distribution. In short it was found that by increasing the surface roughness the trans-critical and critical drag of a cylinder increases, effectively increasing the wake behind the cylinder which corresponds to earlier flow separation. In addition to the latter the authors state that a higher drag correlates with a lower vortex shedding frequency. Furthermore it was shown that through the use of vertical ribs on CT structures a similar effect to surface roughness could be obtained along with a more favourable pressure distribution on the CT circumference which may reduce wind induced stresses on the tower shell.

Störm (2010) investigated the flow in and around a natural draft cooling tower (NDCT) by means of a CFD simulation using Fluent®. His study included the development of a CFD model which could predict the airflow patterns and pressure distribution around a circular cylinder reaching Reynolds numbers in excess of  $Re = 1 \times 10^7$ . The study focused on the evaluation of effects including the boundary layer mesh size and type, turbulence model used, mesh refinement, surface roughness effect on surface pressure distribution as well as pressure and velocity profiles in the wake region. The study found that the  $k-\varepsilon$  Realizable turbulence model is the most suitable method for the turbulence modelling since it resulted in adequate accuracy with a reasonable simulation time. In addition Störm found that grid refinement at the boundary layer and wake region effect the pressure distribution calculated on the surface of a cylinder and that the boundary layer mesh must be extended at least a distance  $D/3$  away from the cylinder in order to obtain accurate results.

Zhao et al. (2012) performed wind tunnel tests on a rigid 1:200 scale model of a hyperbolic cooling tower with the aim of investigating the effect of surface roughness on the pressure distribution around the tower. Surface roughness was modelled through the use of vertical ribs consisting of paper tape or thread. Roughness was varied by changing the spacing, height, thickness and number of layers (in the case of the tape) of the vertical ribs. Furthermore the experiments were conducted with both uniform and non-uniform velocity profiles. In addition measurements were taken at the throat of the model in order to avoid end effects at the tower outlet. They found that the impact of surface relative roughness, with regards to average pressure distribution around the tower, for the uniform and non-uniform velocity profiles were similar. It was observed that with the increase of relative surface roughness there is a consequent decrease in the angle at which the lowest pressure occurs as well as an increase in this pressure. Furthermore in the wake area there is a trend of gradual increase of the wake pressure as the

relative roughness is increased. In addition it was found that with increasing roughness flow separation occurs at an earlier angle which is consistent with data documented by Niemann (Niemann and Hölscher, 1990). The study showed that through the use of surface roughness the flow patterns around a cooling tower can be altered and that higher Reynolds numbers can be simulated under the condition of relatively low Reynolds number through the use of surface roughness.

### 2.3 Investigations of flow around infinite cylinders

Roshko (1960) conducted experiments on a large cylinder in a pressurized wind tunnel reaching a maximum  $Re = 8.4 \times 10^6$  which falls into the trans-critical regime. The main objective of the study was to investigate flow patterns around circular cylinders in order to better understand the flow dynamics. In the experimental setup pressure was measured along one half of the cylinder with a splitter plate attached in the cylinder wake region. It was found that the use of the splitter plate lead to the suppression of vortex shedding and had no significant effect on the pressure distribution around the cylinder. However some changes in the base pressure and cylinder drag were observed. The study concluded with suggested ideas on the flow around cylinders and showed that through the use of a splitter plate in the cylinder wake the flow can be changed from one with alternating shedding to a steady symmetrical flow with suppressed vortex shedding.

Achenbach (1968) investigated the distribution of local pressure and skin friction around smooth circular cylinders in a pressurized wind tunnel within the  $Re$ -range of  $6 \times 10^4 < Re < 5 \times 10^6$ . The flow was considered to be steady and results indicated that the pressure distribution around cylinders is sometimes unsymmetrical. Furthermore from the results three distinct flow regimes could be distinguished: sub-critical, critical and super-critical. In addition results showed that skin friction has a relatively low contribution toward total drag around the cylinder with the percentage of skin friction over total drag ranging between  $C_{d,f} = 0.5\% - 2.5\%$  for  $6 \times 10^4 < Re < 5 \times 10^6$ .

Jones et al. (1969) conducted wind tunnel experiments on a stationary and oscillating circular cylinder in 2-D flow at  $0.36 \times 10^6 < Re < 18.70 \times 10^6$  and Mach numbers of  $0.05 < Ma < 0.46$ . During the stationary cylinder experiments the static pressure distribution was measured and flow visualization techniques were used to gain additional understanding of the cylinder external flow patterns. Furthermore blockage effects during testing were considered to be negligible and wall-interference corrections were ignored. In order to achieve the large  $Re$ -numbers air and Freon were used at various densities to provide a broad range of  $Re$ -numbers. In their study they mention severe flow disturbances were present when the static pressure measurements were taken for the stationary cylinder due to inadequate sealing. This leakage problem was only fixed after the static pressure distribution was measured. Nonetheless the study found that increasing the  $Re$ -numbers (in the range  $8.27 \times 10^6 < Re < 18.70 \times 10^6$ ) had little effect on

the pressure distribution aside from slight increases in the negative pressure peaks ( $-1.9 < C_{p,min} < -2.3$ ). In addition the measured drag coefficients compared well with data from literature although large differences were observed when the data was compared to that of Roshko (1960). These large deviations were ascribed to the fact that Roshko used a roughened cylinder which increased the roughness factor of the cylinder to about 6 times. The data collected by Jones displayed symmetry as could be seen from the static pressure distributions in Figure 3.7 (c).

Cüven et al. (1980) conducted wind tunnel tests on a cylinder in the range  $7 \times 10^4 < Re < 5.5 \times 10^5$  with the aim of investigating the effects of surface roughness on mean pressure distribution. Five sizes of distributed sandpaper were used for the surface roughness modelling and it was found that roughness has a significant effect on the pressure distribution. The results showed that with increasing roughness the negative pressure peaks of the pressure distribution is reduced accompanied by the increase in cylinder back pressure. The results also displayed asymmetric behaviour for the pressure distributions along with near constant wake pressures; however since the pressure measurements on the opposite sides of the cylinder were not made simultaneously it was not possible to make a definitive conclusion concerning the observed asymmetry. In addition to measuring pressure distributions the study also included the measuring of boundary layer profiles. The study concluded with extensive comparison of measured data to available literature at the time. The latter includes pressure distribution, wake pressure and drag coefficient comparisons.

Buresti (1981) experimentally investigated the effect of surface roughness on the transition between flow regimes ranging from sub-critical to super-critical ( $2.6 \times 10^4 < Re < 2.8 \times 10^5$ ). The experiments were performed in an open-jet wind tunnel on circular cylinders roughened with emery cloth with relative roughness ranging from  $k/d \sim 1 \times 10^{-3}$  to  $12 \times 10^{-3}$ . Results from the study showed that the diameter of the cylinder used has no significant effect on the measured pressure distribution provided that the Reynolds number stays the same. Furthermore it was found that not only the degree of roughness used is important, but the type of roughness used should also be considered. Thus the latter implies that it is not as simple as to apply the same degree of roughness to a model and prototype in order to generate similar pressure distributions. Furthermore, the author stated that the latter observation is consistent with what Cüven et al. (1980) stated. The study concluded that surface roughening is an effective way of simulating larger  $Re$  regimes and that the presence of high surface roughness can lead to stabilized vortex shedding.

Nakamura & Tomonari (1982) conducted wind tunnel tests on cylinders with the aim of investigating the effects of surface roughness on mean pressure distribution over a range of  $4.0 \times 10^4 < Re < 1.7 \times 10^6$ . Polystyrene particles glued to the cylinder surface were used for coarse roughening and sand paper was used for finer roughness modelling. In addition the investigation also included the effect of

roughness strips which were 2 cm in width and located on the upper and lower sides of the cylinder at  $50^\circ$  (as measured from the upwind side of the cylinder). The results of the study suggested that flow in the trans-critical range could maintain good two-dimensionality as is evident from the largely uniform wake pressure observed. Furthermore the results showed that with increasing roughness the negative pressure peaks are reduced and the wake pressure is increased accompanied by earlier flow separation points. In addition the study suggested that high  $Re$ -number simulation can only be obtained by the use of roughness strips and not by distributed roughness. In general results from the study compared well with available data from literature.

Farrel and Arroyave (1990) investigated uniform flow around roughened cylinders at critical Reynolds numbers. The experiments were conducted in an open circuit wind tunnel on a circular cylinder with stainless steel wire cloth ( $k_s/d = 4.5 \times 10^{-3}$ ) used as the roughening technique. Mean pressure distributions were measured and from the curves two sub-ranges within the critical transition were observed. The study suggested that mean pressure distributions in the super-critical regime are symmetrical and the trans-critical regime is characterized by sharp vortex shedding peaks.

Ribeiro (1991) investigated the effects of surface roughness on circular cylinders with an aspect ratio of  $h/d = 6.1$  in a wind tunnel. He attempted to discover which type(s) of roughness was more efficient in triggering flow transition in order to simulate trans-critical  $Re$ -numbers. The investigations took place at low  $Re$ -numbers ( $5 \times 10^4 < Re < 4 \times 10^5$ ) and three different types of surface roughness were investigated: sand paper, wire mesh screen and ribs. Results from the investigation showed that with an increase in roughness the angle of minimum pressure and separation moved slightly upwind ( $5^\circ$ - $10^\circ$ ). In addition the data showed that as the surface is roughened there is a relief in suction pressure and increase in absolute wake pressure which ultimately results in an overall increase of pressure drag on the cylinder. The study concluded that sand paper was the least effective method for flow regime transitions and the ribs proved to be the most effective method.

Catalano et al. (2003) conducted a numerical experiment on the flow around a circular cylinder at high Reynolds numbers ( $0.5 \times 10^6 < Re < 2 \times 10^6$ ). A large-eddy simulation (LES) model with wall modelling was used along with flow conditions which fall in the supercritical regime. In addition the results from the LES model were compared to Fluent®'s unsteady Reynolds averaged Navier-Stokes (URANS) and Reynolds averaged Navier-Stokes (RANS) models. Catalano used a C-grid type mesh with uniform quadrilateral cells and for the case of the steady RANS model only half the computational domain was considered. The study showed that the mean pressure distribution of the LES model provides a good indication of what occurs experimentally; however there are some discrepancies with the calculated wake pressure and separation point when compared to the literature. Furthermore the RANS model (standard  $k$ - $\epsilon$ ) results

had a weak comparison to the data from literature as well as to the URANS and LES models. However the predicted wake pressure of the RANS model is consistent with that of the LES model (Figure 3.9).

## 2.4 Investigations of flow around finite cylinders

Gould (Gould et al. in Lupi (2013)) performed wind tunnel tests at high  $Re$ -numbers ( $Re = 2.7$  to  $5.4 \times 10^6$ ) on smooth circular cylinders. Different height to diameter ratios were investigated with a uniform velocity profile. The study included static pressure measurements along varying heights of the cylinder.

Majumdar and Rodi (1989) numerically investigated the flow field around a finite cylinder and cylindrical CT. The results from the models were compared to existing experimental data. The numerical domain consisted of uniform quadrilateral cells in an O-grid type mesh and only considered half the cylinder structure with a symmetric boundary condition used to account for the other half. The standard  $k-\varepsilon$  model along with standard wall functions was used for turbulence modelling with the pressure velocity coupling solved using the SIMPLEC algorithm. A steady RANS approach was used instead of a URANS approach due to limited computing power and a limitation of 80 000 nodes for the mesh. For the surface mounted cylinder investigation a cylinder with an aspect ratio of  $h/d = 1.9$  was used due to available experimental data from work done by Niemann and Hölscher (1990) reaching a Reynolds number of  $Re = 5 \times 10^5$ . The results from the numerical investigation compared fairly well to the experimental measurements indicating that many of the complex flow features around circular structures can be simulated realistically. However although the minimum pressure, stagnation pressure and pressure development during flow acceleration was predicted correctly the model under-predicted the cylinder drag, mostly due to the predicted delayed separation point and low negative wake pressure. The authors stated that this is mainly due to the steady solution of the model which does not take into account the unsteady components (such as vortex shedding) present in the flow. However the model used also ignored the effect of meridional ribs which were present on Niemann's scale model and assumed a smooth surface for the cylinder. It was also found that the stagnation pressure increases as the flow moves to the cylinder tip and it decreases as it moves to the cylinder base. Lastly it was observed that the flow around the mid-height of the cylinder is similar to flow around an infinite cylinder (2-D). The second model investigated was a cylindrical CT structure with a flow through the cylinder in order to investigate the plume effect. The results were compared to data of Violett (1977) who experimentally investigated the effect in a water tunnel on a cylinder with  $h/d = 1.64$  and  $Re = 2.57 \times 10^4$ . The plume spread was simulated fairly accurately in the vertical direction however in the horizontal direction the spreading was negatively affected by numerical diffusion errors.

Uematsu & Yamada (1994) investigated the aerodynamic forces on finite circular cylinders with aspect ratios ranging from  $h/d = 1$  to 5. The experiments were

conducted in a wind tunnel and focussed on the effect height to diameter ratio and surface roughness has on mean pressure distributions and drag coefficients measured at varying cylinder heights. Sand paper was used as the surface roughness technique and varied between relative roughness ( $k_s/d$ ) values of  $k_s/d = 282 \times 10^{-5}$  to  $1\,070 \times 10^{-5}$ . Furthermore the authors made no correction for blockage effects. Results suggested that for a specified roughness value important landmark features such as the angle of zero pressure, angle of minimum pressure, angle of flow separation, value for minimum pressure and wake pressure values do not significantly vary as measurements are taken along the cylinder height. The latter suggests that surface roughening then has a stabilizing effect on the mean pressure distribution along the height of the cylinder. In addition amongst numerous other observations it was also found that the mean drag (as obtained from the mean pressure distribution) has a general increasing trend as measurements are taken along the height of the cylinder. However; close to the tip of the cylinder the latter is not true.

Alberti (2006) studied the flow around solar chimneys and investigated the stabilizing role of vertical ribs located on the outer surface of a cylinder. Amongst other conclusions it was found that the presence of the ribs provide a more desirable pressure distribution around the cylinder compared to a one with no ribs at all.

More recently Krajnovic (2011) investigated the flow patterns and phenomena around a tall finite cylinder with an aspect ratio of  $h/d = 6$  with the aim of better describing the flow. The cylinder had a diameter of  $d = 0.03$  m resulting in a Reynolds number of  $Re = 2 \times 10^4$  and was numerically simulated using LES and the SIMPLEC algorithm for pressure velocity coupling. The mesh consisted of uniform quadrilateral elements and grid sizes varied from 7 to 21.5 million nodes. Static pressure distributions at 4 different height locations were compared to data from experiments and good agreement between the data was achieved. In addition it was found that there is a decrease in  $C_p$  distribution as profiles are taken from the base to the free end. Further observations made, consisted of a large recirculation zone at the cylinder tip originating from the leading edge and horse shoe vortices at the cylinder base.

Rostamy et al. (2012) also studied the flow around a finite cylinder in a low speed wind tunnel using PIV. The cylinders tested had aspect ratios of  $h/d = 9, 7, 5$  and  $3$  respectively with a Reynolds number of  $Re = 4.2 \times 10^4$  reached during testing. They were able to visualize all the flow phenomena around the cylinder including the mean recirculation zone on the cylinder tip, large near-wake recirculation zone with a vortex immediately behind and below the cylinder free end as well as the horse shoe vortex at the upstream cylinder wall. Later one of the authors compiled a review of all the latest findings and understanding of flow above the free end of a surface mounted cylinder focussing on the flow field and pressure and heat flux distributions on the free end surface (Sumner, 2013).



Lupi (2013) studied the design of ultra-high towers in the atmospheric boundary layer under the effect of cross-winds. The research focussed on solar chimneys used in solar updraft power plants. In the study wind-tunnel tests were performed on a scale solar chimney model (circular cylinder) and the effect of surface roughness and  $Re$ -number on the mean static pressure distribution was investigated. It should be stated that the full scale model  $Re$ -number of  $Re = 5 \times 10^8$  (trans-critical) could not be reproduced experimentally and the tests were performed at super-critical  $Re$ -numbers ( $Re = 3 \times 10^5$ ). However surface roughening in the form of ribs were applied to the model to account for the latter. The study confirmed typical effects surface roughening has on the mean pressure distribution including decreased pressure recovery with increasing roughness. Furthermore the study showed the variation of the mean drag coefficient along the height of the cylinder. In addition it was found that roughness enhances the flow over the tip of the cylinder due to the lower pressure created in the wake. Furthermore this low pressure behind the cylinder tip also constitutes the point of maximum mean drag coefficient. Results also suggest that roughening of the surface leads to more consistent pressure recoveries along the cylinder height as compared to a smooth surface case. The results also compared well to data from literature.

## 2.5 Conclusion

From the before mentioned studies it can be seen that there exists a need to better understand the airflow patterns around NDCTs and their effects on CT performance. In particular it is noted that past models focused more on the modelling of specific CT components such as windbreak walls whilst largely neglecting other components such as wind ribs, although it has been shown in research that these elements create a more favourable pressure distribution around the tower periphery.

Furthermore it can be seen that due to experimental constraints the majority of investigations do not fall within the trans-critical Reynolds regime applicable to CTs under the influence of cross winds and surface roughening techniques have to be employed to simulate the trans-critical regime. The development of an adequate CFD model would then be of use to aid in the understanding of these phenomena and subsequently lead to the development of methods to improve the performance and effectiveness of CT modelling in turn leading to possible reduced life cycle costs of the power plant.

## 3 Numerical analysis of flow around an infinite cylinder

In this chapter a two dimensional (2-D) computational fluid dynamic (CFD) model for an infinite cylinder is developed to model trans-critical Reynolds ( $Re$ ) flow around an infinite circular cylinder using a Reynolds Averaged Navier-Stokes (RANS) approach. The model is then used to perform a parametric study in order to identify a single parameter which can be used for the rigorous adjustment of the pressure distribution around a cylinder thus providing a method which can be used to easily re-create the effect that surface roughness such as actual wind ribs has on pressure distributions around cylindrical structures. In addition methods for reducing computational costs are also investigated.

### 3.1 Modelling

Flow around an infinite cylinder is modelled using the Fluent® CFD package. The flow is modelled as steady and 2-D using the double precision solver,  $k$ - $\epsilon$  Realizable turbulence model with standard wall functions, SIMPLE algorithm for pressure-velocity coupling and second order discretization scheme for all remaining equations. These are the models used by Reuter (2010) to model CT performance. Furthermore Störm (2010) also showed in his investigations that the  $k$ - $\epsilon$  Realizable model produces the most accurate results at the lowest computational effort.

#### 3.1.1 Geometry, flow domain and boundary conditions

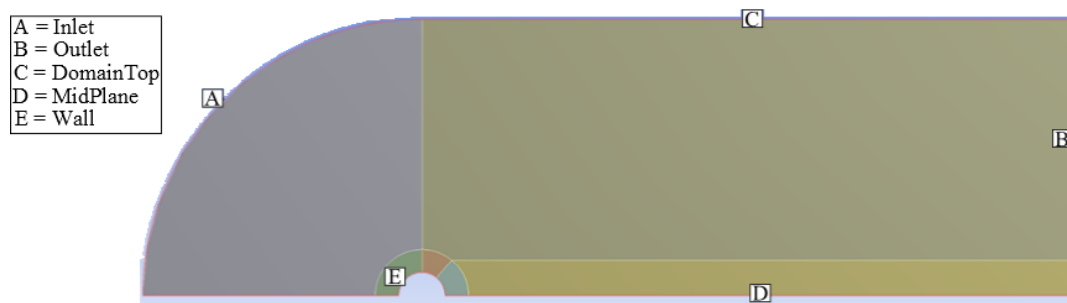
The cylinder modelled has a diameter of  $d = 0.4572$  m with an air density, viscosity and speed of  $\rho = 4.735$  kg/m<sup>3</sup>,  $\mu = 1.846 \times 10^{-5}$  Pa.s and  $V = 71.623$  m/s ( $Ma = 0.210$ ) respectively resulting in a Reynolds number of  $Re = 8.4 \times 10^6$ . The before mentioned conditions replicate those used by Roshko (1960) in his experimental set-up where the air was pressurized in order to achieve the applicable Reynolds number with the corresponding cylinder diameter. This condition is dynamically similar to a CT with a  $d = 55$  m diameter under the influence of a  $V = 2.5$  m/s cross-wind (light breeze).

At trans-critical Reynolds numbers the flow past a cylinder is unsteady due to vortex shedding in the cylinder wake and the high level of turbulence present in the flow. Although simulating the flow as unsteady would then be considered more accurate it would result in oscillating flow in the wake region which would lead to an oscillating pressure distribution around the cylinder circumference as well as a varying wake pressure, making it extremely difficult to compare results of different simulations in a constructive and repeatable manner. In addition simulating the flow as unsteady would increase the computational effort required since rigorous mesh refinement in the wake region would be necessary in order to fully capture the turbulent eddies.



In contrast, if a steady solution could be obtained through vortex shedding elimination, the varying pressure distribution around the cylinder will effectively be eliminated and will result in a near constant wake pressure. This in effect creates a platform that easily allows the comparison of one simulation to another since stable convergence is reached. In addition due to high thermal inertia inherent to CTs one would not see the transient effects in terms of performance.

In order to achieve such a steady state solution the CFD domain used is based on the experimental setup of Roshko (1960) with only one half of the cylinder simulated. This half cylinder domain is advantageous since, along with appropriate boundary conditions, it completely eliminates vortex shedding resulting in a constant pressure distribution around the cylinder once convergence is reached as well as decreases computational effort through halving the required amount of cells in the domain. The chosen CFD domain with descriptions is shown in Figure 3.1, followed by the corresponding boundary conditions (BC) and domain dimensions used given in Table 3.1.



**Figure 3.1: Model domain with descriptions**

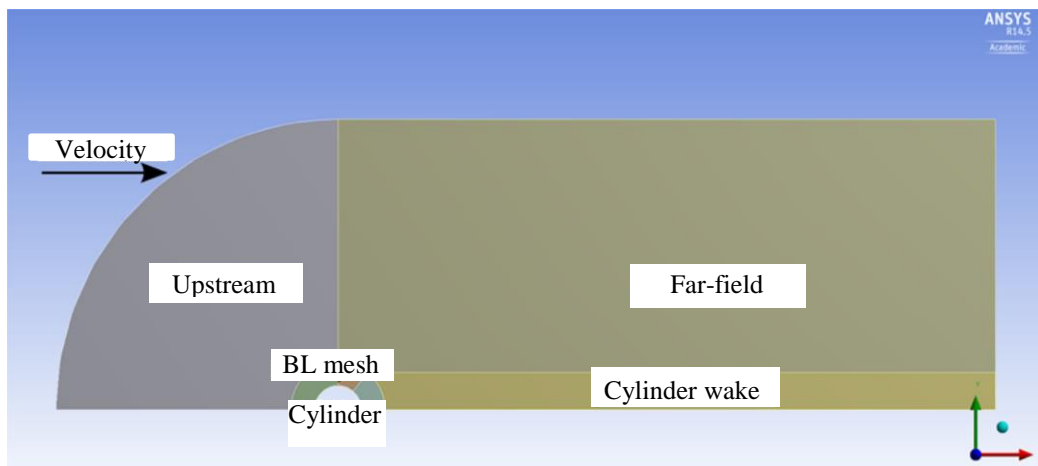
**Table 3.1: Boundary conditions and dimensions**

Description (region)	Boundary condition	Distance from cylinder centre
Inlet (A)	Velocity inlet	6D
Outlet (B)	Pressure outlet	14D
Domain Top (C)	Slip-wall	6D
Mid-plane Domain (D)	Symmetry	-
Cylinder Wall (E)	No-slip Wall	-
Boundary mesh	-	2D

The velocity inlet BC is used to define the velocity and scalar properties of the flow inlet boundary. The velocity component in the flow direction (x-direction) is set equal to the inlet velocity while the other components are set to  $V = 0$  m/s. The pressure outlet BC is used to define the air static pressure at the flow outlet. In this simulation the gauge pressure at the outlet was set to  $P = 0$  Pa which implies that

the pressure outlet is at atmospheric pressure. The no-slip BC sets the velocity at the wall equal to  $V = 0$  m/s while the  $k$  and  $\varepsilon$  values are set at the first node adjacent to the surface using standard wall functions. In the case of the symmetry BC it was found that the use of a slip-wall resulted in the same solution, however since half of a full cylinder domain is effectively solved it is more appropriate to set a symmetry BC.

Störm (2010) found that grid refinement at the boundary layer and wake region affect the pressure distribution calculated on the surface of a cylinder and that the boundary layer mesh must be extended at least a distance  $d/3$  away from the cylinder in order to obtain accurate results. This resulted in further sub-division of the domain into different regions as shown in Figure 3.2. In addition through subdividing the domain more control over the Fluent® mesher could be gained in regions of interest.

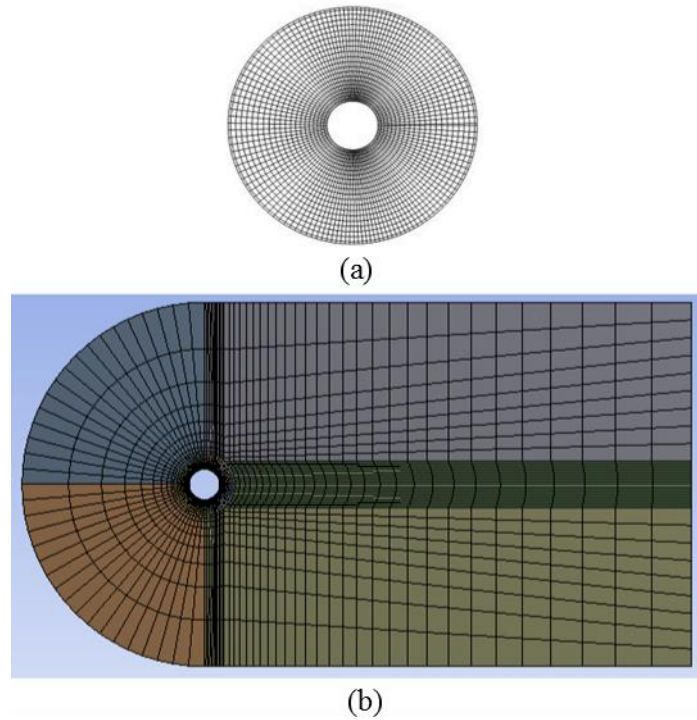


**Figure 3.2: Region designations**

### 3.1.2 Mesh

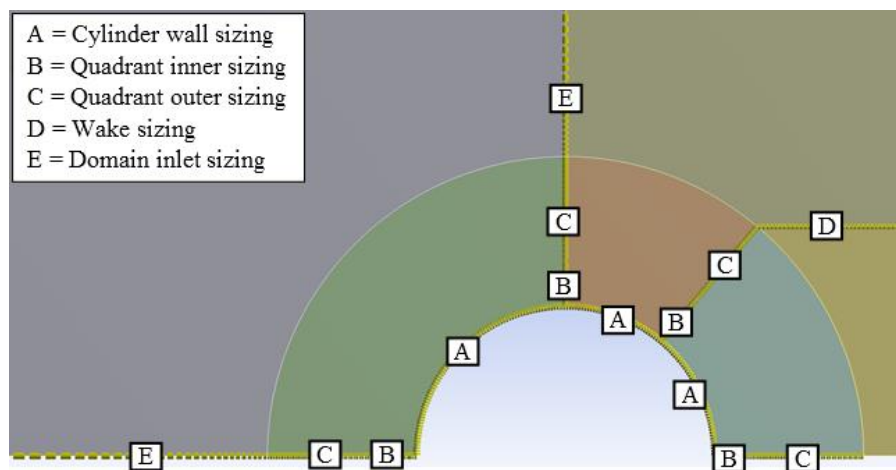
The mesh used for the CFD simulations consists of structured quadrilateral elements in a half C-grid domain. The decision of a C-grid over the conventional O-grid is purely to reduce the amount of unnecessary cells in the upstream region of the domain since it allows independent dimensioning for the upstream and downstream boundaries. An example mesh for both the O-grid and C-grid configurations is provided in Figure 3.3. Furthermore through the use of structured elements a more uniform and controlled mesh can be created. A hybrid type mesh was also considered in which the far field regions consisted of unstructured elements, however the transition between the structured and unstructured regions were inadequate and in some cases lead to an unnecessary increase in mesh element count.

The edges used for meshing is shown in Figure 3.4 followed by information on element sizing in Table 3.2. In addition an example mesh is provided in Figure 3.5.



**Figure 3.3: Different grid types: (a) O-grid; (b) C-grid**

The built-in Fluent® *Inflation* option cannot be used which resulted in the use of edge sizing and biasing to create the near wall mesh. Alternatively instead of biasing a growth rate can be defined although these two methods are interchangeable. In order to ensure a uniform mesh “*Mapped face meshing*” was applied to all surfaces within the domain. To avoid unwanted automatic biasing by the Fluent® mesher the “*Advanced size function*” in the mesher was deactivated. All of the above ensures that minimal control is left to the mesher and maximum control, at important regions, is given to the user.

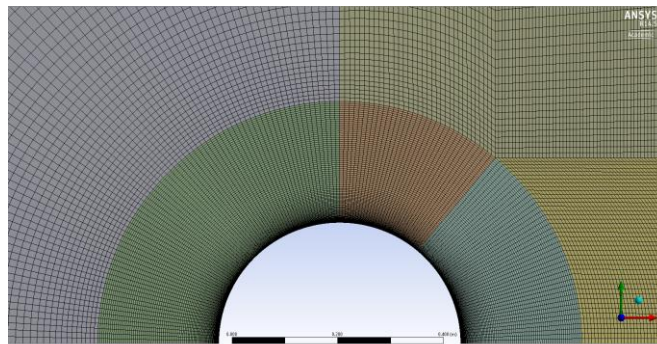


**Figure 3.4: Edges used for sizing**

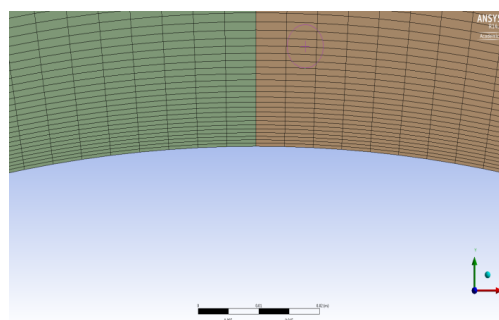
**Table 3.2: Edge sizing and bias factors used**

Edge	Element size (m)	Bias
A	0.004788 (300 divisions)	-
B	0.0015	8
C	0.0042	-
D	0.0064	-
E	0.04	16
Total cell count		115 412 cells

The resulting mesh can be considered extremely conservative due to its large downstream length which can be further shortened to  $10d$  instead of  $14d$  without significant change in simulation results. However if this mesh were to be used for a URANS simulation the  $14d$  case will be more desirable since transient effects will play a major role in the wake region. Furthermore since current investigations use a steady state solver the solution is fairly insensitive to wake coarsening and subsequently edge D in Table 3.2 can be drastically coarsened in order to reduce the number of elements if desired.



(a)



(b)

**Figure 3.5: Meshing around the cylinder: (a) Mesh around cylinder; (b) Wall adjacent cells**

### 3.2 Momentum adjustment procedure

Momentum adjustment can be achieved by varying the cylinder wall shear stress ( $\tau_{wall}$ ) in various ways in an attempt to simulate the effect that meridional ribs, as typically encountered on CT structures, would have on the pressure distribution around the cylinder. Consider the basic definition of total apparent shear stress for a Newtonian fluid as given by equation (3.1) below (Cengel and Cimbala, 2010):

$$\tau_{wall} = (\mu_{lam} + \mu_T) \left( \frac{d\bar{u}}{dy} \right)_{y=0} \quad (3.1)$$

From this definition there are effectively two ways of directly altering the wall shear stress. The first method is to change the total effective viscosity in the near wall region. In Fluent® this is achieved through either locally increasing the molecular viscosity near the wall via a User Defined Function (UDF) or through roughening the surface of the cylinder by using the built-in surface roughness model.

Through surface roughening the turbulence of the flow is increased leading to an increase in turbulent viscosity ( $\mu_T$ ) and ultimately wall shear stress. One advantage of surface roughening is that it can be applied physically to cylinders and full scale cooling towers in practice through the use of numerous methods including meridional ribs (Niemann and Hölscher, 1990). Through increasing the molecular viscosity ( $\mu_{lam}$ ) in the cells adjacent to the cylinder wall (UDF option) more friction is present in the near wall region. From equation (3.1) it is obvious that through increasing  $\mu_{lam}$  the wall shear stress is also increased leading to an increase in resistance to momentum in the near wall region.

The second method is to change the velocity gradient at the cylinder wall. This can be achieved numerically in Fluent® by rotating the cylinder at varying angular velocities which is only possible if half a cylinder is modelled. This rotation effectively increases the wall velocity relative to the free stream flow velocity leading to a increase in velocity gradient at the wall.

The aim of the parametric study as outlined above is to determine the effect the respective alterations have on the pressure field in the vicinity of the cylinder. In order to quantify this effect the static pressure coefficient on the cylinder surface was computed for the varying cases.

### 3.3 Numerical results and discussion

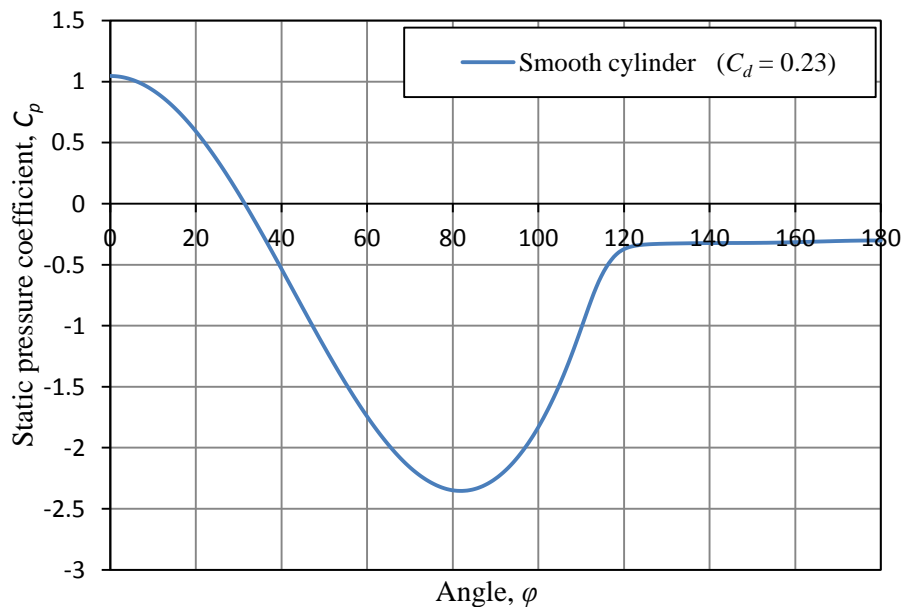
In this section results obtained from the 2-D Fluent® model are presented and compared. The reference (ref) mesh and conditions used are provided in Table 3.2. This reference condition constitutes a mesh which is found through a grid independence study where successive meshes are refined until the solution remains unchanged. The latter is based on the change in values of important  $C_p$  curve features such as the value of minimum pressure coefficient, value of wake

pressure coefficient and their corresponding angles as the mesh is systematically refined. This verification of mesh independency is based on guidelines provided in Versteeg (Versteeg & Malalasekera, 2007). The  $y^+$  values at the wall boundary fall within the advised range of  $30 < y^+ < 300$ , to accurately bridge the viscous sub-layer using standard wall functions.

It is worth noting that the stagnation pressure on the cylinder windward side slightly deviates from 1 in simulation results. However, it has been observed in literature that at high degrees of free stream turbulence, which is inherent to trans-critical flow, the stagnation pressure can be larger than 1 showing that with increasing large turbulence there is an increase of the stagnation pressure (Pröper, 1977). Furthermore the symbols used to distinguish between graphs, for the numerical results, do not necessarily represent all the data points used to determine the curves, rather only select data points are highlighted in order to distinguish between varying curves. Data points are connected with straight lines.

### 3.3.1 Reference model compared to data from literature

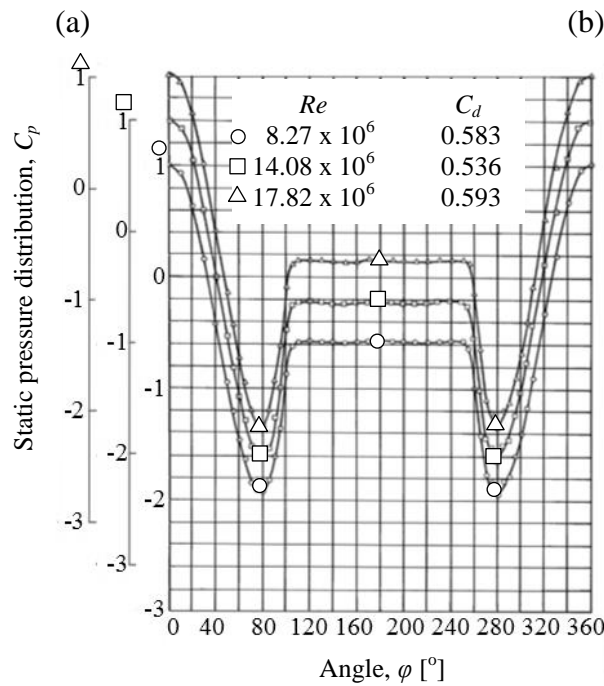
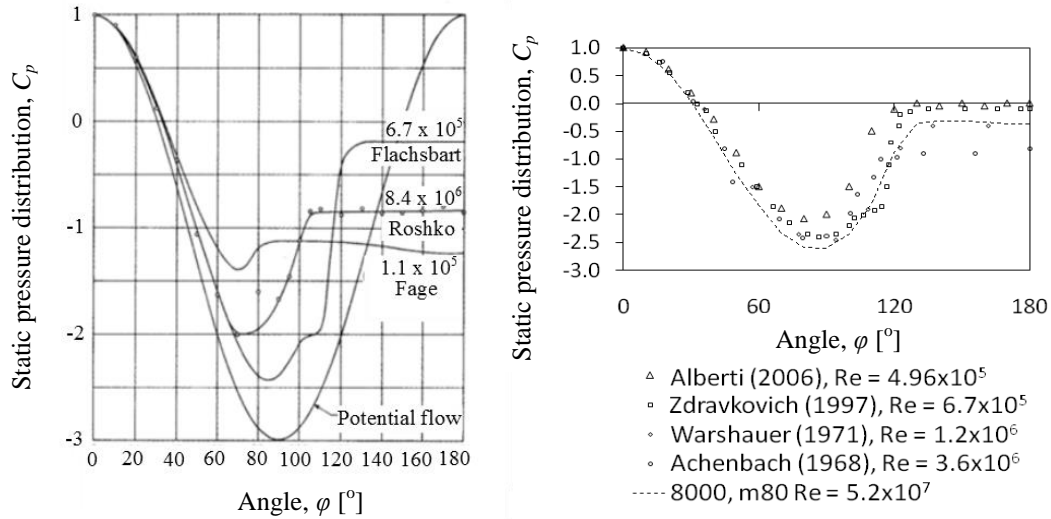
Before continuing to the parametric study an attempt is made to compare the reference Fluent® model results to similar pressure distribution trends found in literature. Figure 3.6 shows the CFD model results followed by Figure 3.7 to Figure 3.8 showing various data from literature pertaining to the general trends of pressure distributions around cylinders as well as specific data on measured values for the minimum pressure ( $C_{p,min}$ ), wake pressure ( $C_{pb}$ ) and cylinder pressure drag ( $C_d$ ).



**Figure 3.6: Reference model  $C_p$  curve for  $Re = 8.4 \times 10^6$**

First consider the results from Figure 3.6 and the curve of Roshko in Figure 3.7 (a). Important angles measured by Roshko, such as the angle of

minimum pressure ( $\varphi_l \sim 70^\circ$ ) and angle of separation ( $\varphi_N \sim 105^\circ$ ) do not correspond accurately to the generated CFD data which predicts an angle of minimum pressure closer to  $\varphi_l = 80^\circ$  and an angle of separation closer to  $\varphi_N = 120^\circ$ . However the angle of minimum pressure on Roshko's curve might be somewhat inaccurate due to a faulty data point at approximately  $80^\circ$  which was neglected by the author. On the other hand the angle of zero pressure corresponds fairly well at approximately  $\varphi_0 = 31^\circ$ .



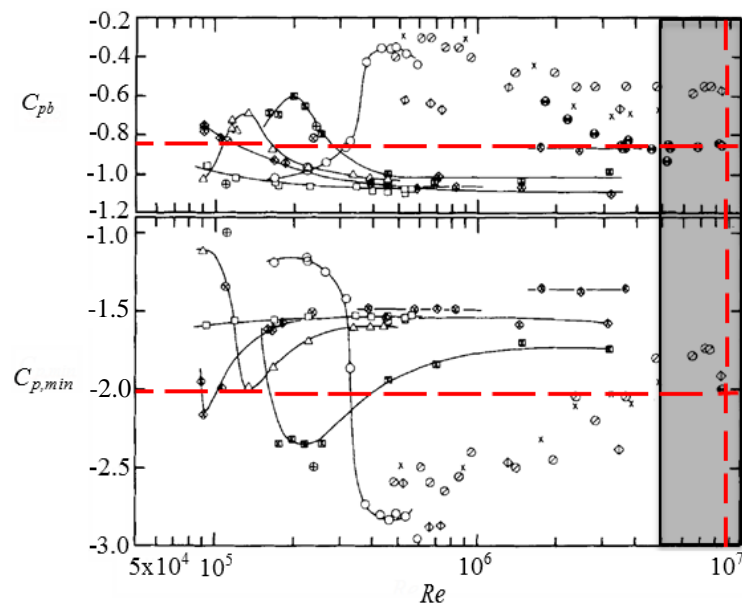
(c)

Figure 3.7:  $C_p$  distributions: (a) Roshko (1960); (b) Störm (2010); (c) Jones (1969)



In addition the values of minimum pressure coefficient and wake pressure coefficient of the CFD results and Roshko are not similar with significant deviations of  $C_{p,min}$  and  $C_{pb}$  values. Now consider the rest of the  $C_p$  distributions in Figure 3.7 (a) to (c) more holistically. Important angles such as the angle of zero pressure ( $\varphi_0 \sim 30^\circ$  to  $35^\circ$ ), angle of minimum pressure ( $\varphi_l \sim 75^\circ$  to  $85^\circ$ ) and angle of separation ( $\varphi_N \sim 110^\circ$  to  $125^\circ$ ) generally correspond well with one another with fairly consistent trends between the measured and numerically generated data. However when considering data which falls well into the trans-critical regime ( $Re > 5 \times 10^6$ ) in Figure 3.7 (c) it is apparent that there are slight deviations between the CFD model and measured data from literature. Although the angle of zero pressure still compares well the angle of minimum pressure predicted is approximately  $\varphi_l = 82^\circ$  which is slightly larger than the measured angle which is at  $\varphi_l = 80^\circ$ . Furthermore the CFD model also predicts a delayed separation point around  $\varphi_N = 120^\circ$  as compared to the measured separation point at about  $\varphi_N = 115^\circ$ .

In addition when the values for  $C_{p,min}$  and  $C_{pb}$  of the CFD data is compared to data obtained experimentally from varying authors summarized in Figure 3.8 significant differences are observed. In the figure the trans-critical regime is highlighted by the grey area and the Reynolds number used by Roshko is indicated using the vertical dashed line along with the respective pressure coefficient indicated with the horizontal dashed line. Furthermore the solid lines show suggested trends of behaviour as observed by a specific investigator.



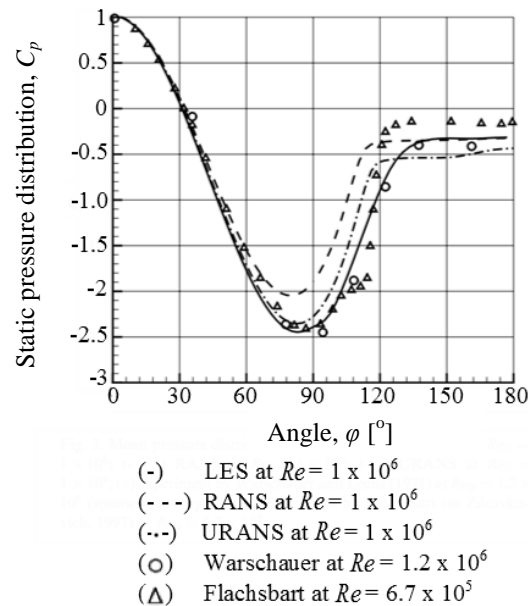
**Figure 3.8: Summary of  $C_{p,min}$  and  $C_{pb}$  values for cylinders at various Re-numbers (Güven, et al., 1980)**

For example it can be seen that the predicted  $C_{p,min}$  value of  $C_{p,min} = -2.35$  does not fall within the range of measured values ranging from  $C_{p,min} = -1.8$  to  $-2.0$  suggesting that the CFD model over estimates this value.



Furthermore the predicted  $C_{pb}$  value of  $C_{pb} = -0.33$  once again does not fall into the measured range of  $C_{pb} = -0.58$  to  $-0.90$  suggesting that on this occasion the CFD model under predicts this value. Due to these differences in minimum and wake pressure values the CFD model also severely underestimates the pressure drag coefficient at a value of  $C_d = 0.23$  compared to a value closer to  $C_d = 0.58$  from measured data trends in Figure 3.7 (c). Although in some literature the expected drag coefficient, as based on the cylinder frontal area, is approximately  $C_d = 0.3$  for turbulent flow (Cengel & Cimbala, 2010).

However, it is worth noting that CFD models are known for their prediction of delayed separation points and over- and underestimations of the minimum and wake pressures respectively as can be seen in Figure 3.9 when considering the data of Catalano et al. (2003) who investigated the flow around a cylinder at  $Re = 1 \times 10^6$  numerically. It is also interesting to note that the CFD models used by Catalano struggled to maintain the stagnation point exactly at 1.



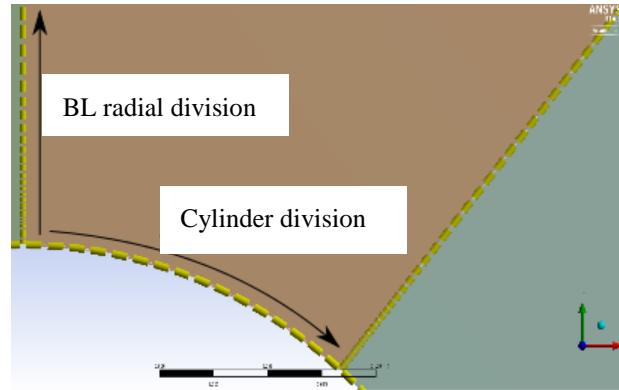
**Figure 3.9: Results of Catalano at  $Re = 1 \times 10^6$  (Catalano et al., 2003)**

In conclusion to this section it is noteworthy to state that it is not a straightforward task to compare the CFD data to that from literature due to multiple factors. These factors include the scarcity of available data (due to experimental restrictions) in the trans-critical regime and the fact that of the data available in this regime there are large observed discrepancies between measured data, specifically between minimum and wake pressure values. Nonetheless the general characteristic of the CFD model is consistent with those observed in literature and is deemed fit for use in parametric studies.

### 3.3.2 Grid sensitivity analysis

Du Preez and Kröger (1995) compared full scale CT measurements to a CFD model they developed and found good agreement between the data trends. The

authors stated that their model was considered extremely conservative and that a mesh independence study was performed however, the grid used was extremely coarse at only 4 920 cells used. Furthermore due to a lack of time and computational power only the tower and the immediate surroundings were included in the model. In order to investigate a possible explanation for this good agreement between the coarse model and on site measurements a sensitivity analysis on select mesh sizing is performed.



**Figure 3.10: Boundary layer mesh detail**

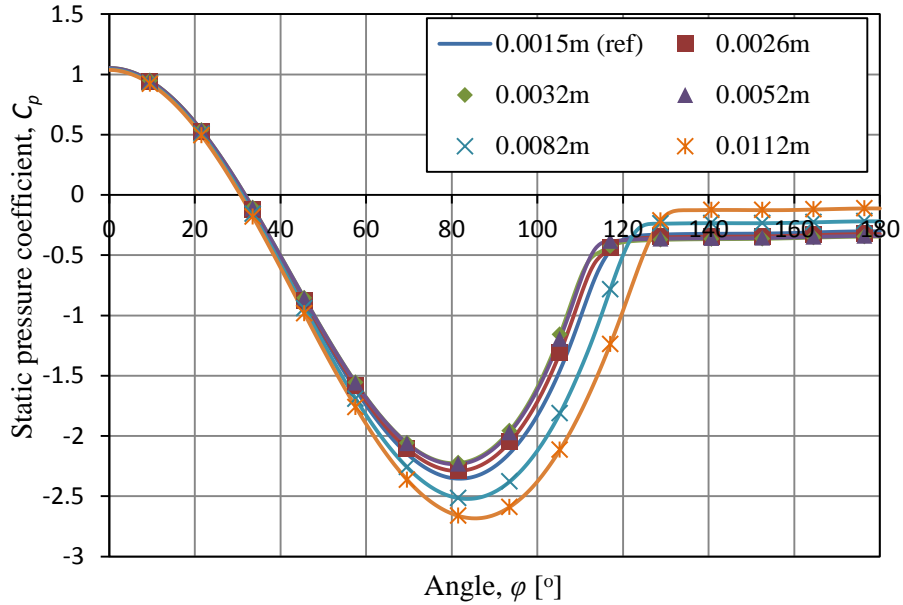
The first mesh parameter considered is the resolution of the BL radial division (edge B in Table 3.2 and Figure 3.10). The cell elements are systematically coarsened whilst the remaining factors such as biasing remains unchanged. Since edge C is also enclosed in the BL mesh and it has no bias attached to it the elements are adjusted to fit the size of the last cell along edge B in order to provide a smooth transition in the BL mesh zone (Figure 3.2).

Figure 3.11 shows the surface static pressure coefficient ( $C_p$ ) distribution along the cylinder wall as calculated from the cylinder upstream position ( $\varphi = 0^\circ$ ) to the cylinder downstream position ( $\varphi = 180^\circ$ ) for various cell element sizes.

The results indicate that the gradual coarsening of the BL mesh in the radial direction does not significantly alter the expected  $C_p$  curve trend. From the data it can be seen that coarsening generally leads to an upward shift of the minimum  $C_p$  value ( $C_{p,min}$ ) along with an earlier separation point. This upward shift in  $C_{p,min}$  signifies reduced suction on the cylinder side accompanied by a larger wake due to earlier flow separation.

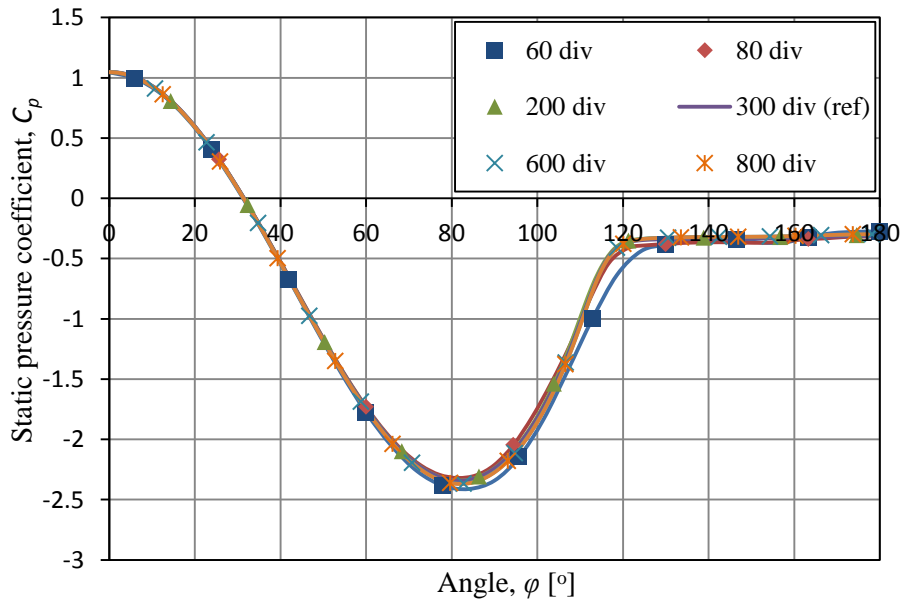
Furthermore it is observed that the cylinder back pressure ( $C_{pb}$ ) is not significantly affected. However at large element sizes (0.0082 m and higher) a significant downward shift in  $C_{p,min}$  is noted accompanied by a noticeable upward shift in  $C_{pb}$  as well as a delayed flow separation point. Further increasing the element size leads to greater suction on the cylinder side accompanied by a smaller wake in the cylinder downstream region. This large deviation from the reference mesh is mainly caused by the increasing values of  $y^+$  found in the near wall region which exceeds  $y^+ = 1500$  at the largest element size investigated.

Due to the large  $y^+$  values, weak approximations for the wall function bridging the viscous sub-layer are generated resulting in a large deviation from the reference mesh. It is worth noting that, although the  $y^+$  guidelines are not followed for coarser meshes (as is evident from the large  $y^+$  values generated), the general shape/trend of the  $C_p$  curve is still the same as the reference case and those found in Figure 3.7 (a) to (c).



**Figure 3.11: Radial wall element size variation**

Figure 3.12 depicts the  $C_p$  distribution when the number of element divisions along the cylinder surface is varied (edge A in Table 3.2 and Figure 3.10).



**Figure 3.12: Cylinder wall division element size variation**

The data indicates that varying the element size along the cylinder has no significant effect on the  $C_p$  curve with minimal shifting of the curve observed. It can, however, be stated that with extremely coarse elements on the cylinder surface (60 divisions) the curve has a delayed separation point and a prolonged period of recovery. The latter can be ascribed to the weak mesh resolution accompanying the coarse grid leading to information being lost along the cylinder surface.

As a final investigation the original BL mesh was kept constant and the edge sizing in the wake region was coarsened (edge D in Table 3.2). It was observed that coarsening the wake region had an insignificant effect on the static pressure distribution around the cylinder periphery as can be seen in Table 3.3 when important  $C_p$  trend characteristics are compared. Note that the large number of decimals is only used to illustrate differences in mesh results and by no means illustrate the level of accuracy that the model provides.

**Table 3.3: Wake coarsening**

Wake edge sizing (m)	Minimum pressure coefficient, $C_{p,min}$	Angle of separation, $\varphi_N$	Wake pressure coefficient, $C_{pb}$
0.0064 (ref)	-2.343086153	~ 121	-0.311906512
0.008	-2.353600059	~ 121	-0.302057032
0.032	-2.353608292	~ 121	-0.302056209
0.064	-2.353600059	~ 121	-0.302059502

This is advantageous since it suggests that more rigorous coarsening of the wake region is possible without the loss of information in the vicinity of the cylinder. However it should be kept in mind that a RANS solution is utilized here and for the case of using a URANS solution wake refinement is necessary in order to capture transient behaviour of the flow in the wake region.

The mesh division analysis consisted of varying the coarseness of the mesh and in effect also the aspect ratio in the near wall region. It was found that through varying the BL mesh radial element size the  $C_p$  curve could be manipulated in either an upward shift or downward shift of the curve. The latter was ascribed to the extremely large  $y^+$  values resulting in weak approximations of the wall functions necessary for viscous sub-layer bridging.

Furthermore it was observed that through varying the number of divisions along the cylinder wall surface the  $C_p$  curve trend remained generally unchanged for all practical purposes. The above discoveries indicate that through the use of a coarse mesh a good approximation for the general  $C_p$  trend around a cylinder can be obtained even if the suggested rules for the turbulence model used are not adhered to.

### 3.3.3 Surface roughness analysis

There is limited information available on surface roughness around cylinders within the trans-critical  $Re$ -number regime. Most investigators did not have adequate facilities to reach trans-critical  $Re$ -numbers, aside from using roughening techniques to simulate the regime, leading to most available data lying in the super critical range or even lower.

Niemann and Hölscher (1990) investigated surface roughness on scale NDCTs through the use of ribs located on the CT shell (Figure 1.3) and found that with increasing roughness the suction on the sides of the CT are reduced. Similar effects have also been observed with flow around cylinders where surface roughness was modelled through the use of sand paper and numerous other techniques. The results generally show an upward shifting trend of the  $C_p$  curve with increasing roughness.

In this section the built-in rough wall formulation model of Fluent® is utilized to simulate the effects of increasing surface roughness. In order to activate the model an equivalent sand grain roughness height ( $k_s$ ) must be specified for the cylinder wall surface. Once a value for  $k_s$  is supplied the solver will automatically use the turbulence model with adjusted wall functions for surface roughness.

In version 14.5.7 of Fluent® this adjustment is made via a downward shift in the logarithmic velocity profile as shown in Figure 3.13. In addition due to the assumption that surface roughening creates a blockage effect the rough wall formulation physically shifts the wall boundary by 50 % of the specified  $k_s$  value (Fluent, 2013). Fluent® states the rough wall formulation incorporating the shift introduced eliminates all restrictions with respect to mesh resolution near the wall (as can be seen in Figure 3.13) and can subsequently be run on arbitrary fine meshes. The latter is a new feature in version 14.0, prior to this it was necessary to ensure that the first cell central node was at least a distance of  $k_s/2$  from the wall.

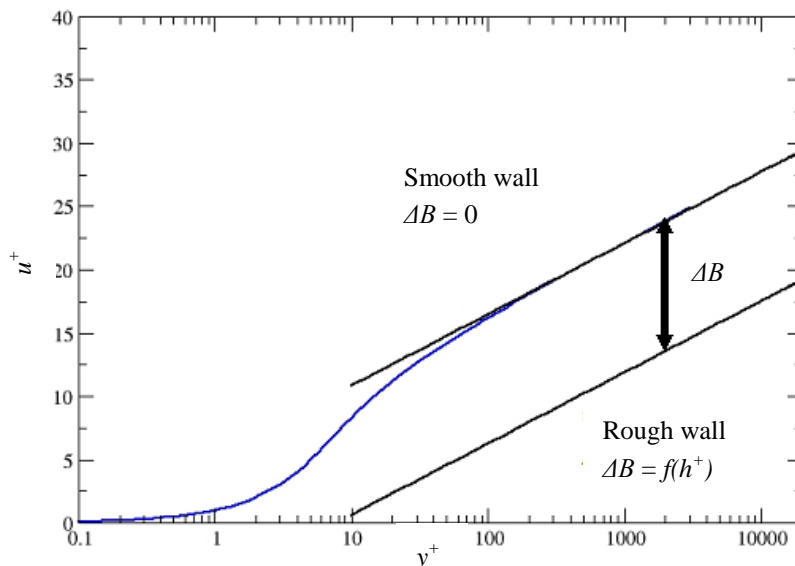
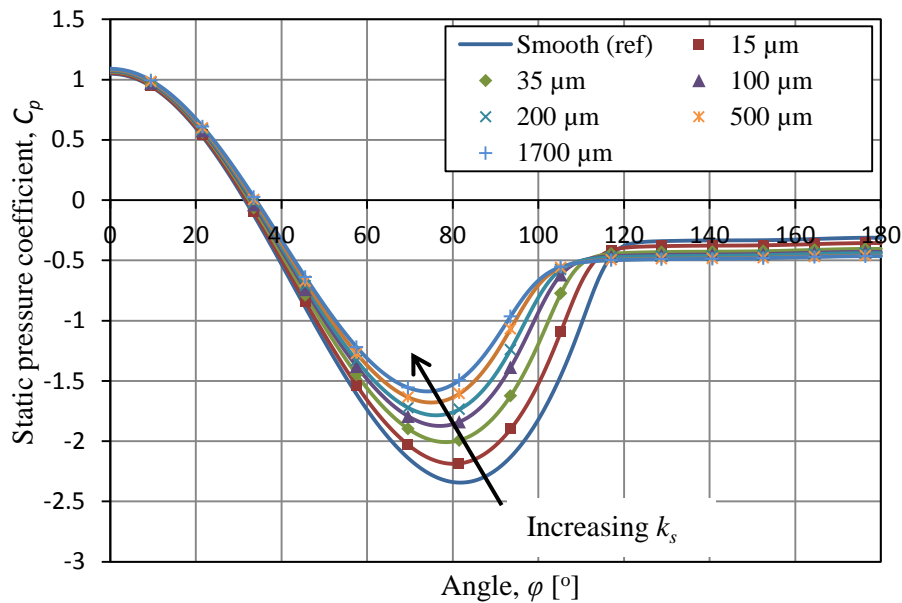


Figure 3.13: Rough wall modelling in Fluent, Log-Law shift (Fluent, 2013)

Figure 3.14 shows the effect of surface roughness as  $k_s$  is increased from a smooth surface to an extremely rough surface. When considering the effect of a stepwise increase in the surface roughness it is observed that as the roughness is increased the  $C_p$  curve is shifted in an upward trend with the minimum pressure and wake pressure increasing and the flow separation point shifting upwind.



**Figure 3.14: Effect of surface roughness on static pressure coefficient**

This trend of relieved minimum pressure on the cylinder side and increased wake pressure is consistent with what is observed experimentally when a surface is roughened as can be seen when the simulation results are compared to data in Figure 3.15 and Figure 3.16. In addition the wake pressure in the simulation seems to tend towards a value of  $C_{pb} = -0.5$  which is also consistent with wake pressures in Figure 3.7. However it should be noted that the majority of the researchers mentioned did not reach the trans-critical Reynolds regime directly, due to wind tunnel constraints, instead surface roughening was used to simulate large  $Re$ -number flows. Subsequently the comparison of data can only be made on trends observed as roughness is increased and not specific values.

In addition to the data from cylinders this behavioural trend of increasing surface roughness is consistent with data obtained by Zhao et al. (2012) who performed surface roughness tests on a 1:200 scale hyperboloid CT. In the tests of Zhao surface roughness was modelled through creating ribs with varying layers of paper tape as in Figure 3.17. It should be kept in mind that the model considered in this section is not only 2-D but is also purely cylindrical, which is not the case for Zhao who used a hyperboloid structure. Subsequently a direct comparison between the results is not possible. Nonetheless it is interesting to note the resemblance between the sets of data for similar  $C_p$  curves based on their  $C_{p,min}$  values.

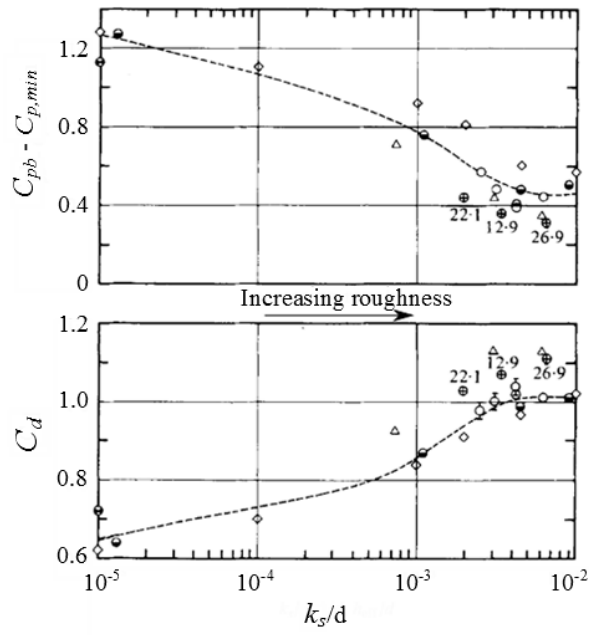


Figure 3.15: Variation of  $C_{pb}-C_{p,min}$  and  $C_d$  with increasing roughness (Güven, et al., 1980)

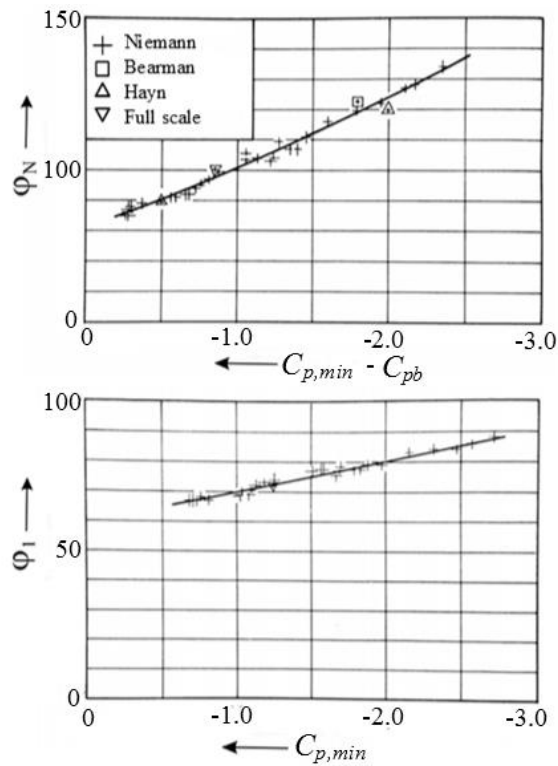
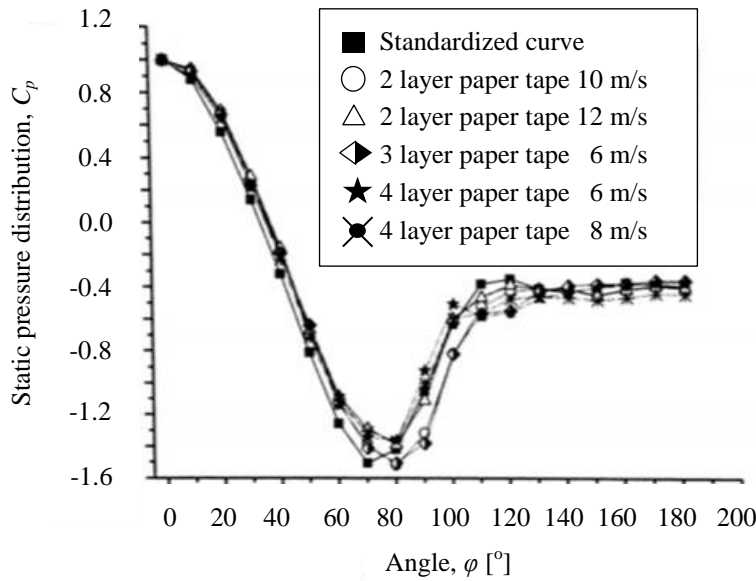


Figure 3.16: General pressure distribution trends with increasing roughness (Niemann, 1971)



**Figure 3.17: Data of Zhao et al. (2012)**

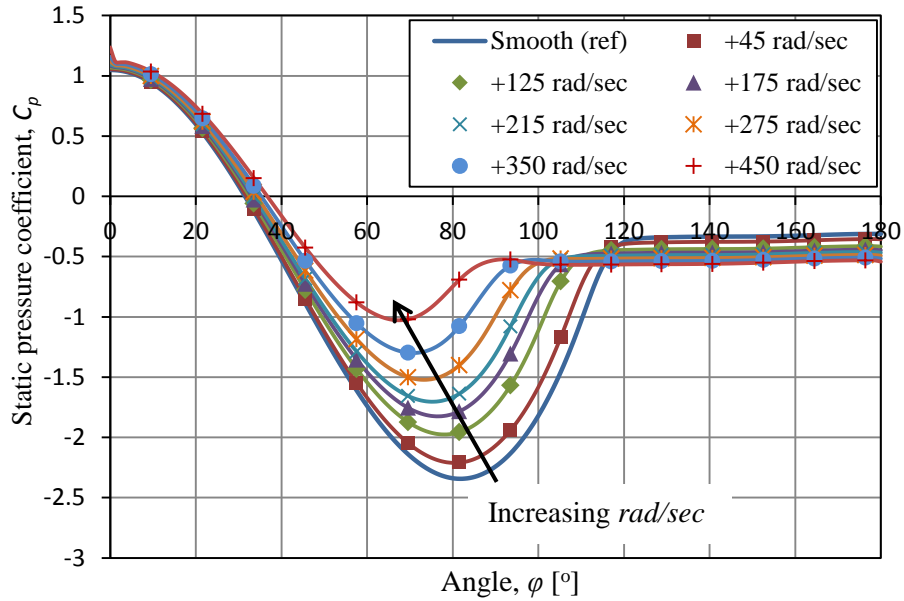
When  $k_s$  was increased further to higher roughness values it was found that there is a decrease in  $C_{p,min}$  with the  $C_p$  curve trend moving back towards the initial reference curve. The reason for this subsequent decreasing trend of the  $C_p$  distribution is ascribed to the large  $y^+$  values resulting in weak approximations for the RANS equations which in return limit the maximum allowable  $k_s$  value which can be used.

### 3.3.4 Rotating cylinder analysis

As mentioned in section 3.2, an alternative method for altering  $\tau_{wall}$  is to increase the velocity gradient at the cylinder wall. This can be achieved through rotating the cylinder by varying its angular velocity numerically. Figure 3.18 shows results obtained from the 2-D Fluent® model when the cylinder wall boundary condition is set to a rotating cylinder and a given angular velocity.

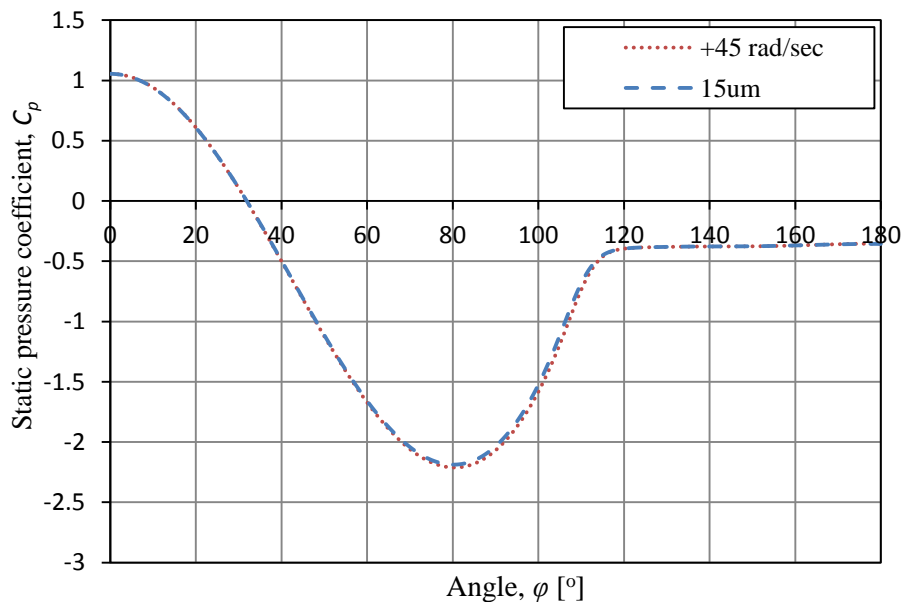
When considering the variation of the cylinder rotational speed in Figure 3.18 again this upward shifting trend of the  $C_p$  curve is observed as the angular velocity is increased. As the angular velocity is systematically increased there is a corresponding increase in the minimum pressure, increase in the wake pressure and earlier separation point. Furthermore the wake pressure also tends toward  $C_{pb} = -0.5$  as in the surface roughness variation case. When similar curves, based on their  $C_{p,min}$  value in Figure 3.14, are compared to curves in Figure 3.18, it can be seen that both methods result in the exact same solution as shown in Figure 3.19.





**Figure 3.18: Effect of cylinder rotation on static pressure coefficient**

However, whereas it was only possible to adjust the  $C_p$  curve to a minimum pressure value of  $C_{p,min} = -1.58$  using the surface roughness technique, the cylinder variation technique allowed adjustment of the minimum pressure of up to a value of  $C_{p,min} = -1.0$ . This is of importance since for actual NDCTs, which are 3 dimensional (3-D), the  $C_{p,min}$  values fall in this range. Bearing in mind that this study uses a 2-D infinite cylinder an attempt can be made to compare the data to measured data of Zhao in Figure 3.17.



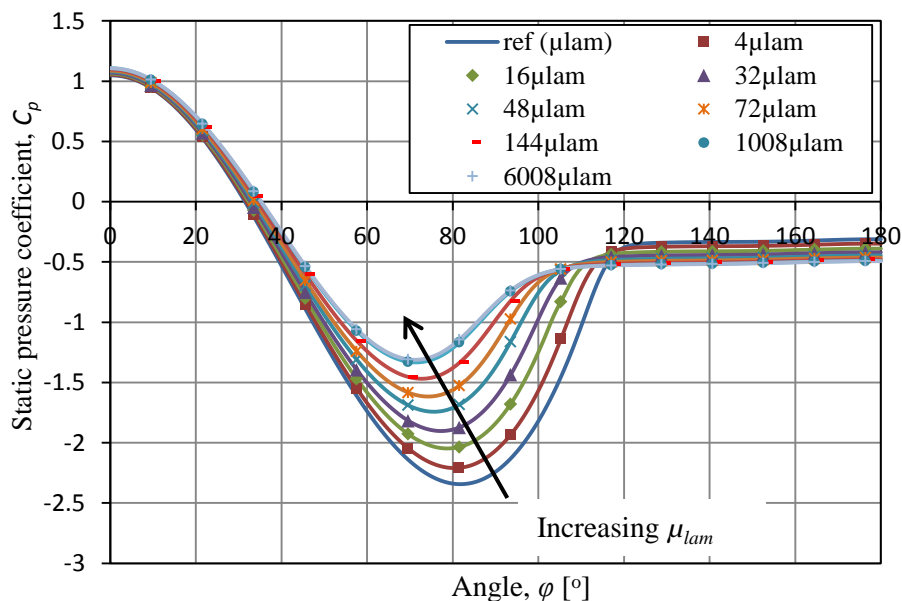
**Figure 3.19: Comparison between surface roughness and cylinder rotation**

Interestingly enough there are numerous consistencies in the data with the CFD model and measured data corresponding well with regards to the angle of zero pressure, angle of and value for the minimum pressure and wake pressure value approximately approaching  $C_{pb} = -0.5$ .

However, although a more rigorous manipulation of the  $C_p$  curve was achieved with the cylinder rotation technique the pressure distribution becomes slightly unstable as the angular velocity exceeds 350 rad/sec and it is difficult to maintain the windward stagnation pressure close to 1 as higher velocities are reached.

### 3.3.5 Wall viscosity variation

The last method for altering  $\tau_{wall}$  is through artificially increasing the laminar viscosity ( $\mu_{lam}$ ) of the wall cells adjacent to the shell wall directly through the use of a UDF which multiplies it by a constant factor. An example of the latter UDF is provided in Appendix A. It is clearly deducible from Figure 3.20 that by increasing  $\mu_{lam}$  the  $C_p$  curve can be adjusted in exactly the same manner as surface roughening. This, however, is expected since through surface roughening the  $\mu_t$  is increased instead of  $\mu_{lam}$  which both ultimately contribute towards the increase in total (effective) viscosity, however, the surface roughness technique uses a different model.

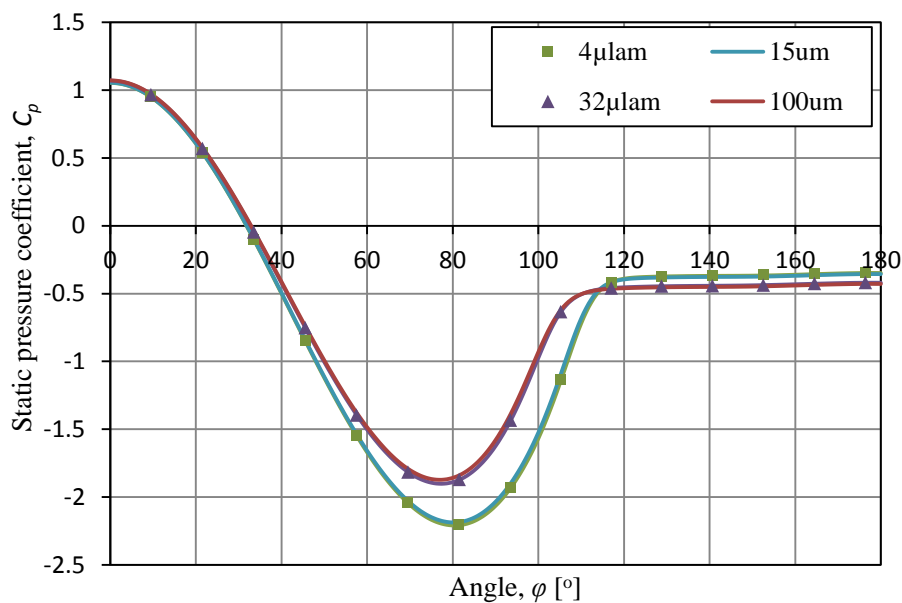


**Figure 3.20: Effect of wall viscosity on the static pressure coefficient**

Up to a viscosity of  $\mu = 4\mu_{lam}$  near the surface the  $y^+$  values fall within the acceptable range for standard wall functions ( $30 < y^+ < 80$ ). However as the viscosity is further increased the  $y^+$  values at the wall drastically starts to decrease to  $y^+ < 1$  when the viscosity reaches  $\mu = 1008\mu_{lam}$ . Furthermore from a viscosity of  $\mu = 144\mu_{lam}$  the effect of further increasing  $\mu_{lam}$  seems to be less severe. In fact it was found that when the viscosity is increased to values larger than

$\mu = 6008\mu_{lam}$  there is no significant change in the  $C_p$  distribution trend indicating adjustment saturation. Furthermore it should also be kept in mind that the severity of the variation  $\mu_{lam}$  has on the pressure distribution is closely connected to the dynamic conditions of the flow.

When compared to Figure 3.14, however, this method seems more favourable since it permits the adjustment of the  $C_{p,min}$  to values above  $C_{p,min} = -1.5$  which was not possible through the use of the built-in surface roughness model in Fluent®. Figure 3.21 shows a comparison between the surface roughness- and laminar viscosity-variation obtained from simulations. It is seen that both methods result in extremely similar results with only slight deviations for the  $C_{p,min}$  values. Other important features such as the point of flow separation and wake pressure values are for all practical purposes the same.



**Figure 3.21: Comparison of  $\mu_{lam}$  method and  $k_s$  method**

### 3.3.6 Mesh coarsening using wall viscosity

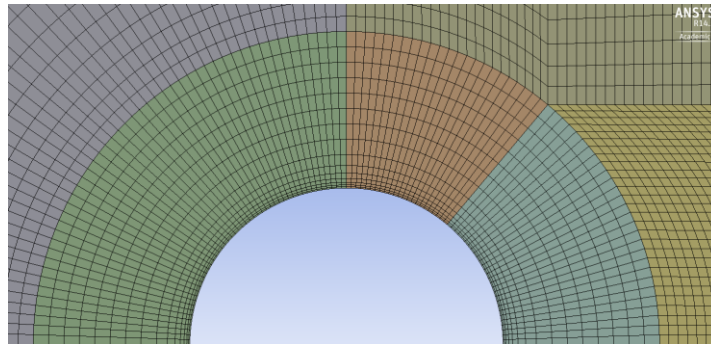
In section 3.3.5 it is observed that as the wall adjacent cell viscosity is increased the  $y^+$  values at the wall drastically decrease. In this section the latter occurrence is exploited and the mesh is coarsened such that, with a given viscosity range, the  $y^+$  values fall within the suggested range of  $30 < y^+ < 300$  for standard wall functions.

The mesh is generated through coarsening the cell elements of both the radial division and the cylinder wall division (as defined in Figure 3.10). In addition the remaining edges are sized to provide smooth transition between cell elements. Furthermore the mesh size is determined by specifying a wall cell adjacent viscosity of  $\mu = 16\mu_{lam}$  and coarsening the elements until the  $y^+$  range falls into the recommended  $30 < y^+ < 300$ . It should be noted that for viscosities higher than

$\mu = 16\mu_{lam}$  caution must be taken when executing the current suggested technique of coarsening a mesh since very large wall cell sizes can lead to  $C_p$  distributions which heavily over predict the minimum pressure coefficient and separation point as was seen in Figure 3.11. However, if such a mesh is produced the curve can be manipulated to result in a more adequate  $C_p$  distribution through using the suggested modelling techniques in sections 3.3.3 to 3.3.5. The edge sizing used for the generation of the mesh and the total cell count is provided in Table 3.4 with the edges as defined in Figure 3.4. The mesh used is also shown in Figure 3.22.

**Table 3.4: Coarse mesh using  $\mu = 16\mu_{lam}$**

Edge	Element size (m)	Bias
A	0.007182	-
B	0.01	12
C	0.026	-
D	0.014	-
E	0.1	12
Total cell count	28 796 cells	



**Figure 3.22: Coarsened mesh using  $\mu = 16\mu_{lam}$**

As can be seen the current mesh (28 796 cells) is significantly coarser than the refined mesh in Figure 3.5 (115 412 cells) with a reduction of approximately 86 600 cells. The  $y^+$  ranges obtained from the model for the case of a smooth cylinder ( $\mu = 1\mu_{lam}$ ) and a cylinder with the applied wall viscosity technique is summarized in Table 3.5. It is clear from Table 3.5 that for the smooth case the  $y^+$  values lie outside the preferred  $y^+$  range.

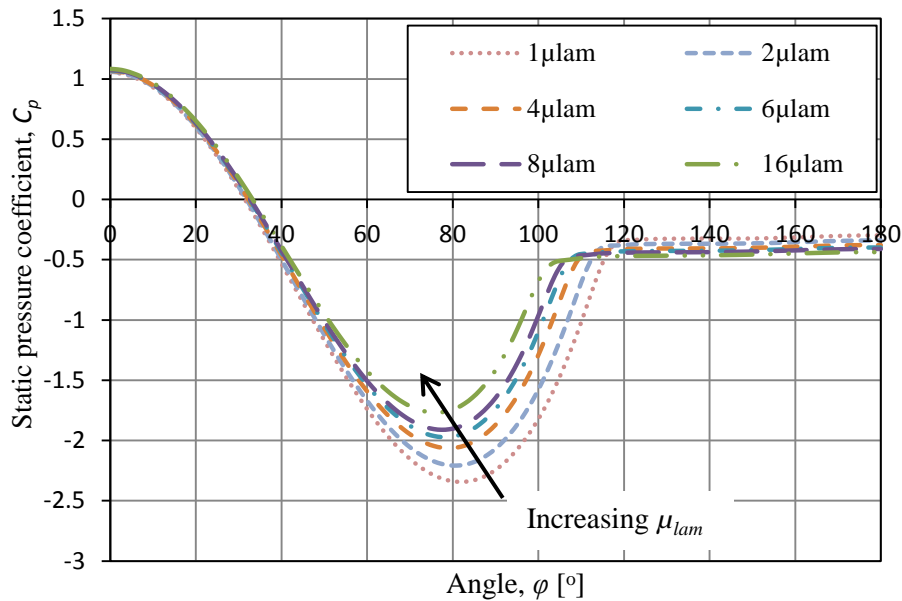
However, once the wall viscosity is numerically increased the  $y^+$  values start to drop and eventually fall within the suggested range. The corresponding  $C_p$  distributions generated by the model are shown in Figure 3.23. It is evident from the results that the trend of relieved suction pressures, earlier flow separation positions and lower wake pressures with increasing wall cell viscosity is

consistent with trends observed for both the surface roughening and wall viscosity variation in the previous sections. Furthermore this trend is also consistent with trends found in literature, with regard to the effect of surface roughening, as given in Figure 3.15 and Figure 3.16.

**Table 3.5:  $y^+$  range for the coarse mesh**

Specified wall viscosity	$y^+$ range
$1\mu_{lam}$ (smooth cylinder)	~200-1200
$2\mu_{lam}$	~100-700
$4\mu_{lam}$	~30-325
$6\mu_{lam}$	~30-225
$8\mu_{lam}$	~30-180
$16\mu_{lam}$	~30-90

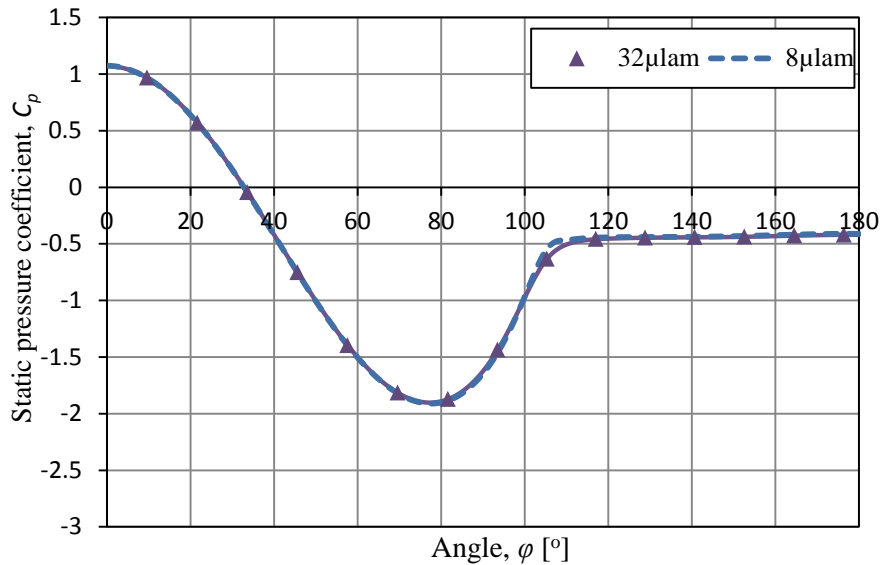
Although the  $\mu = 16\mu_{lam}$  case for the current model and the model used in section 3.3.5 do not result in similar  $C_p$  distributions with regard to  $C_{p,min}$  and  $C_{pb}$  values the result is however expected, since in the current model the region in which the laminar viscosity is increased is larger than in the refined model.



**Figure 3.23: Coarsened mesh using  $\mu = 16\mu_{lam}$ :  $C_p$  distributions**

Figure 3.24 shows a comparison, based on similar  $C_{p,min}$  values, of  $C_p$  distributions generated with the current coarse model ( $\mu = 8\mu_{lam}$ ) and the refined model in section 3.3.5 ( $\mu = 32\mu_{lam}$ ). From the figure it can clearly be seen that both models result in similar  $C_p$  distributions with the same predicted values for

important angles such as the angle of zero pressure ( $\varphi_0 \sim 33^\circ$ ) and angle of minimum pressure ( $\varphi_l \sim 75^\circ$ ). However, when comparing the angle of separation the coarse mesh has a more abrupt and defined separation point at approximately  $\varphi_N = 107^\circ$  whereas the refined model does not have such a defined separation point with separation occurring closer to  $\varphi_N = 110^\circ$ . However, both models predict the same wake pressure at approximately  $C_{pb} = -0.44$ .



**Figure 3.24: Comparison of the coarse mesh with the refined mesh**

In conclusion this section shows that mesh size can be significantly reduced by specifying a wall viscosity and sizing the elements until the  $y^+$  values fall within the desired range. Furthermore aside from a slight difference in the prediction of the separation point ( $\sim 3^\circ$ ) the coarse model provides an adequate representation for the pressure distribution around a cylinder and can also be used to calibrate numerical results such that it is more representative of experimental results.

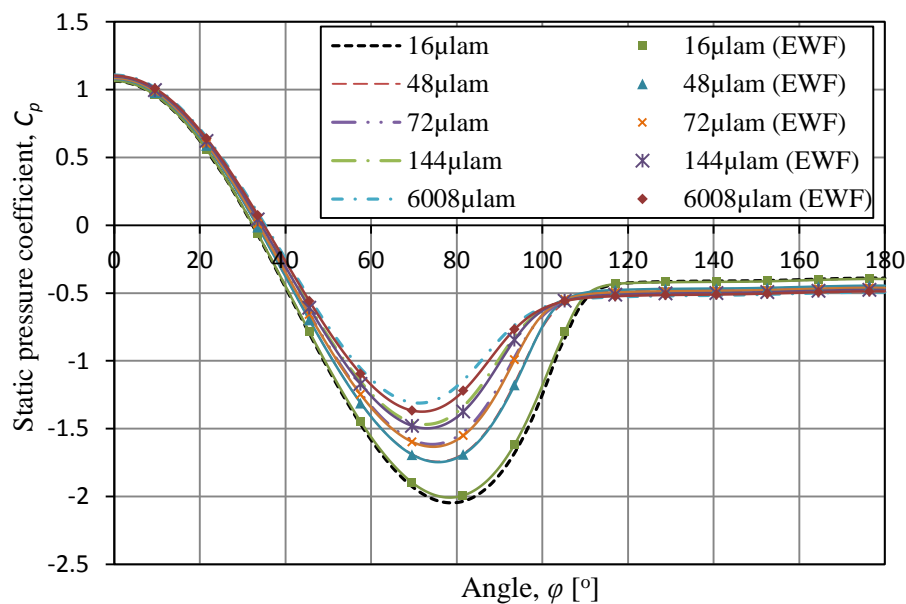
### 3.3.7 Low Reynolds number modelling for the wall viscosity variation

In the case of varying wall viscosity the wall adjacent cell  $y^+$  values can decrease to well below 30 and even approach 1. When this condition is reached the applicability of the standard wall function approach is questionable since the wall approximations for the standard wall function (SWF) is only valid and accurate in the range  $30 < y^+ < 300$ . However most current numerical CT models use standard wall functions and it is preferable to use this approach in the current model such that the findings can be directly applied to current as well as future numerical models.

In order to investigate whether there is a significant deviation between the prediction of the static pressure distribution using the standard wall function approach and a low Reynolds number modelling approach, where data is integrated across the viscous sub layer and not bridged, the simulations were

executed using Fluent's® enhanced wall function (EWF) approach. The enhanced wall function approach is a near-wall modelling method that combines a two-layer model with so-called enhanced wall functions (Fluent, 2013). Thus in the case of the standard wall function approach where the wall functions are technically only valid between  $30 < y^+ < 300$  the EWF allows for approximations of wall functions down to  $y^+ \sim 1$ . For the case when  $y^+ > 30$  the EWF formulation is exactly the same as the standard wall function approach and subsequently results in the exact same solution. During the surface roughness and cylinder rotation investigations the  $y^+$  values never reach values below  $y^+ = 30$  and the use of the EWF should not influence the results.

Figure 3.25 shows the comparison between the SWF and EWF approach for the wall viscosity variation case with Table 3.6 showing specific values for important angles and pressure coefficients.



**Figure 3.25: Comparison between the SWF and the EWF**

From the data it is clearly visible that the solutions generated by the SWF and EWF are extremely similar with the angle of zero pressure, angle of minimum pressure, separation angle and wake pressure values for each respective case the same. The only discrepancy is the values of minimum pressure. However up to  $\mu = 144\mu_{lam}$  the difference between the two sets of results are fairly small and can be considered insignificant. The largest deviation between the two models occur at  $\mu = 6008\mu_{lam}$  where the SWF seems to under predict the maximum suction pressure at the cylinder side leading to a  $C_{p,min}$  value of  $C_{p,min} = 0.06$  larger than the  $C_{p,min}$  value predicted by the EWF. This slight difference in  $C_{p,min}$  value subsequently leads to a slight difference in the pressure recovery stage, however once again the difference is not very large and the approximation provided by the SWF can be considered an acceptable representation for the pressure distribution as compared to the solution of the EWF.

**Table 3.6: Comparison between the SWF and the EWF**

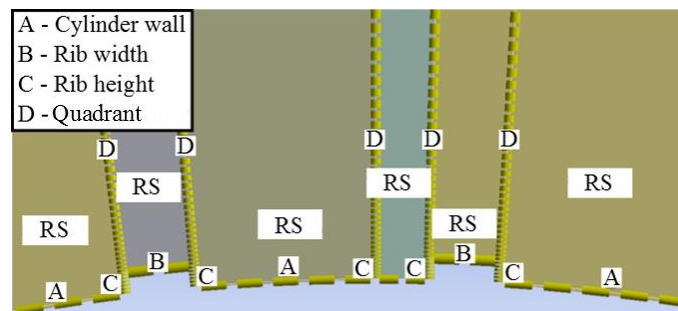
	$16\mu_{lam}$		$48\mu_{lam}$		$72\mu_{lam}$		$144\mu_{lam}$		$6008\mu_{lam}$	
	SWF	EWF	SWF	EWF	SWF	EWF	SWF	EWF	SWF	EWF
$\varphi_0$	32	32	33.6	33.6	33.6	33.6	34.8	34.8	34.8	34.8
$\varphi_l$	78	78	75.6	75.6	74.4	74.4	73.2	72.3	70.8	72
$\varphi_N$	120	118	115	114	112	111	110	110	105	105
$C_{pb}$	-0.42	-0.42	-0.45	-0.45	-0.48	-0.47	-0.49	-0.49	-0.5	-0.5
$C_{p,min}$	-2.046	-2.008	-1.742	-1.746	-1.616	-1.633	-1.468	-1.497	-1.331	-1.374
$\Delta C_{p,min}$ (%)	1.85		0.229		1.05		1.97		3.23	

### 3.4 Physical modelling of ribbed surfaces

In the previous sections of this chapter the effect of meridional ribs were represented through numerous numerical adjustments (surface roughness, cylinder rotation and wall viscosity) as an alternative to physically modelling of the ribs. In this section the effectivity and practicality of physically modelling these meridional ribs are investigated.

#### 3.4.1 Flow domain and mesh

In general, the geometry and boundary conditions used in the model are exactly the same as that described in section 3.1.1 unless otherwise stated, however due to the added complexity of ribbed structures on the cylinder circumference the mesh is slightly altered to provide sufficient resolution in the vicinity of the ribs. Figure 3.26 shows the edge sizing used for the meshing procedure. It can also be seen that the domain was further sub-divided into radial sections (RS) spanning either between ribs or along the rib width.

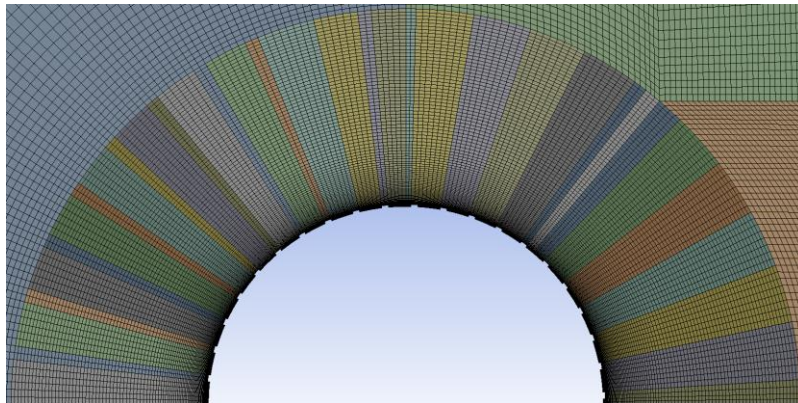
**Figure 3.26: Edges used for meshing**

The combination of radial sections, “*mapped face meshing*” for each section and edge sizing resulted in a mesh that permits excellent control in the near wall region as shown in Figure 3.27. It is found that without sub-dividing the BL mesh

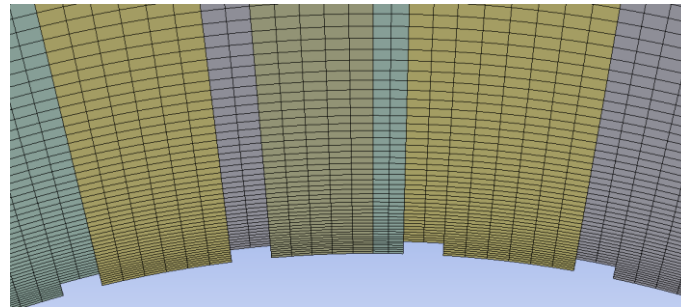


into radial sections the mesher is unable to provide adequate mesh resolution in the near wall region and struggles to map the regions between ribs. The use of the radial sections subsequently serves as a means to provide guidance to the mesher in order to create a uniform mesh.

Physical modelling of ribbed surfaces can however be extremely time-consuming especially when compared to the time it takes to generate a domain and mesh as in section 3.1 for the case of a smooth cylinder surface. Furthermore it is only possible to parameterize a ribbed case for a specific set amount of ribs, i.e. if it was decided to create a model with 36 ribs it would be fairly easy to change the rib spacing and rib height however if it was desired to add more ribs to the model the flow domain will have to be sub-divided again in order to take into account the new amount of ribs. In addition aside from the time-consuming nature of adding the ribbed structures there is also an increase in cell count due to the additional resolution that is necessary at the near wall region.



(a)



(b)

**Figure 3.27: Mesh with physical ribs: (a) Mesh surrounding the cylinder; (b) Near wall mesh**

### 3.4.2 Results for a half cylinder with 36 ribs

This section provides data resulting from an investigation in which meridional ribs, spaced  $a = 5^\circ$  apart resulting in a total of 36 ribs, are physically modelled around the half cylinder circumference. The mesh used consists of approximately

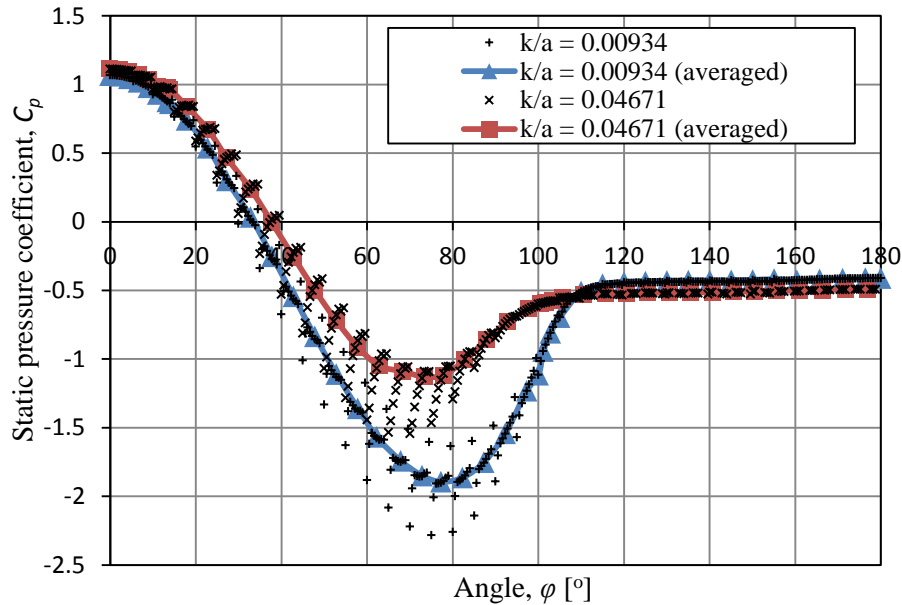
236 000 uniform quadrilateral cells which is an increase of approximately 120 600 cells compared to the smooth cylinder case. The degree of roughness is varied through changing the height ( $k$ ) of the ribs while keeping the spacing ( $a$ ) between the ribs and rib width ( $b$ ) constant (Figure 1.3). The focus of the investigation is subsequently more on the effect of varying the roughness parameter ( $k/a$ ) rather than recreating multiple ribbed cases. Nonetheless the rib geometries and spacing used is representative of actual ribs as found on NDCTs. Specifically the roughness parameters and rib geometries in the current investigation are based on roughness parameters and geometries used by Pröpper (1977) who measured pressure distributions around scaled NDCT models with meridional ribs. The subsequent details of the CFD model rib geometries and roughness parameters used as well as that used by Pröpper are summarized in Table 3.7.

**Table 3.7: Roughness values investigated**

Parameter	CFD model		Pröpper	
	Case 1	Case 2	Case 1	Case 2
Cylinder diameter, $d$ [mm]	457.2	457.2	247.52	247.52
Rib height, $k$ [mm]	0.93	0.186	0.5	0.1
Rib width, $b$ [mm]	1.86	1.86	1	1
$b/k$	2	10	2	10
Rib spacing, $a$ [°]	~ 5	~ 5	~ 5	~ 5
$k/a$	$4.67 \times 10^{-2}$	$9.34 \times 10^{-3}$	$4.63 \times 10^{-2}$	$9.26 \times 10^{-3}$
$k/d$	$2.03 \times 10^{-3}$	$4.06 \times 10^{-4}$	$2.02 \times 10^{-3}$	$4.04 \times 10^{-4}$

Figure 3.28 shows a static pressure distribution obtained around the circumference of the ribbed cylindrical surface for the case when the roughness parameter is  $k/a = 4.67 \times 10^{-2}$  (Case 1 in Table 3.7) and  $k/a = 9.34 \times 10^{-3}$  (Case 2 in Table 3.7). It can be seen that at locations where ribs are situated pressure jumps are observed. In addition it can also be seen that the higher rib height case leads to a greater distortion of the pressure distribution than the case with a lower rib height. In order to remove the pressure distortions and generate a clear representation for the pressure distribution around the cylinder an averaging procedure is applied.

However, before data points are averaged outlier data points located at the ends of the ribs are discarded leaving only closely clustered data points spanning the region between two consecutive ribs. The latter closely clustered data points are then averaged such that a single representative point is generated between each consecutive set of ribs.



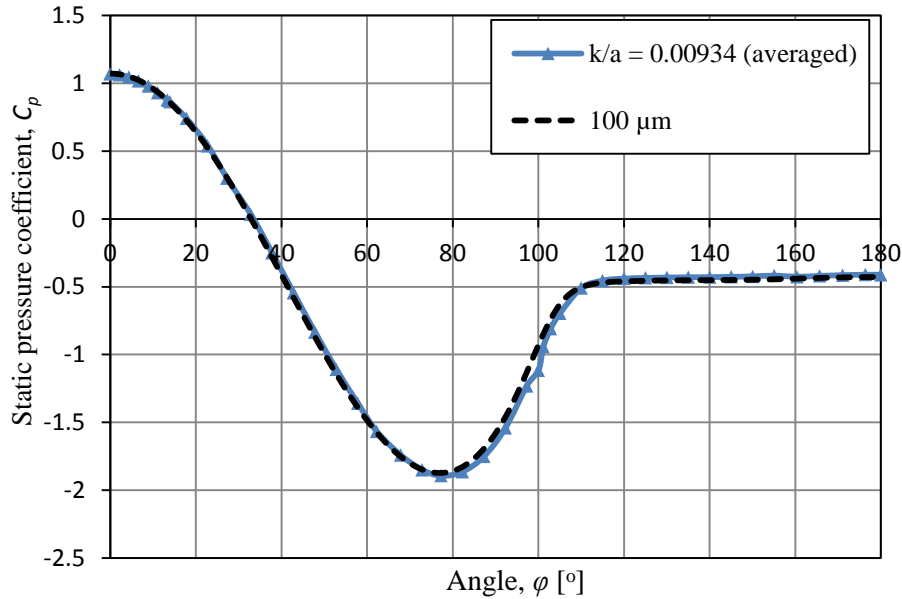
**Figure 3.28: Static pressure distributions around ribbed cylinders**

The resulting averaged pressure distributions are shown in Figure 3.28. It is observed that with a stepwise increase in the roughness parameter ( $k/a$ ) there is a subsequent decrease of  $C_{p,min}$  accompanied by a larger  $C_{pb}$  and earlier separation point which is consistent with what was observed in section 3.3. In addition the  $C_{pb}$  seems to tend towards a value of  $C_{pb} = -0.50$  as  $k/a$  increases.

Figure 3.29 shows the comparison between simulation results with similar  $C_{p,min}$  values obtained through physically modelling the ribs as well as through the use of the built-in surface roughness option in Fluent®. It can be seen that the averaged  $C_p$  curve distribution obtained through physical rib modelling is fairly similar to that obtained through numerically modelling the ribs with minimal differences between the two predictions.

However there are discrepancies when considering the pressure recovery stage between the two sets of data. In addition the physical rib model predicts a slightly delayed flow separation point when compared to the surface roughness model although both methods predict the same wake pressure of about  $C_{pb} = -0.45$ .

Subsequently it can be concluded that the numerical techniques developed to represent the overall effect meridional ribs have on the pressure distribution around a cylindrical structure are an effective and efficient alternative to physically modelling the ribs with similar  $C_p$  trends predicted between the two methods.



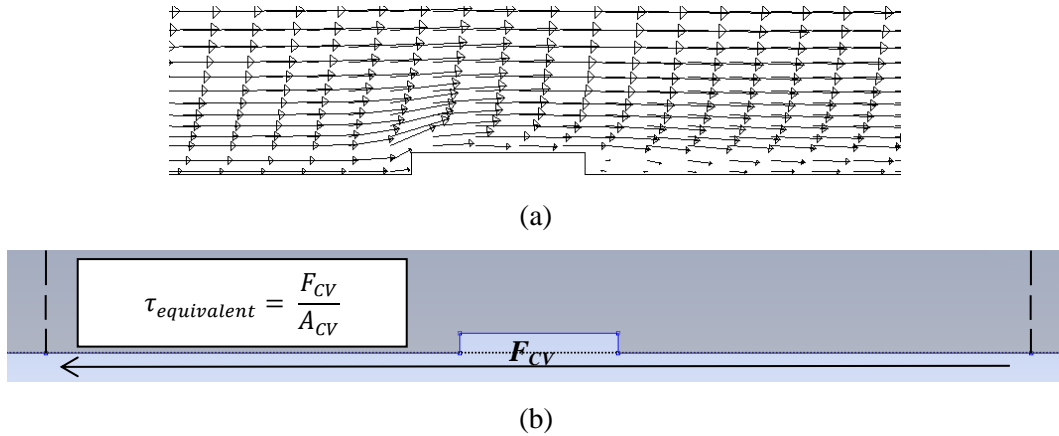
**Figure 3.29: Comparison between physical rib and surface roughness techniques**

### 3.5 Wall shear stress calibration using a flat plate model

In this section an attempt is made to calibrate the varying modelling methods analysed. Specifically wall shear stress ( $\tau_{wall}$ ) profiles over a flat infinite parallel plate are generated using each numerical method through either specifying a value for  $k_s$ ,  $\mu_{lam}$  or physically modelling ribs.

For the case of the equivalent sand grain roughness and wall viscosity methods similar  $\tau_{wall}$ -profiles are identified and the corresponding variables used are passed to the 2-D half cylinder model where the static pressure distributions around the cylinder circumference are compared. In the latter, through comparing the wall shear stress curves the total drag force over the plate surface is effectively compared.

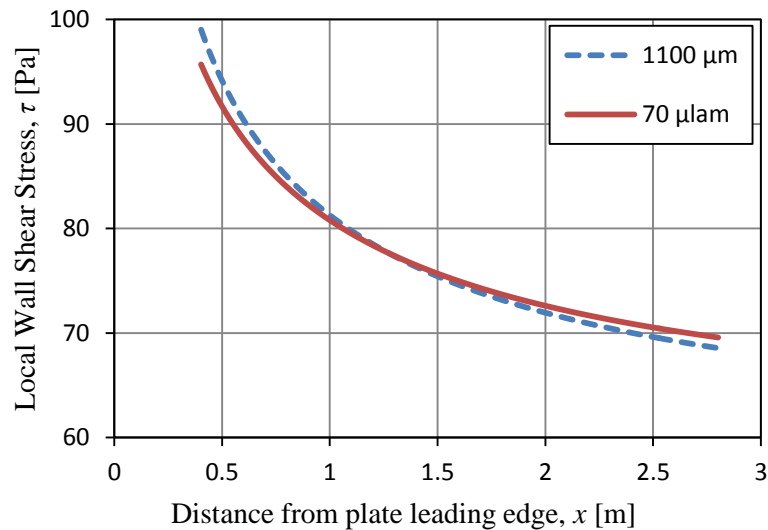
However, for the case of physically modelling the ribs the contribution of wall shear stress to the total drag force is small since pressure drag dominates. The latter is due to continuous flow separation and recirculation regions present in the vicinity of the ribs as shown in Figure 3.30 (a). Subsequently in the case of the ribbed plate, ribbed sections are divided into individual control volumes, as shown in Figure 3.30 (b), such that the total force ( $F_{CV}$ ) acting on each control volume could be obtained and an equivalent shear stress ( $\tau_{equivalent}$ ) can be determined. With the determination of the equivalent shear stress on each individual control volume a representative wall shear stress curve is generated over the entire length of the plate which can then be used to compare the ribbed case with the numerically modelled case(s).



**Figure 3.30: Flow around ribbed structure: (a) Velocity vectors; (b) Control volume**

The numerical model is developed using Fluent® and adhered to general accepted numerical criteria such as  $y^+$  values in the range  $30 < y^+ < 300$  for the smooth plate case. Furthermore the velocity at the domain inlet and all fluid properties are as specified in section 3.1.1.

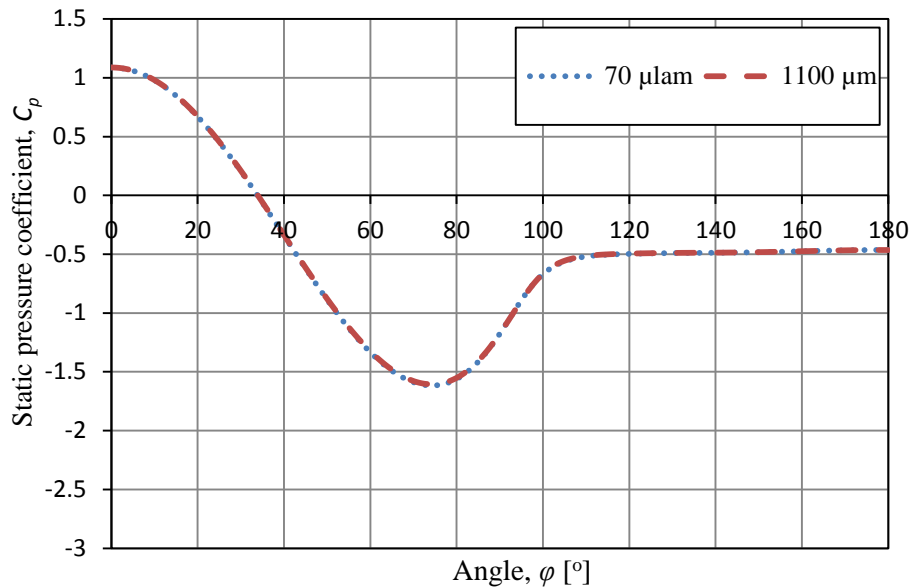
Figure 3.31 shows shear stress profiles over a flat plate for the case of specifying an equivalent sand grain roughness of  $k_s = 1100 \mu\text{m}$  and wall adjacent viscosity of  $\mu = 70\mu_{lam}$  respectively. From the figure relatively good agreement between the two curves can be seen with the curves corresponding almost exactly in the range of  $1 < x < 1.5$ . Since the latter shear profiles are extremely similar the applicable values for the sand grain roughness and wall adjacent viscosity are used in the 2-D half cylinder model to check whether or not the variables will predict similar static pressure distributions.



**Figure 3.31:  $\tau_{wall}$  profiles comparison for  $k_s = 1100 \mu\text{m}$  and  $\mu = 70\mu_{lam}$**

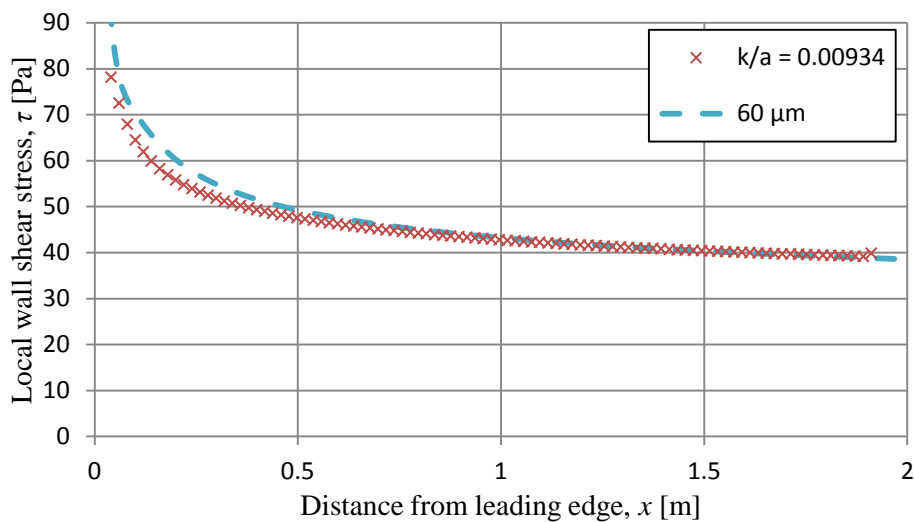
Figure 3.32 shows the respective static pressure distributions. It can clearly be seen that there is no difference between the two generated pressure distributions indicating that calibrating the equivalent sand grain height method and wall

adjacent viscosity method can be effectively achieved through matching flat plate wall shear stress profiles.



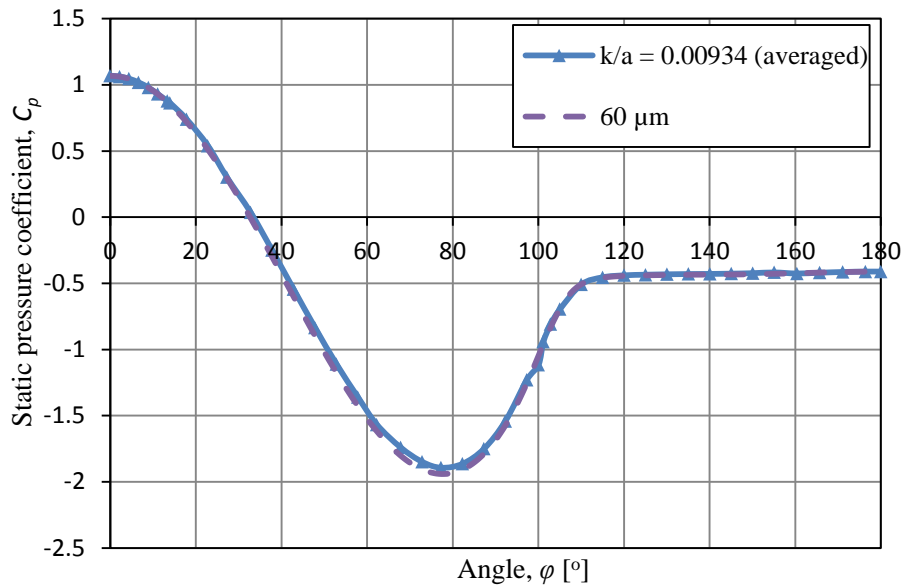
**Figure 3.32:  $C_p$  distribution comparison ( $k_s = 1100 \mu\text{m}$  and  $\mu = 70\mu_{lam}$ )**

In order to calibrate the sand grain roughness, or wall viscosity, and physical rib technique a slightly different approach had to be followed since the driving mechanism for drag force in the latter case is pressure drag and not friction drag. Consequently through following the procedure described earlier a representative equivalent shear profile across the ribbed plate was measured and compared to the wall shear stress distribution of the surface roughness technique. The measured shear stress profiles are shown in Figure 3.33 and it can be seen that there is good agreement between the profiles.



**Figure 3.33:  $\tau_{wall}$  curve comparison for  $k_s = 60 \mu\text{m}$  and  $k/a = 0.00934$**

Aside for some initial variation up to a plate length of  $x = 0.5$  m there is in fact no significant difference between the profiles. Since the profiles match the relevant parameters were passed to the 2-D half cylinder model to determine what pressure distribution will be generated. The resulting pressure distributions are shown in Figure 3.34.



**Figure 3.34:  $C_p$  distribution comparison:  $\mu = 60 \mu\text{m}$  and  $k/a = 0.00934$**

As can be seen in Figure 3.34 the generated pressure distribution with a surface roughness of  $k_s = 60 \mu\text{m}$  provides adequate representation for the case of the ribbed surface resulting in a relative roughness of  $k/a = 0.00934$ . Unfortunately with the current 2-D half cylinder model the  $k/a = 0.04671$  case  $C_p$  distribution falls just short of the achievable  $C_{p,min}$  range ( $C_{p,min}$  achievable = -1.30) of the developed techniques and subsequently the calibration cannot be performed. In conclusion this section has shown that matching shear stress curves, whether it is wall shear stress or an equivalent shear stress, result in similar pressure distributions when the applicable variables are used in the 2-D half cylinder models and the latter method can be used for effective calibration of pressure distributions.

### 3.6 Experimental investigation of the effect of surface roughening on pressure distribution

In this section experimental results for a roughened cylinder are presented. In addition all markers used on the curves represent measured data points unless otherwise stated. The experiments were conducted in the large suction wind tunnel test facility at the Mechanical and Mechatronic Engineering Department of Stellenbosch University in collaboration with Hill (2014). Tests were conducted on a single circular cylinder with a diameter of  $d = 200$  mm, at two wind velocities. The experimental setup, wind tunnel specifications and method of



obtaining the data is discussed in Appendix C. The main goal of the experiments is to validate the effect surface roughening has on the external pressure distribution around cylindrical structures. Furthermore the experimental data is also used to compare varying pressure distributions to distributions obtained with the 2-D numerical model developed in Chapter 3, with the same cylinder diameter as used in the experiment.

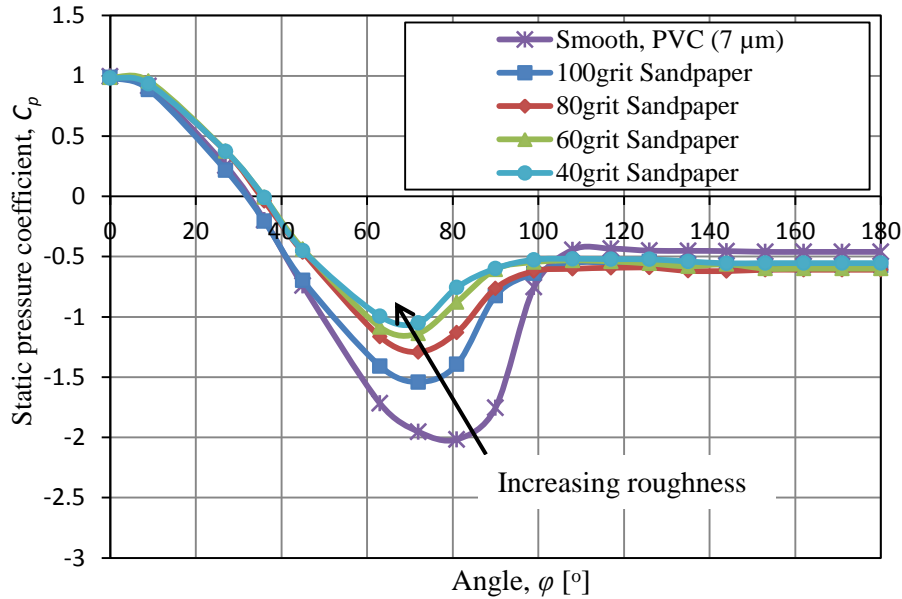
Due to wind tunnel constraints, trans-critical Reynolds numbers cannot be achieved in the experiments since for a cylinder diameter of  $d = 200$  mm the velocity will have to be in the vicinity of  $V = 390$  m/s in order to reach the trans-critical Reynolds regime boundary. Subsequently the investigation involved two wind speeds of  $V = 25$  m/s and  $33$  m/s resulting in Reynolds numbers of  $Re = 3.3 \times 10^5$  and  $4.3 \times 10^5$  respectively. Furthermore once roughening is applied to the cylinder surface, and the  $k_s/d$  parameter increases, the critical Reynolds number should theoretically decrease according to Achenbach as shown in Figure 1.4 (a). The latter then suggests that although the  $Re$ -numbers, based on the smooth cylinder diameter, reside in the critical and super-critical regime, respectively, the addition of surface roughening may result in the simulation of trans-critical Reynolds regimes.

It should be pointed out that if the tests were performed at the maximum wind velocity ( $V = 90$  m/s) a larger Reynolds number would be achieved however this would place the flow in the unstable upper transitional region (Table 1.1) which is undesirable due to limited knowledge of the flow behaviour in this regime. In addition the chosen Reynolds numbers are similar to past investigators and fall within ranges which have been extensively studied. Specifically Niemann (1971) investigated the pressure jumps meridional ribs cause on a  $d = 200$  mm diameter cylinder at  $Re = 3.3 \times 10^5$  and Achenbach (1970) investigated the pressure distribution around a rough circular cylinder with  $k_s/d = 110 \times 10^{-5}$  at  $Re = 4.3 \times 10^5$ . Figure 3.35 shows the experimental results obtained for varying sand grain roughness heights. In addition the equivalent surface roughness heights for the individual sand paper grits, as given by CAMI standards, are provided in Table 3.8.

**Table 3.8:  $k_s$  values of the sand paper grit used**

CAMI grit	Grade	$k_s$ [ $\mu\text{m}$ ]	$k_s/d$
40	Coarse	428	$\sim 214 \times 10^{-5}$
60	Medium	268	$\sim 134 \times 10^{-5}$
80	Medium	192	$\sim 96 \times 10^{-5}$
100	Medium	141	$\sim 70.5 \times 10^{-5}$



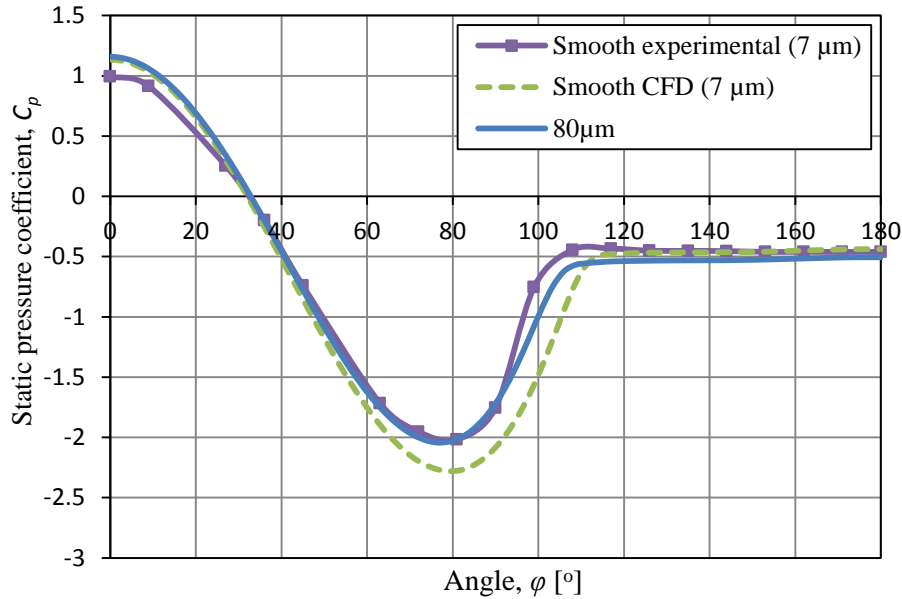


**Figure 3.35: Sand paper roughening at  $Re = 3.3 \times 10^5$**

It can clearly be seen that as the degree of surface roughness is increased there is a corresponding lower absolute  $C_{p,min}$  value which indicates suction pressure relief on the cylinder side. Furthermore it is observed that at higher roughness values there is a corresponding earlier separation point and larger negative wake pressure. In addition it is interesting to note that the wake pressure tends to a value in the vicinity of  $C_{pb} = -0.45$  to  $-0.55$  which is similar to what was observed in the CFD model results in Figure 3.14 and in the measured distributions of Jones et al. in Figure 3.7 (c). Furthermore this trend of an upward shift in  $C_{p,min}$  and downward shift of  $C_{pb}$ , on the  $C_p$  curve, with increasing roughness is consistent with observations made by Cüven et al. in Figure 3.15 and Niemann in Figure 3.16. Thus the  $C_p$  trend behaviour is similar to that generated by the CFD models which serves as verification for the effect surface roughening has on the static pressure distribution around cylinders.

The results for the tests done at  $Re = 4.3 \times 10^5$  are omitted in this section since it resulted in similar trends as the  $Re = 3.3 \times 10^5$  case. However, the results are tabulated in Appendix C.

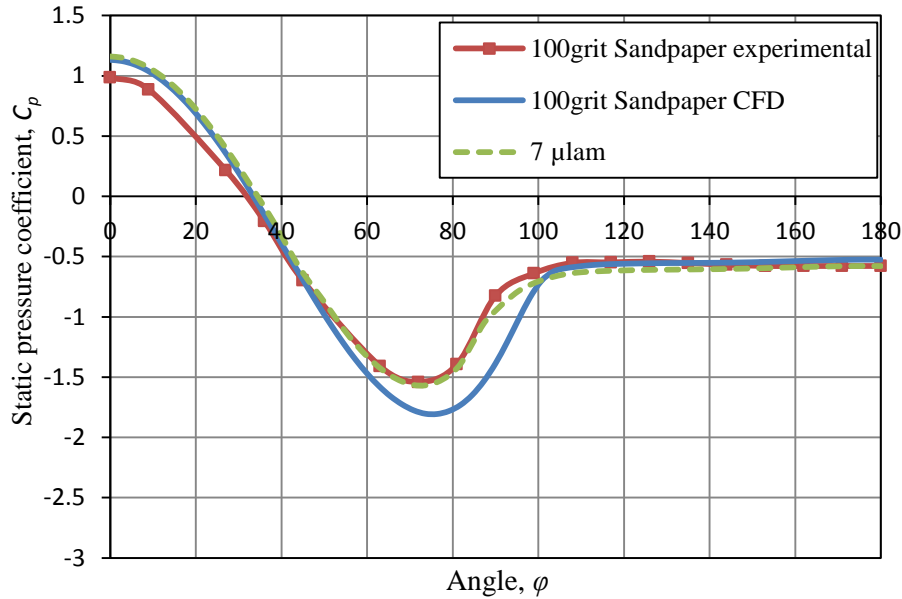
Figure 3.36 shows a comparison between the experimentally measured and numerically generated pressure distributions for the smooth cylinder case. From the results it can clearly be seen that the CFD model does not accurately predict the smooth case with an observed larger negative pressure and delayed separation point. However, it is interesting to note that the CFD model does predict a similar wake pressure of approximately  $C_{pb} = -0.45$  as in the experimental results. In an attempt to calibrate the CFD model such that it better represents the overall pressure distribution the surface roughening technique suggested in section 3.3.3 is employed with a specified equivalent sand grain roughness height of  $k_s = 80 \mu\text{m}$ .



**Figure 3.36: Comparison of smooth cylinder experimental and numerical results at  $Re = 3.3 \times 10^5$**

From the results it can be seen that the modified CFD model results in a slightly better approximation for the pressure distribution with regard to the minimum pressure and separation point. However, with the addition of the surface roughness the CFD model now predicts a slightly larger wake pressure of  $C_{pb} = -0.51$  as compared to the experimentally measured  $C_{pb} = -0.45$ . It is useful to note that in the current regime there is a transition from a laminar to the turbulent boundary layer, as explained in Chapter 1, as opposed to a fully turbulent boundary layer in the trans-critical regime. The latter is important to take into account since the  $k-\epsilon$  Realizable turbulence model is developed for fully turbulent boundary layer flows and does not take into account the transition from a laminar to turbulent boundary layer state, thus the use of the latter turbulence model already has a negative impact on the simulation of the flow around the cylinder at the experimental Reynolds number.

Furthermore with a similar procedure used to generate the  $C_p$  distributions in Figure 3.36 the  $\mu_{lam}$  method (section 3.3.5) is employed to determine an adequate representation for the 100 grit sand paper case as shown in Figure 3.37. From the results it is clear that using a similar sand grain roughness, to represent the 100 grit sand paper in the numerical model, the numerical model does not predict the same pressure distribution as the experimental case. However through adjusting the pressure distribution using one of the techniques developed,  $\mu = 7\mu_{lam}$  in the wall adjacent cells, a significantly better approximation can be achieved. Comparing the adjusted  $C_p$  trend to the measured trend it can be seen that numerous characteristics are the same such as the angle and value of minimum pressure, angle at which separation occurs and the wake pressure.



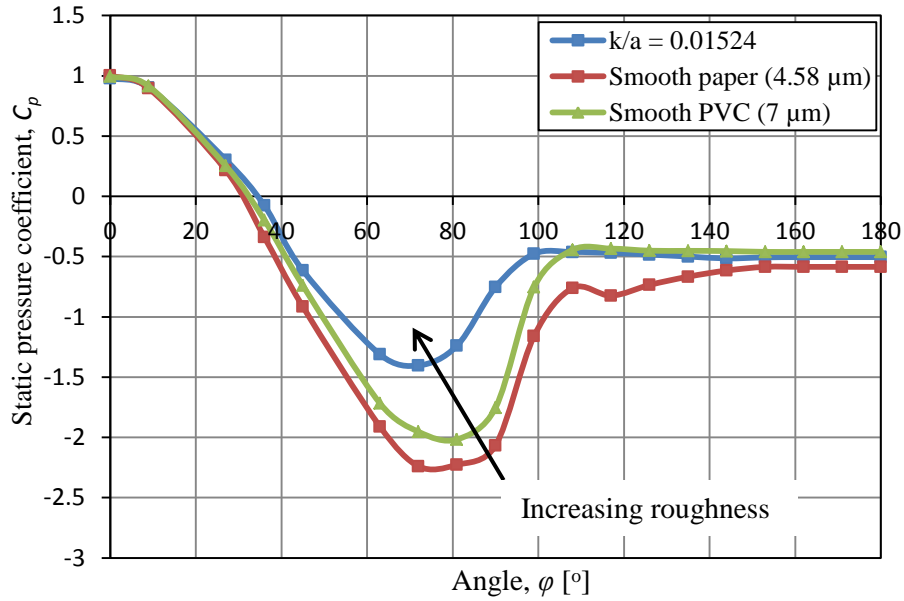
**Figure 3.37: Comparison of 100 grit sand paper experimental and numerical results at  $Re = 3.3 \times 10^5$**

In addition to sand paper roughening of the cylinder surface the case of adding physical ribs on the cylinder surface was also investigated. The chosen rib geometries are provided in Table 3.9 and are based on geometries used by Niemann (1971) who investigated the effect various rib geometries have on pressure distortions along the circumference of a circular cylinder. It should be noted that additional rib geometries were also investigated however, since all the cases resulted in the same roughness parameter,  $k/a = 0.01524$ , there were little to no major differences in the predicted  $C_p$  trends. The latter additional data is provided in Appendix C.

**Table 3.9: Rib geometry investigated**

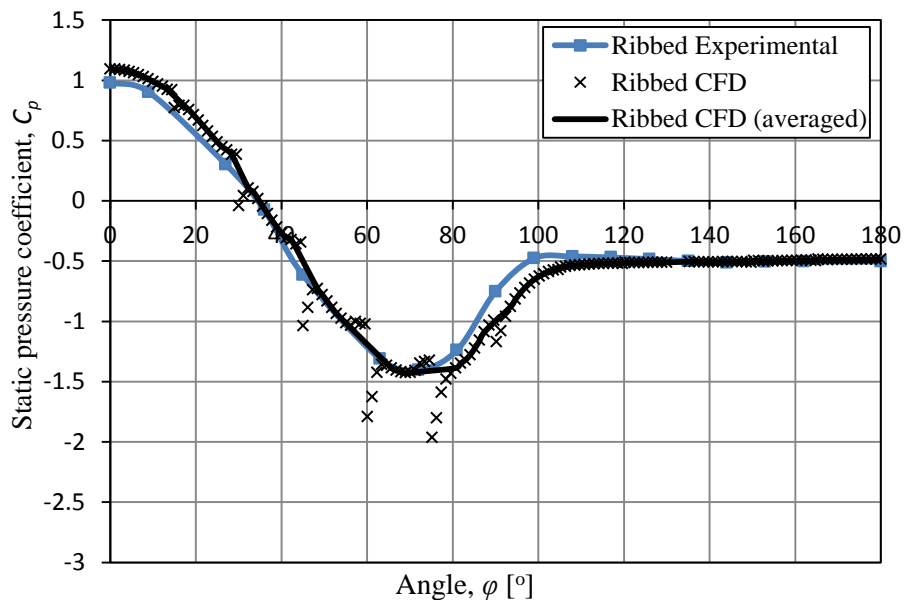
Rib height, $k$ [mm]	Rib Width, $b$ [mm]	$b/k$	Rib spacing, $a$ [mm]	$k/a$
0.4	1	2.5	26.24	0.01524

Figure 3.38 shows the measured pressure distribution for the ribbed and smooth cylinder cases. However, in this smooth case paper was wrapped around the cylinder periphery in order to eliminate the added effect the paper roughness might have on the pressure distribution. The latter was needed since the ribs were first attached to paper and then to the cylinder surface as described in Appendix C. It can be seen that through applying physical ribbed structures to the cylinder surface there is an upward shifting trend of the general  $C_p$  distribution. More specifically there is a significant relief of suction pressure and earlier separation point observed along with a larger negative wake pressure.



**Figure 3.38: Experimental data for ribs at  $Re = 3.3 \times 10^5$**

The latter mentioned trends are also in accordance with trends observed in Figure 3.15 and Figure 3.16, verifying the effect rib roughening has on the pressure distribution. Furthermore the Niemann ribbed case was also simulated using a similar ribbed cylinder model as the one developed in section 3.4. In addition using the averaging procedure described in section 3.4.2 an averaged pressure distribution for the CFD ribbed cylinder is generated and compared to the experimental results in Figure 3.39.



**Figure 3.39: Comparison for ribbed case at  $Re = 3.3 \times 10^5$**

In general important angles such as the angle of zero pressure ( $\varphi_0 \sim 34.5^\circ$ ) and angle of minimum pressure ( $\varphi_l \sim 72^\circ$ ) correspond extremely well with no significant difference between the measured and numerically generated data. However, when considering the angle of separation it is seen that the numerical model predicts a slightly delayed separation at approximately  $\varphi_N \sim 105^\circ$  compared to the measured separation point at  $\varphi_N \sim 100^\circ$ . Interesting is the fact that both the measured experimental results and the numerical model predicts a similar wake pressure in the region of  $C_{pb} = -0.50$ . In short the numerical model predicts the pressure distribution extremely well up to the angle of minimum pressure however; thereafter the numerical model fails to predict the pressure rise accurately up to the point of separation. However, from the separation point onwards the numerical model again provides a fairly adequate representation for the pressure distribution. Furthermore despite the weak prediction of the pressure rise the numerical model does provide an adequate overall representation of the general pressure distribution and can be used for an effective parametric study to gain better understanding of how flow disturbances affect the pressure distribution around the cylinder.

In addition the wall shear stress calibration method developed in section 3.5 is now used to determine the equivalent  $\mu_{lam}$  parameter that should be used to generate a similar  $C_p$  distribution as the ribbed case. It should be kept in mind that for the calibration, numerical models are used to determine shear stress profiles over a flat plate. However, the flow conditions in the numerical models are set to the same experimental conditions such that the state of the free-stream flow is similar. Figure 3.40 shows the resulting calibration attempt.

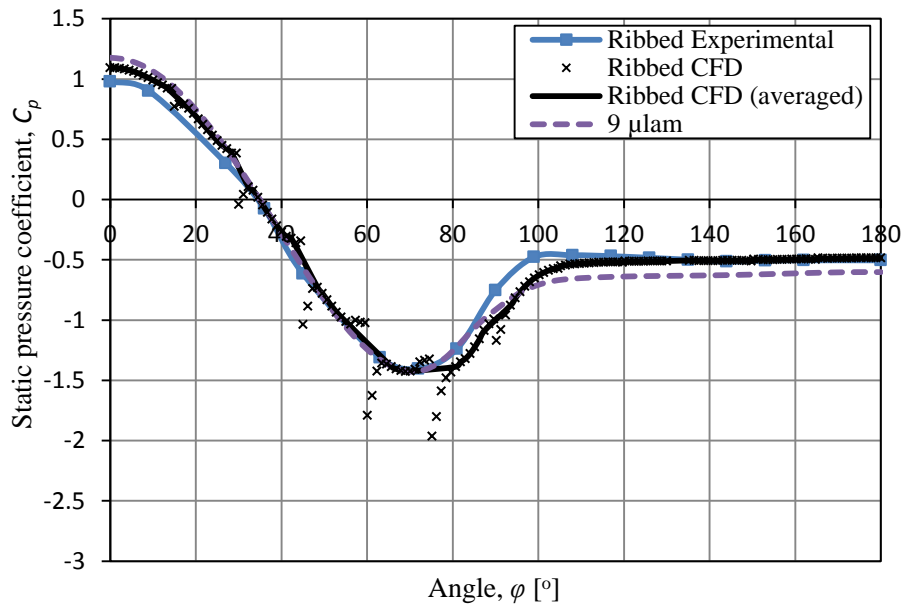


Figure 3.40: Calibrated rib case at  $Re = 3.3 \times 10^5$

From the data it is clear that the calibrated case provides an adequate representation for the  $C_p$  distribution up to the point of minimum pressure with the angle of minimum pressure, value of minimum pressure and the angle of zero pressure corresponding extremely well with insignificant differences. However, from the point of minimum pressure onwards the calibrated curve follows the ribbed experimental case up to approximately  $87^\circ$  where after separation is predicted at approximately  $\varphi_N = 100^\circ$  compared to the  $\varphi_N = 105^\circ$  of the ribbed CFD model. In addition due to this earlier separation the predicted wake pressure is also significantly lower. Although when compared to the experimental data the separation point predicted by the calibrated model can be considered more accurate. Again it should be kept in mind that the  $k-\varepsilon$  Realizable model was developed for fully turbulent boundary layer flow which may not be the case for the current  $Re$ -numbers under investigation.

### 3.7 Conclusion

Using Fluent® a 2-D CFD model for the flow around an infinite cylinder is successfully developed. The developed model is found to correlate well with available data from literature and is deemed fit for use in a parametric study in order to identify viable methods for re-creating the effect that wind ribs have on cylindrical structures. Three methods are identified for the momentum adjustment at the cylinder surface based on the definition of shear stress:

1. Specifying an equivalent sand grain roughness for the cylinder surface.
2. Specifying an angular velocity for the cylinder wall.
3. Numerically increasing the laminar viscosity in the wall adjacent cells.

It is observed that by increasing the sand grain roughness of the cylinder surface there is a subsequent upward shifting adjustment of the  $C_p$  trend with relieved minimum pressures on the cylinder side as well as increased wake pressures (Figure 3.14). In addition it is found that the surface roughening technique only allows  $C_p$  curve adjustment of up to  $C_{p,min} = -1.58$  with further increases in equivalent sand grain roughness leading to weak wall function approximations.

The angular velocity variation method on the other hand resulted in improved adjustment of the  $C_p$  trend with  $C_{p,min}$  values reaching the vicinity of  $C_{p,min} = -1.0$  (Figure 3.18). However at large angular velocities the pressure distributions seemed unstable and it was difficult to maintain the windward stagnation pressure at approximately 1.

Through increasing the laminar viscosity in the wall adjacent cells, rigorous adjustment of the  $C_p$  trend was achieved with  $C_{p,min}$  values reaching  $C_{p,min} = -1.30$  (Figure 3.20). This adjustment is an improvement compared to the surface roughening method but is still not as effective as the angular velocity method. However the pressure distribution does not seem to become unstable as in the angular velocity case. Furthermore, adjustment saturation is observed at large values of laminar viscosity. In addition it was shown that through exploiting the

fact that the increase of wall adjacent viscosity leads to drastically reduced  $y^+$  values a coarser mesh can be generated for investigation purposes.

All three investigated techniques resulted in pressure trends which correlate well with data in literature and all three techniques predicted similar pressure distributions when compared to each other based on similar  $C_{p,min}$  values.

The practicality of physically modelling meridional ribs is also investigated and it was found that this method is time consuming. It is observed that increasing the rib roughness parameter does indeed result in  $C_p$  trend adjustment (Figure 3.28) and that the  $C_p$  trends compare well to results generated using the developed numerical techniques. Furthermore it is shown that through shear stress curve comparisons all models can be effectively calibrated such that for a specific set of parameters ( $k_s$ ,  $\mu_{lam}$  and  $k/a$ ) every individual variable generates the same  $C_p$  trend.

Lastly experimental tests are performed and the effect of surface roughening, for both the sand paper and meridional rib case, showed a trend of relieved suction pressure on the cylinder side, earlier flow separation point and a larger wake pressure. The latter trends are found to be in accordance with experimental data from various researchers and confirmed the effect surface roughening has on the pressure distribution around a cylinder.

In addition it is shown that the CFD model for the non-ribbed cylinder case, without using any of the developed adjustment techniques, does not provide an adequate representation for the pressure distribution. However, when applying the adjustment technique(s) developed in section 3.3 a better representation for the pressure distribution can be generated. Furthermore it is shown that the ribbed cylinder CFD model does indeed provide an adequate representation for the  $C_p$  trend although there are some shortcomings in the pressure rise region. In addition it is also demonstrated that the wall shear stress calibration technique developed can be successfully used to determine the equivalent adjustment parameter albeit  $k_s$  or  $\mu_{lam}$ .

## 4 Numerical analysis of flow around a finite cylinder

In this chapter a three dimensional (3-D) CFD model for a finite cylinder is developed using the 2-D model in section 3. The 2-D domain is extruded in the  $z$ -direction in order to generate a model which takes into account three dimensional effects. The model is then used to perform a parametric study in order to investigate the effect of using a height to diameter ratio, the tip effect of a finite cylinder on static pressure distribution around the cylinder and the general variation of static pressure distribution at varying heights around the cylinder periphery. The techniques developed for meridional rib modelling in the previous section are also applied to the 3-D model in order to investigate the effect of roughening on static pressure distributions along the cylinder height.

### 4.1 Geometry, flow domain, boundary conditions and mesh

Since the 3-D finite cylinder model is derived from the 2-D model developed in section 3 the cylinder geometry is exactly the same as in the 2-D case with the addition of a  $z$ -component in the flow domain.

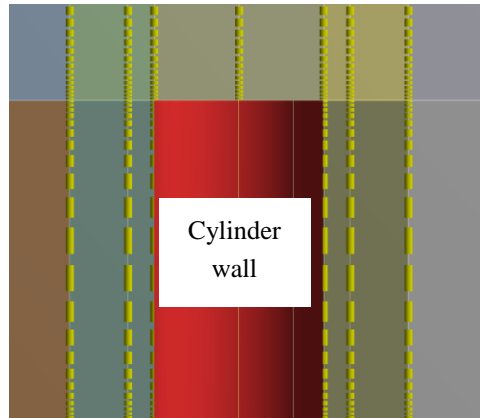
This additional  $z$ -direction sizing is shown in Figure 4.1 along with an example mesh. The edge sizing along the cylinder wall is biased towards the ends of the cylinder in order to provide finer resolution near the top and bottom of the cylinder respectively with coarser elements toward the middle of the cylinder. The edge sizing from the top of the cylinder towards the top domain boundary is set to be biased toward the cylinder top in order to capture possible tip effect phenomena. Furthermore the wake region edge sizing was slightly coarsened in an attempt to reduce the number of cells used.

This coarsening of the wake is allowed since the current model is not time dependent and it was found in section 3 that coarsening of the wake has an insignificant effect on the steady state solution. However it should be noted that when drastically varying the element sizing in the near wake region (enclosed in the BL mesh) the solution can and will be significantly affected. Although there is some room for mesh coarsening w.r.t the cylinder mesh divisions which can be drastically coarsened without significant changes in  $C_p$  curve trends as was shown in section 3.3.2.

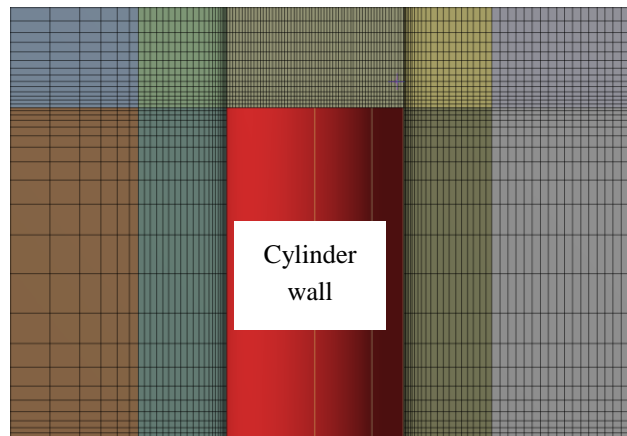
The final mesh used for the 3-D finite cylinder cases consist of uniform quadrilateral elements with the mesh sizing and number of cells used as provided in Appendix E. Due to the heavy computational load of the model, the computations were performed using University of Stellenbosch's Rhasatsha High Performance Computing capabilities (<http://www.sun.ac.za/hpc>). Furthermore since the focus of this study is to investigate whether a coarse model can be used for adequate representation of the external pressure distribution around cylindrical



structures a model with significantly less elements will also be developed. The idea is that the latter model along with the use of  $C_p$  trend adjustment techniques developed in section 3 will then allow adequate pressure distributions at a more economic computational cost.



(a)



(b)

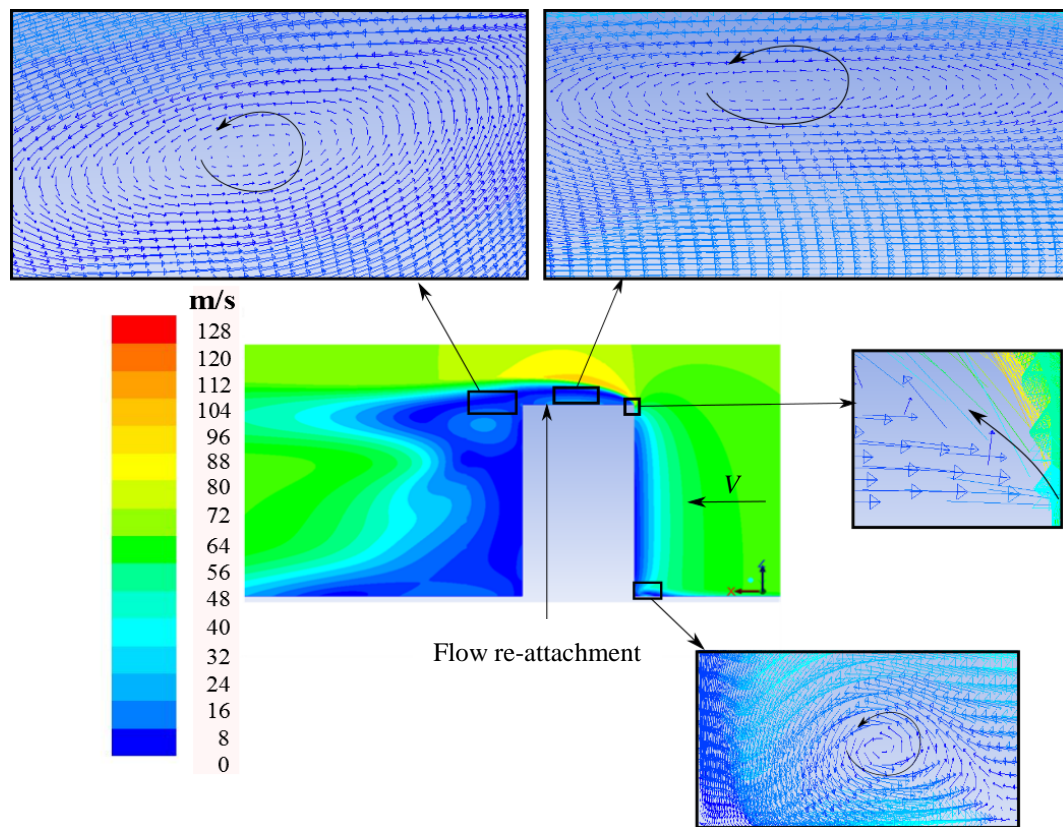
**Figure 4.1: 3-D cylinder mesh along the symmetry plane: (a) z-direction mesh edges for sizing; (b) Sample mesh**

## 4.2 Pressure distribution variation along the cylinder height

This section investigates how the static pressure distribution around a solid finite cylinder varies as it is measured at different heights along the cylinder surface. The cylinder considered has a height to diameter ratio ( $h/d$ ) of 1.88 with the rest of the geometry the same as in section 3. Multiple cases for the cylinder are investigated including: flow around a smooth finite cylinder, flow around a solid finite cylinder with surface roughening and finally flow through and around a smooth and rough finite hollow cylinder with an inlet height at the cylinder base.

### 4.2.1 Flow around a solid finite cylinder

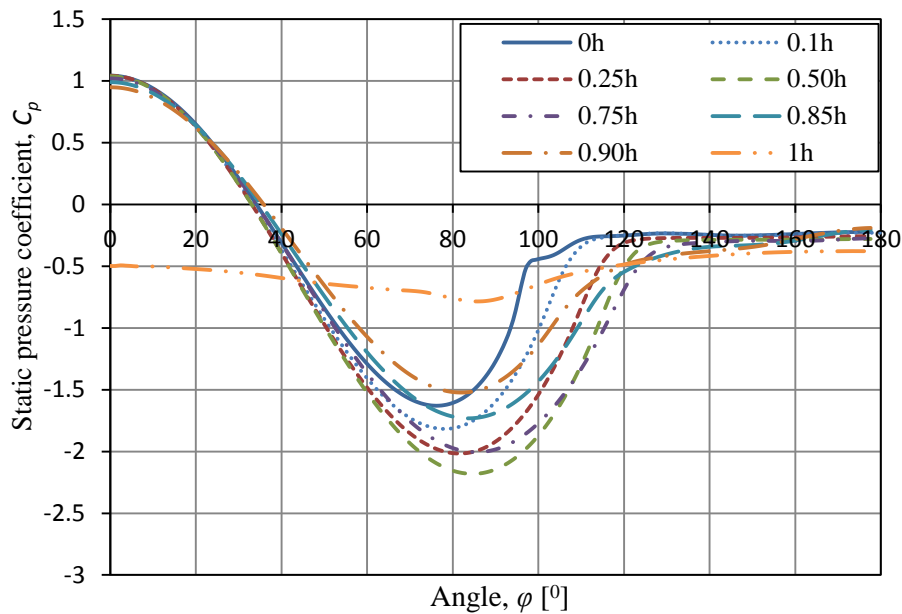
Figure 4.2 shows velocity contours along the symmetry plane for airflow around a smooth solid finite cylinder. From these contours generally encountered flow phenomena can be identified in an attempt to validate the flow field around the cylinder. Most notable is the flow separation at the leading edge of the cylinder tip and the subsequent re-attachment of the flow in the middle vicinity of the cylinder top as well as the well-known tip-effect which forms vortices directly downstream of the cylinder tip in the wake area. Furthermore, other phenomena such as the vortices at the upstream and downstream base of the cylinder can also be identified. All these flow visualizations are consistent with observations made by Majumbar and Rodi (1989) as well as Rostamy et al. (2012) which indicates that the model does indeed correctly represent the expected flow field around the cylinder.



**Figure 4.2: Velocity contours and vectors along the centreline of the smooth solid finite cylinder**

$C_p$  distributions obtained from the simulation results are shown in Figure 4.3. The pressure distributions shown are measured from the base of the cylinder ( $0h$ ) to the free end of the cylinder ( $1h$ ). It is found that as the pressure distribution is measured from the base of the cylinder toward the middle ( $0.50h$ ) of the cylinder height there is a significant increase of suction pressure on the sides of the

cylinder. This is expected and is ascribed to the large shear forces the airflow encounters at the no-slip ground surface which causes the airstream to slow down in the region at the cylinder base, i.e. the shear forces increase the flow resistance at the cylinder base. As the airstream moves further away from the cylinder base this flow resistance decreases. On the  $C_p$  distribution this can be seen when comparing the acceleration span at the base of the cylinder ( $\sim 0^\circ$  to  $74^\circ$ ) to the acceleration span at  $0.50h$  ( $\sim 0^\circ$  to  $84^\circ$ ). It is also interesting to note that as the acceleration span around the cylinder periphery decreases the flow separation point shifts further upstream which is similar to the effect surface roughening has on the pressure distribution.

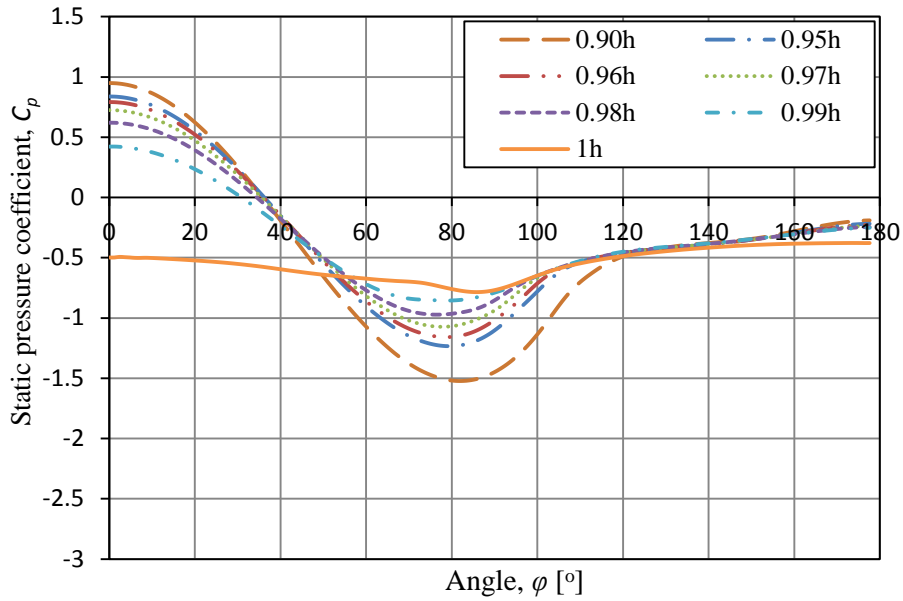


**Figure 4.3:  $C_p$  distribution around a smooth solid finite cylinder**

However from the middle of the cylinder height toward  $0.90h$  of the height there is a decrease of suction pressure on the cylinder side. This variation of pressure distributions at different sections along the cylinder height was also observed by Lupi (2013) who divided the regions into the tip region, normal region and low region. Ultimately the general pressure distribution trend breaks down as the free end of the cylinder is reached and a near constant pressure is measured at the cylinder top as can be seen in Figure 4.4.

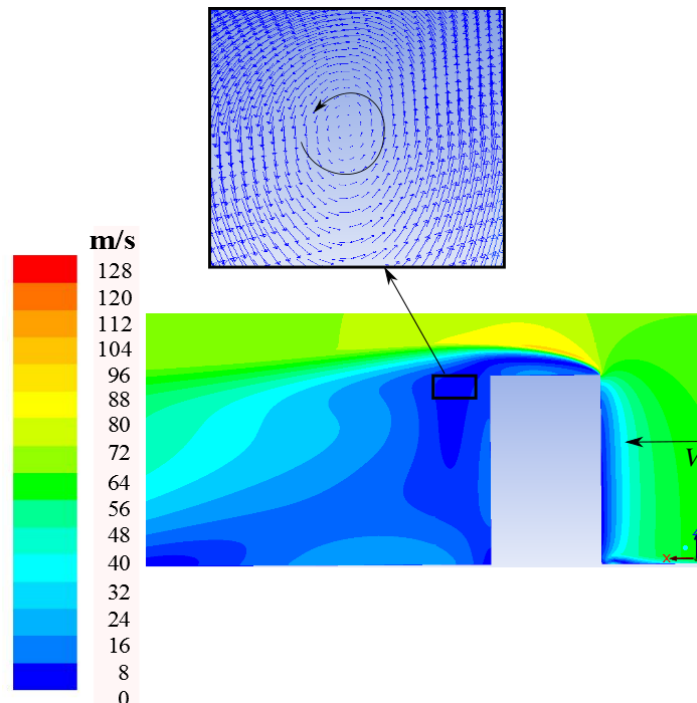
This near constant pressure at the cylinder top end is mainly due to the recirculation region on the top surface of the cylinder which results from flow separation at the upstream tip and the subsequent re-attachment of the flow to the cylinder top. Useful to note is that midway up the cylinder height the pressure distribution is extremely similar to a pressure distribution encountered for 2-D flow past a cylinder. In fact if the cylinder height is increased and the effects of

the ground surface and cylinder free end become less severe the pressure distribution will become extremely similar to the 2-D case.



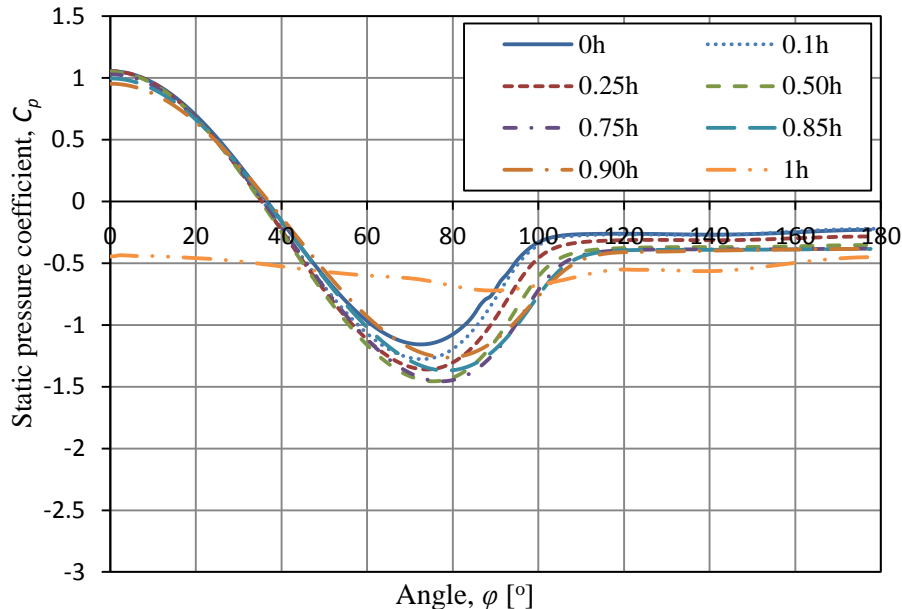
**Figure 4.4:  $C_p$  distribution near the smooth solid finite cylinder top end**

Figure 4.5 shows the velocity contours around the solid finite cylinder with a specified surface roughness of  $k_s = 500 \mu\text{m}$  followed by the obtained pressure distributions along different heights of the cylinder in Figure 4.6 and Figure 4.7.



**Figure 4.5: Velocity contours of the rough ( $k_s = 500 \mu\text{m}$ ) solid finite cylinder**

Considering the velocity contour plot it can be seen that roughening the surface results in changes in the wake region of the cylinder. Most notable is the recirculation region which is now located immediately below the tip of the cylinder in the wake region, whereas it was observed to be slightly higher in the smooth cylinder case. In general the roughened surface also results in significantly lower velocities in the wake region compared to larger velocities present for the smooth case.

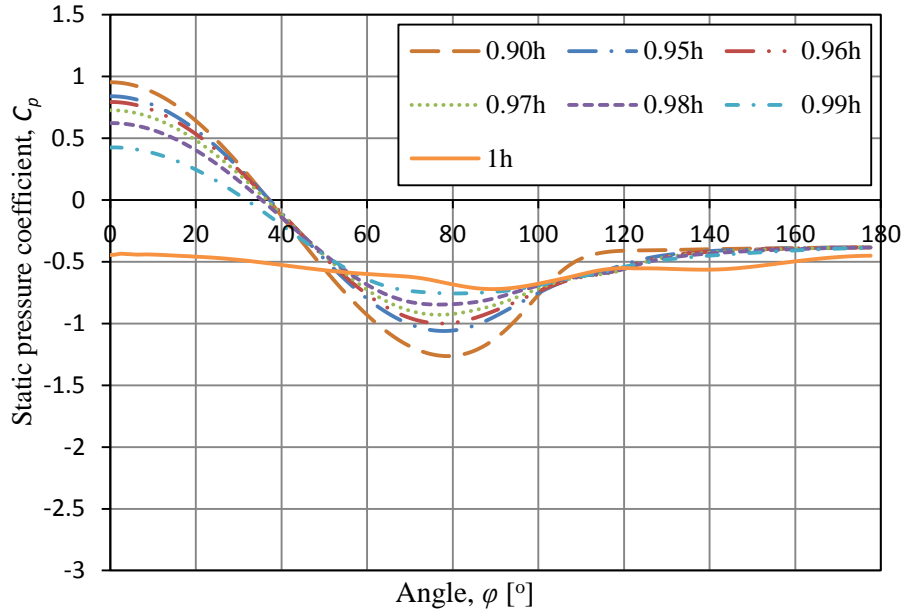


**Figure 4.6:  $C_p$  distribution around a rough ( $k_s = 500 \mu\text{m}$ ) solid finite cylinder**

In addition as in the smooth cylinder case there is a significant increase of suction pressure on the cylinder side as measurements are taken from the base of the cylinder ( $0h$ ) to  $0.5h$  which can be ascribed to the large shear forces present at the ground level. Again from  $0.5h$  to  $0.9h$  the suction pressure on the cylinder side decreases and the general pressure distribution trend breaks down as the tip of the cylinder is reached.

At the tip height a near constant pressure is again present around  $C_p = -0.5$  which is similar to the smooth case which approximately also centres on  $C_p = -0.5$ . When comparing the trends of the smooth case to that of the rough case it can be seen that in the rough case the  $C_p$  trends have relieved suction pressures ( $C_{p,min}$  values) and earlier separation points which is consistent with what was observed for the 2-D investigations. Furthermore since a finite cylinder with a height to diameter ratio is investigated the results can be compared to CT data although it should be kept in mind that there is no flow through the tower present in this case. Comparing the pressure measurements ranging from  $0.5h$  to  $0.9h$  to the data of Zhao et al. (2012) in Figure 3.17, good agreement between the results is observed.

Important characteristics such as the angle of zero pressure ( $\varphi_0 \sim 36^\circ$ ), angle of minimum pressure ( $\varphi_l \sim 75^\circ$  to  $80^\circ$ ), angle of separation ( $\varphi_N \sim 113^\circ$ ) and wake pressure values ( $C_{pb} \sim -0.4$  to  $-0.5$ ) correspond extremely well for distributions with similar  $C_{p,min}$  values. Thus specifying an equivalent sand grain roughness of  $k_s = 500 \mu\text{m}$ , in this case, is an extremely good representation to account for the effect meridional ribs have on the pressure distribution.



**Figure 4.7:  $C_p$  distribution near the rough solid finite cylinder tip**

It was also found that the rough case results in more stable pressure distributions as the tip is reached as is evident from the clear separation point and wake pressure at  $0.9h$  compared to the smooth cylinder which has a less obvious separation point and slightly increasing wake pressure.

Table 4.1 shows the pressure drag coefficient ( $C_d$ ), determined from the  $C_p$  distribution, as measured along various heights of the cylinder for the smooth and rough cases. Although CFD simulations are known for their under-prediction of drag coefficients (enhanced by the fact that the current simulations are considered steady) the data can still be used in order to investigate the drag trend as measurements are taken at varying heights along the cylinder. From the table it can be seen that the rough case always results in a larger pressure drag around the cylinder as compared to the smooth case. This however is expected since roughening the surface causes earlier flow separation (at trans-critical  $Re$ -numbers) and effectively a larger wake which results in large pressure drag forces acting on the cylinder. It is worth mentioning that the drag due to friction is not considered here since it has been shown in the past that the contribution of skin friction to the drag is extremely small compared to the contribution of pressure drag (Achenbach, 1968).

**Table 4.1: Pressure drag coefficients at various cylinder heights**

Height level	$C_{d, \text{Smooth}}$	$C_{d, \text{Rough}}$
$0h$	0.0044	0.1618
$0.25h$	0.1972	0.2065
$0.50h$	0.2072	0.2553
$0.75h$	0.2021	0.2755
$0.85h$	0.1569	0.2765
$0.95h$	0.1620	0.2751
$1h$	0.2637	0.3120

#### 4.2.2 Flow around an empty hollow finite cylinder with an inlet height

Figure 4.8 shows the velocity contours and vectors through and around a smooth hollow finite cylinder with an inlet height followed by measured pressure distributions at varying heights of the cylinder in Figure 4.9.

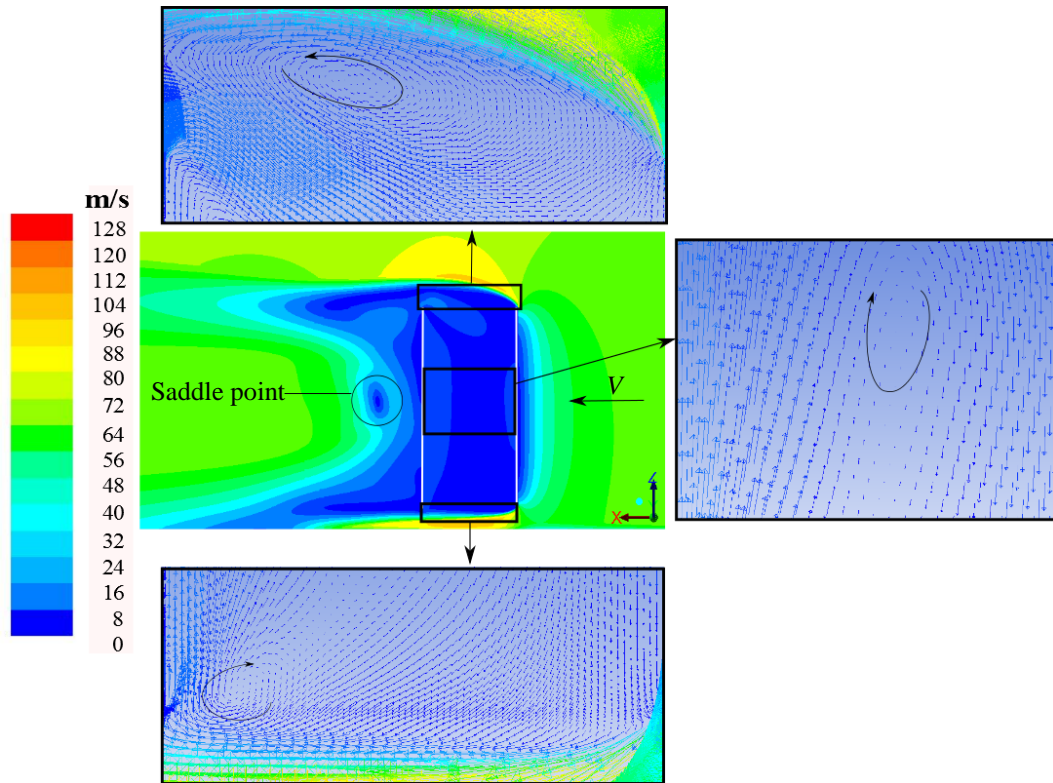
The cylinder height to inlet height ratio chosen for investigation is  $h_{\text{cylinder}}/h_{\text{inlet}} = 8.77$ . This ratio is typically encountered in NDCT designs and is based on an actual NDCT geometry as specified in Kröger (2004).

From the results shown in Figure 4.8 it can be seen that even when there is no solid cylinder top surface a recirculation zone still exists above the cylinder top end due to flow separation on the windward side of the cylinder. Furthermore since a solid surface for re-attachment is now absent the flow tends to circulate into the hollow cylinder effectively creating a downward flow of air through the tower. Specifically the latter flow enters the hollow structure in the middle region of the cylinder top end and moves toward the windward inner wall of the cylinder where it continues to flow downward along the wall. However, at the windward top end of the cylinder air circulates out of the cylinder due to the low pressure zone generated by the accelerated flow at the wall edge.

Now consider the flow at the cylinder bottom end where the inlet is located. It can be seen that as the flow approaches the narrowed inlet section the flow accelerates which effectively creates a low pressure zone at the cylinder inlet. In addition due to this abrupt acceleration of the flow, flow separation occurs on the windward edge of the cylinder. Although most of the accelerated airflow passes through to the leeward side of the cylinder, the airflow closest to the cylinder bottom end collides with the leeward cylinder edge resulting in a recirculation zone as well as upward flowing air along the inner leeward cylinder wall. The combination of the



latter upward flowing air and the downward flowing air from the cylinder top end results in a large recirculation zone in the middle of the hollow cylinder as shown in Figure 4.8 however, the air in this vicinity is for all practical purposes stationary.



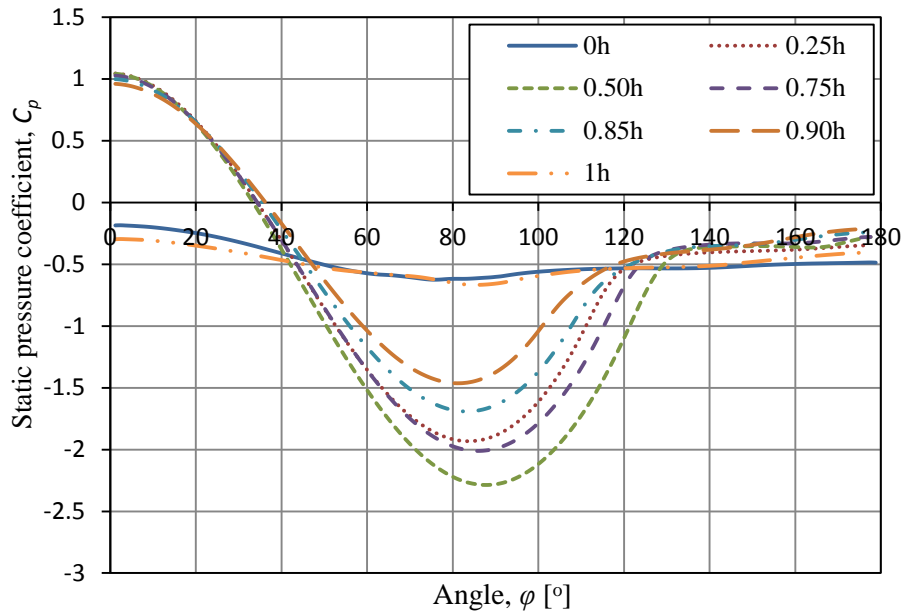
**Figure 4.8: Velocity contours and vectors along the centreline for the smooth hollow finite cylinder**

The static pressure distributions measured along the hollow cylinder height is shown in Figure 4.9. It can be seen that at the cylinder bottom edge ( $0h$ ) a near constant pressure distribution is measured which is almost identical to the pressure distribution at the top end ( $1h$ ) of the cylinder. This can be ascribed to the fact that at both the top and bottom edge of the cylinder flow separation is present which results in accelerated flow at the edges leading to a lower pressure at the edge itself.

However, as pressure distributions further along the cylinder height are considered it can be seen that the expected  $C_p$  trend as described in Figure 1.1 is again observed. Similar to the solid finite cylinder case in the previous section there exists a downward shifting trend for the  $C_p$  curve with increased suction pressures on the cylinder side and delayed separation points. The latter trend is observed once again from the base of the cylinder ( $0h$ ) to the middle of the cylinder height ( $0.50h$ ). However, when considering the  $C_p$  distribution from  $0.50h$  to  $0.90h$  again a trend of relieved suction pressures on the cylinder side and



earlier separation angles are observed and ultimately when approaching the top end of the cylinder again the  $C_p$  trend breaks down.

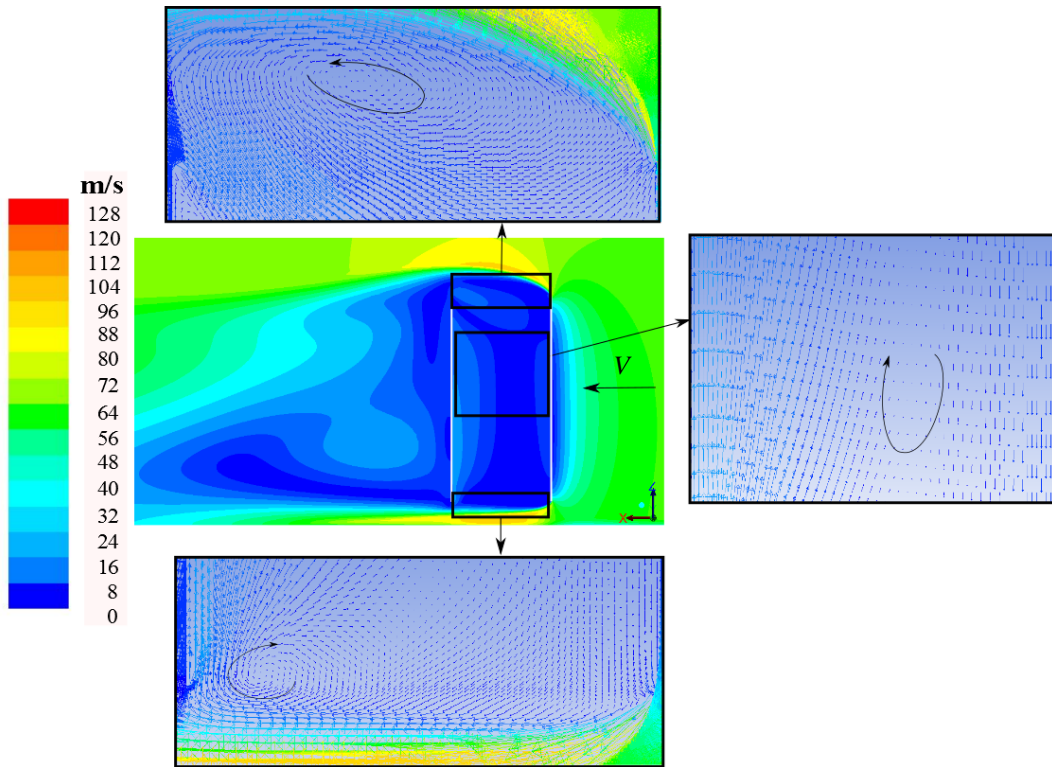


**Figure 4.9:  $C_p$  distribution around the smooth hollow finite cylinder**

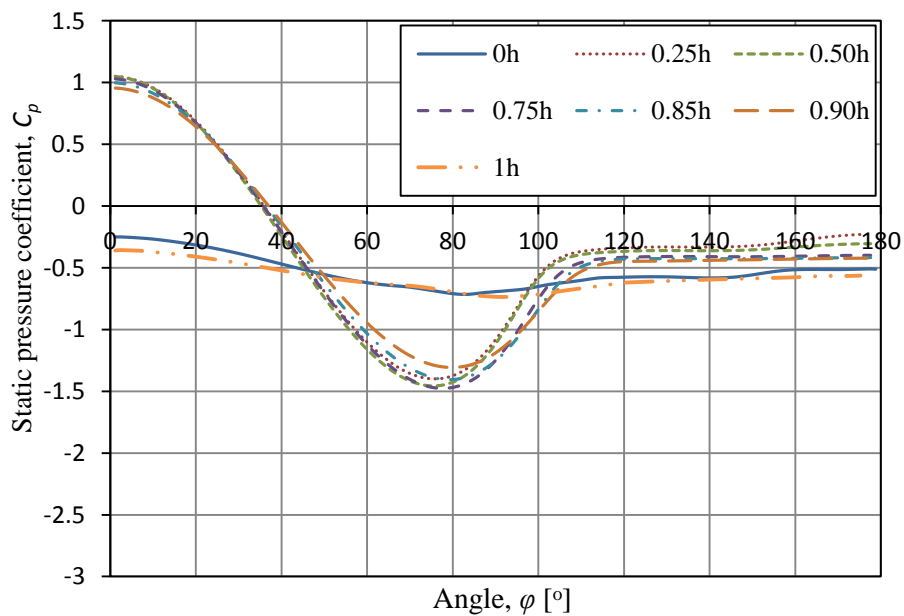
In order to investigate the effect of surface roughening on the flow field through and around the hollow cylinder as well as the effect surface roughening has on the static pressure distribution an equivalent sand grain roughness of  $k_s = 500 \mu\text{m}$  is applied.

Figure 4.10 shows the obtained velocity contours and velocity vectors at important locations of the cylinder. From the results it is observed that roughening of the surface does not significantly affect the general flow at the top end, bottom end and the flow through the cylinder with similar flow patterns encountered when compared to the smooth surface case. However; when looking at the wake region significant changes in the flow behaviour can be observed. Most notably is the disappearance of the saddle point which can be seen in Figure 4.8. In addition considering the leeward cylinder wall it can be seen that in general the velocity is more constant over the height of the cylinder as compared to the smooth case. This can perhaps be seen more clearly when considering the pressure distribution at varying distances along the cylinder height as shown in Figure 4.11.

Once again it is evident from the pressure distributions that a near constant pressure is present at both the top and bottom end of the cylinder. When considering the pressure distributions at  $0h$  and  $1h$  of both the smooth and rough case it can be seen that there is no significant change and both cases reside/tend to around  $C_p = -0.50$ .



**Figure 4.10: Velocity contours and vectors along the centreline for the rough hollow finite cylinder**



**Figure 4.11:  $C_p$  distribution around a rough hollow finite cylinder**

However, when considering the pressure distributions between  $0h$  and  $1h$  a significant change in the  $C_p$  distribution can be noted. It is observed that surface

roughening leads to a more closely spaced pressure distribution along the height of the cylinder with minimal changes between suction pressures and separation angles compared to the smooth surface case. Interesting to note is that the pressure distribution measured between  $0.50h$  and  $0.85h$  can be considered almost exactly similar aside from slight differences in  $C_{p,min}$  values. Although closer to the cylinder top end at  $0.90h$  there is a noticeable relief of minimum pressure however, the separation angle is still similar to the distributions measured at lower heights. The latter implies that surface roughening provides a form of stabilization for the pressure distribution measured along the height of the cylinder.

Since the current model can be regarded as a simple cylindrical cooling tower structure an attempt can be made to compare the generated  $C_p$  distributions with trends found in literature. Specifically when considering the experimentally measured results of Zhao et al. (2012) in Figure 3.17 it can be seen that important angles such as the angle of zero pressure ( $\varphi_0 \sim 36^\circ$ ), angle of minimum pressure ( $\varphi_l \sim 75^\circ$  to  $80^\circ$ ) and angle of separation ( $\varphi_N \sim 112^\circ$ ) correspond extremely well. Furthermore considering the values of important pressure coefficients the minimum pressure ( $C_{p,min} \sim -1.47$ ) and wake pressure ( $C_{pb} \sim -0.4$  to  $-0.5$ ) correspond extremely well.

In short, the current application of  $k_s = 500 \mu\text{m}$  provides a good representation, in terms of the static pressure distribution, of the characteristics of flow around a CT with meridional ribs located on the CT shell surface.

### 4.3 Efficacy of a coarsened mesh

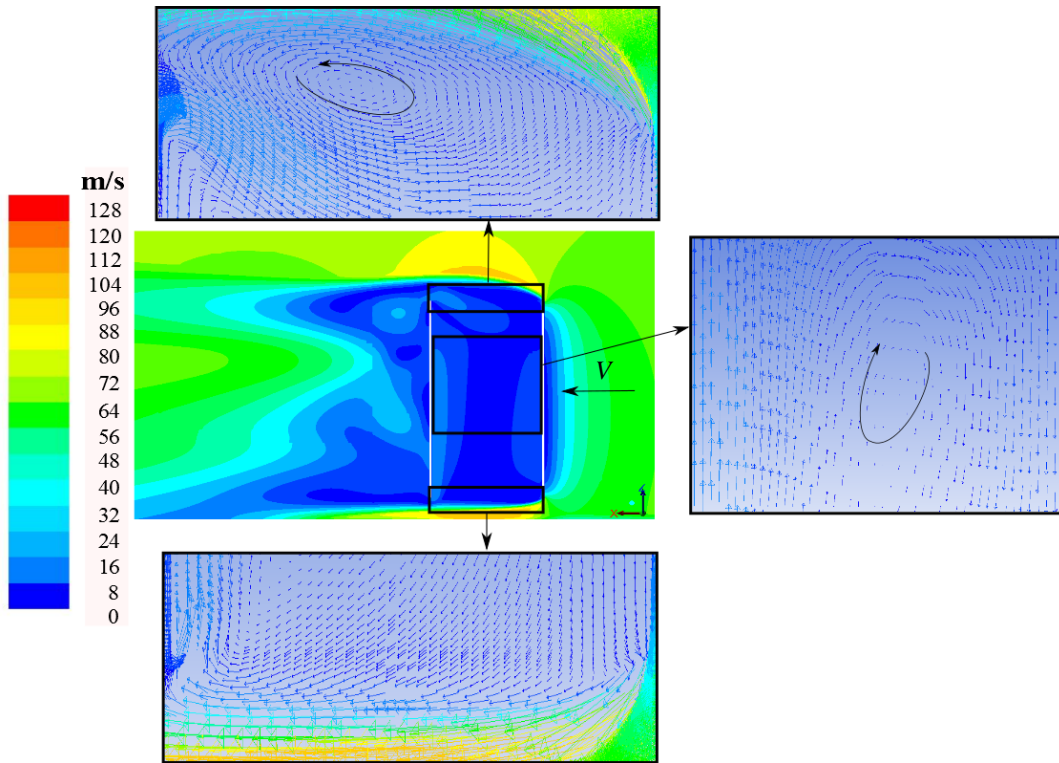
This section investigates how effectively the pressure distribution around the hollow finite cylinder in section 4.2.2 can be predicted if the mesh is coarsened with the aid of the findings in section 3.3.2. The resulting mesh cell count and sizing details are provided in Table E.6 of Appendix E.

Figure 4.12 shows the obtained velocity contours and vectors for the smooth hollow finite cylinder case using the coarsened mesh. When compared to the obtained velocity contours and vectors with the fine mesh in Figure 4.8 it can be seen that the coarse mesh provides an adequate representation of the airflow over the cylinder top end and the subsequent flow through the hollow structure with a recirculation region still visible at the cylinder top end as well as inside the hollow structure. However, the coarsened mesh predicts an entirely different flow in the wake of the cylinder with the disappearance of the saddle point most notable. In addition at the base of the cylinder the small recirculation zone is no longer visible and the airflow mostly moves upward on the leeward inner wall of the cylinder.

In order to get a better idea for the effect mesh coarsening has on the immediate wake region the  $C_p$  distributions at varying heights along the cylinder are considered. The obtained  $C_p$  distributions can be seen in Figure 4.13 followed by a deviation plot in Figure 4.14.

The deviation plot uses the data from the coarse and fine mesh with the deviation value defined as follows:

$$Deviation = \frac{(C_{p,coarse\ mesh} - C_{p,fine\ mesh})}{C_{p,fine\ mesh}} \quad (4.1)$$



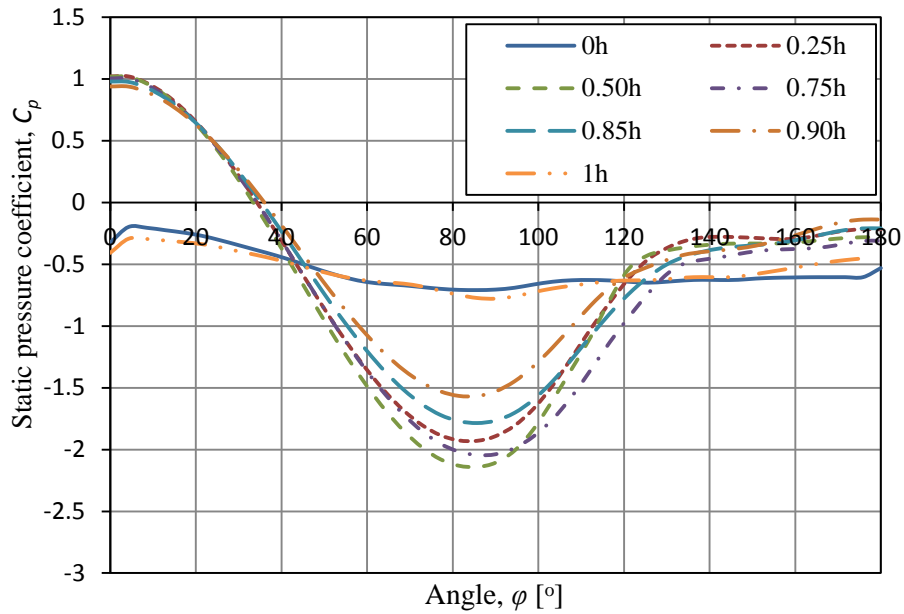
**Figure 4.12: Velocity contours and vectors along the centreline for the coarse smooth hollow finite cylinder**

Similar to the fine mesh case the  $C_p$  distribution along the cylinder height does seem to vary significantly with large differences in  $C_{p,min}$  values observed. Furthermore the pressure distribution at the inlet ( $0h$ ) and outlet ( $1h$ ) of the cylinder is again extremely similar with both varying around  $-0.5$ .

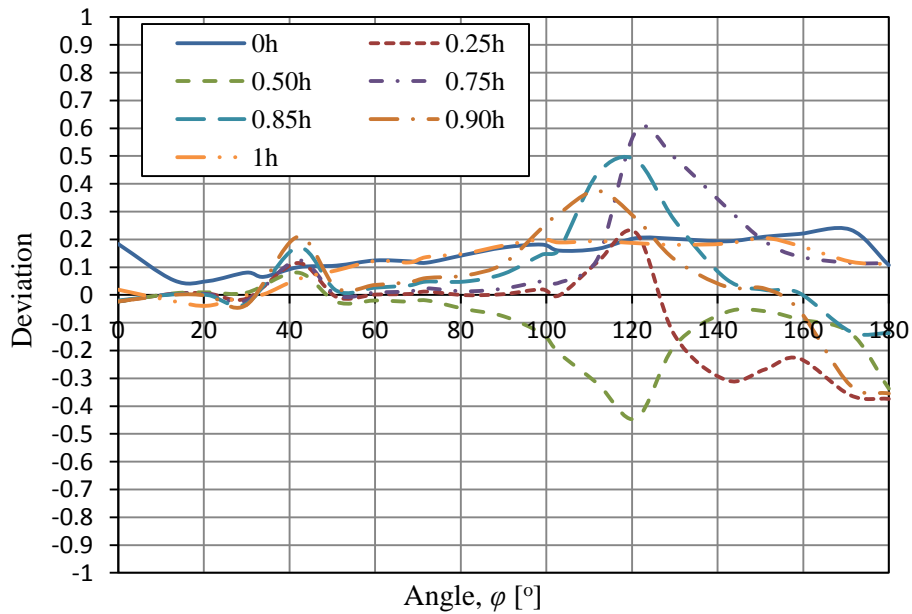
Looking at Figure 4.14 it can be seen that up to the point of zero pressure ( $\varphi_0 \sim 34^\circ$ ) both the coarse and fine mesh predict almost exactly the same pressure distribution however, after the point of zero pressure is passed there is a spike in the deviation plot indicating that the coarse and fine meshes do not correlate extremely well during the acceleration period of the flow up to approximately  $50^\circ$ .

From  $\sim 50^\circ$  toward  $80^\circ$ , which represents the approximate angle at which the minimum pressure is reached, there exist only marginal differences between the coarse and fine mesh predictions with the most notable differences occurring at the cylinder base end, top end and at  $0.5h$ . However; large deviations are observed

during the pressure rise of the  $C_p$  trend and the subsequent separation point and wake region.



**Figure 4.13:**  $C_p$  distribution around a smooth hollow finite cylinder using a coarse mesh

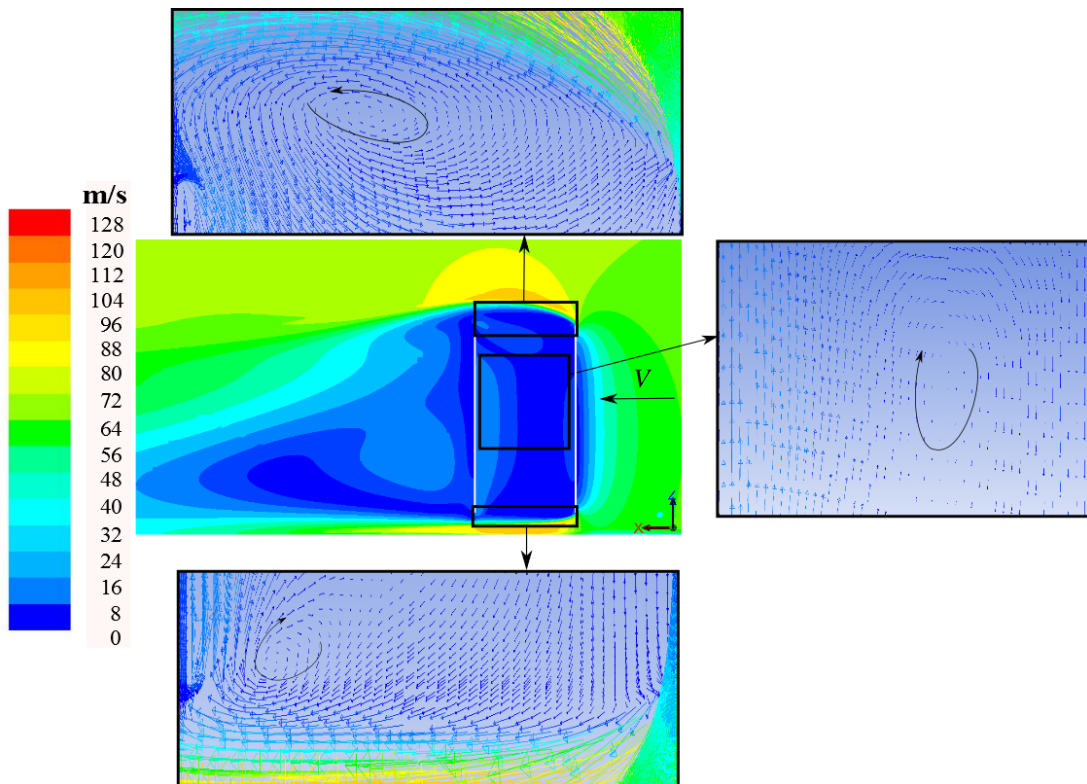


**Figure 4.14:** Deviation plot for the smooth hollow finite cylinder

The latter is however expected since the coarse model predicts a wake with difference characteristics compared to the fine model. The most notable differences when considering the  $C_p$  trend plots and the deviation plot is the larger

variation in wake pressure of the coarse model at varying heights compared to the smaller wake pressure variation of the fine model as well as the mostly delayed pressure distributions predicted by the coarse model. Subsequently it can be concluded that the coarse model for the smooth hollow finite cylinder results in a wake region with significant discrepancies compared to the fine model and lacks the ability to adequately represent the flow phenomena and pressure distributions in the wake.

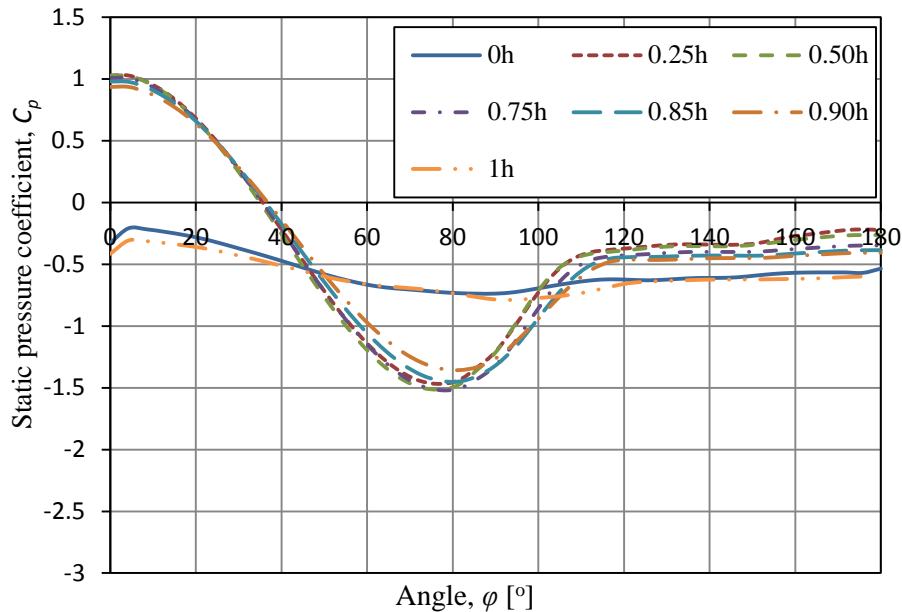
In addition to the smooth hollow finite cylinder an equivalent sand grain roughness of  $k_s = 500 \mu\text{m}$  was also applied to the cylinder surface of the coarse model. As mentioned in section 3.3.3 the use of a surface roughness removes all restrictions in terms of mesh resolution which can be considered an advantage for the use of a coarse mesh. The resulting velocity contours and vectors can be found in Figure 4.15 followed by the obtained  $C_p$  distributions and an error plot for the comparison between the fine and coarse mesh.



**Figure 4.15: Velocity contours and vectors along the centreline for the coarse rough hollow finite cylinder**

Comparing Figure 4.15 to the obtained velocity contours and vectors of the fine mesh in Figure 4.10 it can be seen that both the velocity contours as well as the expected flow phenomena at the specified regions correspond extremely well with no major visible differences. In order to check whether there are significantly large differences between the wake predictions of the coarse and fine model the static pressure distributions were measured at varying heights along the cylinder

wall. The subsequent results are shown in Figure 4.16 followed by a deviation plot in Figure 4.17.

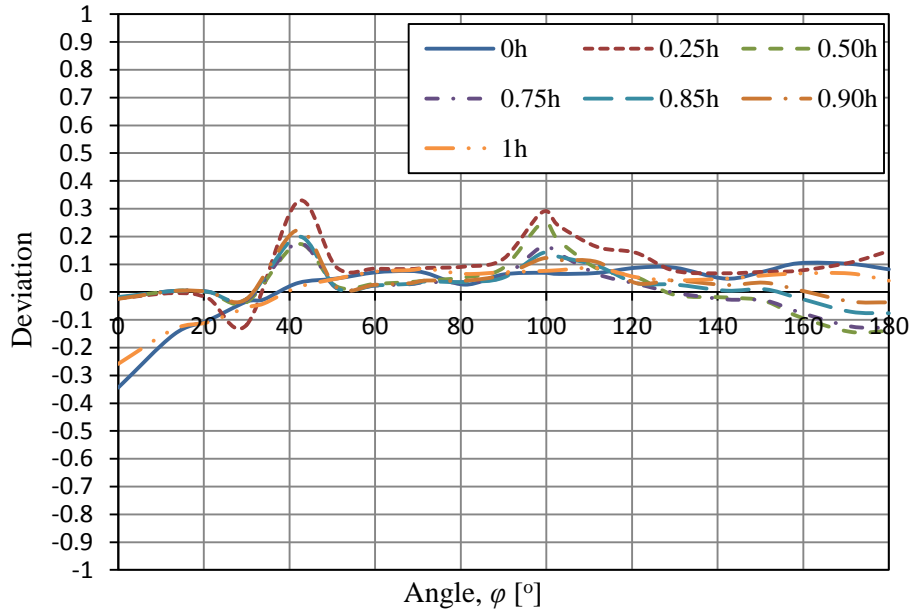


**Figure 4.16:**  $C_p$  distribution around a rough hollow finite cylinder using a coarse mesh

From Figure 4.16 the stabilizing effect surface roughness has on the pressure distribution, as mentioned in section 4.2.2, can clearly be seen with closely spaced pressure distributions observed as measurements are taken along the cylinder height. Furthermore it can also be seen that along the height there is a smaller variation in wake pressure compared to the smooth surface case along with earlier separation angles. However, it is also clear from Figure 4.16 that the measured pressure distributions at the base and top end of the cylinder does vary close to around -0.5 as was observed with the fine mesh solution in Figure 4.11. The latter can also be clearly seen on the deviation plot in Figure 4.17 with relatively small deviations observed, especially in the wake region.

However; when considering the differences for the general  $C_p$  trends along the cylinder height it can be seen that the rough case has significantly smaller deviations when comparing the fine and coarse mesh. In fact aside from error spikes in parts of the acceleration span ( $\sim 35^\circ$  to  $55^\circ$ ) and the pressure recovery stage ( $\sim 90^\circ$  to  $110^\circ$ ) the majority of the predicted pressure distributions compare fairly well with deviations only reaching 10% in most parts. In addition the roughened model also has smaller deviations in the wake region as opposed to the poor performance of the coarse model with a smooth surface where large deviations in wake pressure are observed.





**Figure 4.17: Deviation plot for the rough hollow finite cylinder**

Considering the significant reduction in cell count the rough model can be considered to be an adequate representation for the flow around a roughened cylinder with limited significant deviations between the flow field and pressure distributions along the cylinder height.

#### 4.4 Effect of a non-uniform velocity profile

This section investigates the effect of a power-law velocity profile as opposed to the uniform velocity profile considered up to now. The coarsened model with a specified surface roughness of  $k_s = 500 \mu\text{m}$  in section 4.3 is used for the analysis since it was shown that with a specified surface roughness the changes in the predicted flow field, as compared to the fine mesh, is small with an adequate prediction of the general flow field and  $C_p$  distributions. Furthermore the model also resulted in  $C_p$  distributions which are representative of expected distributions found around NDCTs. Thus it would be of interest to investigate the change in pressure distribution behaviour when a non-uniform velocity profile is considered. The  $1/5^{\text{th}}$  power law profile was applied such that the velocity varies from the ground to the top of the cylindrical structure according to:

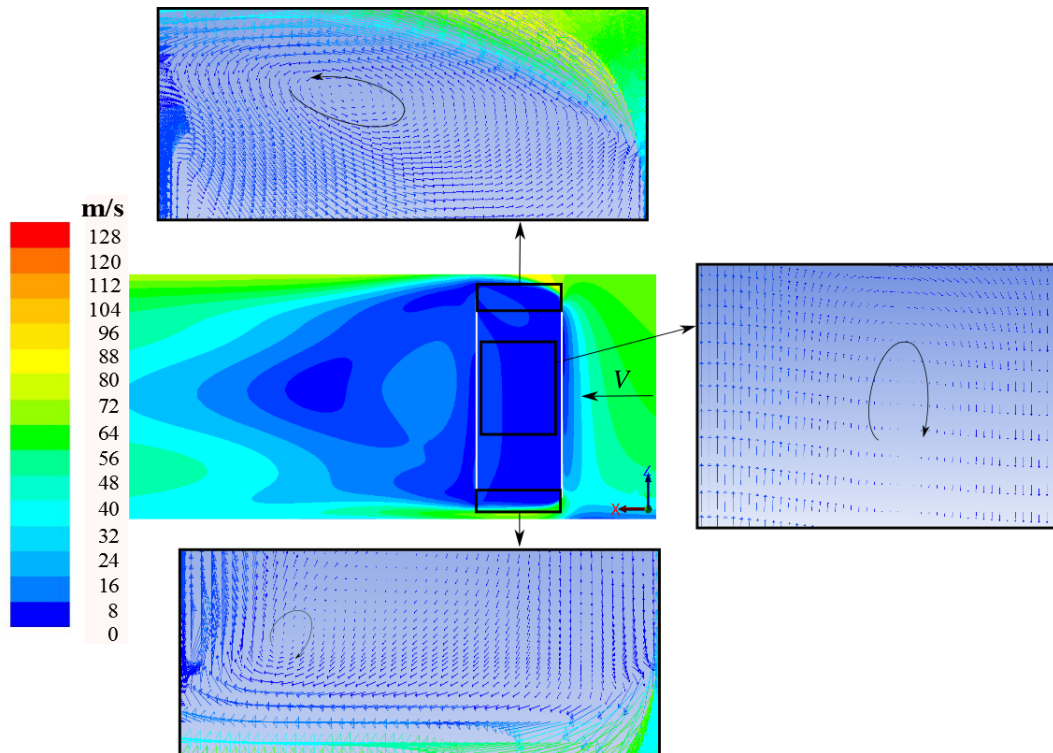
$$V_z = (V_\infty) \left( \frac{z}{z_{ref}} \right)^b \quad (4.2)$$

Where  $z$  is the height above ground level,  $z_{ref}$  is the tower outlet height,  $V_\infty$  is the free stream velocity ( $V_\infty = 71.62 \text{ m/s}$ ) and  $b$  is the exponent used for the power law. The resulting velocity contours and vectors obtained are shown in Figure 4.18. Comparing the resulting flow phenomena at the specified regions to



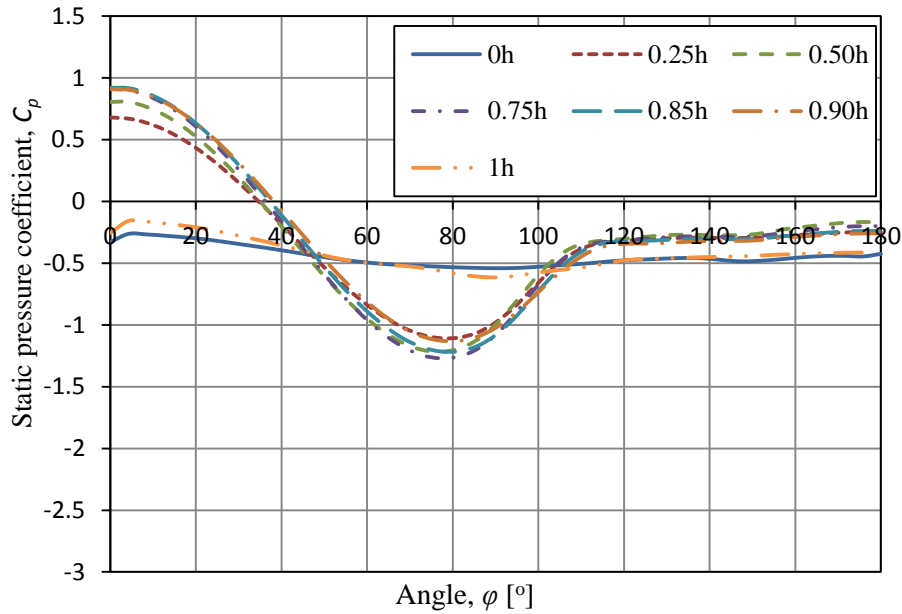
the flow phenomena observed with the uniform velocity profile case in Figure 4.15 it can be seen that in both cases similar structures are observed. However, when considering the wake flow structure it can be seen from the velocity contours that the non-uniform velocity profile results in a wake that differs significantly from that of the uniform profile. This can be seen more clearly when considering the  $C_p$  distribution around the cylindrical structure at varying heights as shown in Figure 4.19.

It is clear that there are differences between the predicted  $C_p$  distributions when compared to the  $C_p$  distribution obtained for the uniform velocity case in Figure 4.16. Most notable is the lower suction pressures present on the side of the cylinder and the significantly lower absolute wake pressures predicted. However, the surface roughness still seems to provide a stabilizing effect with the  $C_p$  distributions measured along the height not varying significantly and the wake pressures predicted along the height resulting in similar values. Furthermore the non-uniform velocity profile also seems to have a visible impact on the predicted angle of zero pressure when compared to the uniform velocity case.

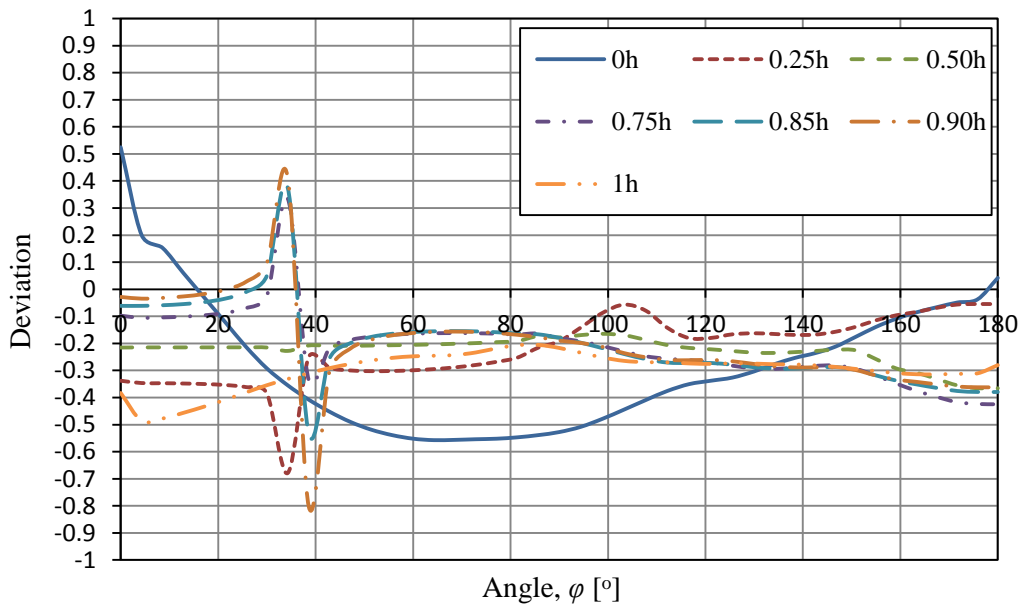


**Figure 4.18: Velocity contours and vectors along the centreline for the coarse rough hollow finite cylinder with a non-uniform velocity profile**

All of the mentioned visible discrepancies between the two cases investigated can be more clearly seen on the deviation plot shown in Figure 4.20.



**Figure 4.19:**  $C_p$  distribution around a rough hollow finite cylinder using a coarse mesh with a non-uniform velocity profile



**Figure 4.20:** Deviation plot for the rough hollow finite cylinder with a non-uniform velocity profile

It is seen that in general there are large changes in important angles and predicted pressure values. However, this large difference is expected since the velocity experienced at the varying heights of the cylinder drastically differs when the profile is imposed. For example consider the large shift in  $C_{p,min}$  values when the profile is imposed. This is expected since the velocity on the windward side of the

cylinder is drastically lower and subsequently the air will have less momentum to accelerate along the cylinder surface resulting in more relieved suction pressures compared to the uniform case. Interesting to note is that the non-uniform velocity profile results in a smaller variation and generally more constant wake pressure along the cylinder height as compared to the uniform case. In conclusion it is observed that the use of a non-uniform velocity profile can significantly affect the pressure distribution around cylindrical structures due to the changes in velocity at different heights along the cylinder surface.

## 4.5 Conclusion

Using Fluent® a 3-D CFD model for the flow around a solid finite cylinder is successfully developed. The developed solid finite cylinder model (Figure 4.2) is found to correlate well with available data from literature and is deemed fit for use in a parametric study in order to investigate the effect surface roughening has on the pressure distribution along the cylinder height as well as the effect it has on the flow field around the cylinder.

It is found that roughening of the cylinder wall surface leads to significant alterations in terms of the flow behaviour around the cylinder. Specifically it can be seen that the roughness element significantly alters the wake region behind the cylinder with an observed shift in the position of the wake vortex and generally more constant velocity in the immediate cylinder wake (Figure 4.5). The latter can be seen more clearly when considering the  $C_p$  distribution along the cylinder height in Figure 4.6. Furthermore it is observed that the roughened model leads to more closely spaced  $C_p$  distributions along the cylinder height compared to the scattered  $C_p$  distributions observed in the smooth case. In addition the roughened case also results in more constant wake pressures which are due to the more constant velocity in the immediate cylinder wake. The above mentioned characteristics of the roughened surface then suggest that roughening has a stabilizing effect on the pressure distribution along the height of the cylinder. Furthermore it is seen in Table 4.1 that in general the roughened cylinder experiences larger pressure drag forces compared to the smooth case. The latter is however expected since roughening the surface leads to earlier flow separation angles subsequently resulting in a larger wake area.

In addition to the solid finite cylinder investigated the latter model is modified to represent a hollow finite cylinder with an inlet height region at the cylinder base. It is found that the addition of the hollow structure with an inlet height leads to significant changes in the flow field around the cylinder. Specifically it is seen that due to the lack of a solid surface at the cylinder top end a portion of the air now circulates into the hollow structure. The latter air then collides with the windward inner wall of the cylinder and starts to move toward the base of the cylinder (Figure 4.8). Furthermore it is seen that a portion of the air at the inlet section collides with the leeward inner wall of the cylinder resulting in a small recirculation zone at the cylinder base and flow travelling upward along the

leeward inner wall surface (Figure 4.8). The combination of the upward travelling air from the base of the cylinder and the downward travelling air from the cylinder top end results in a large recirculation of air in the centre of the cylindrical structure as shown in Figure 4.8.

When surface roughening is applied to the hollow cylinder major changes in the wake area of the cylinder can be observed. Most notable is the disappearance of the saddle point and the generally more constant velocity in the immediate wake of the cylinder (Figure 4.10). Once again it can be seen from the  $C_p$  distribution that the roughened surface results in more closely spaced pressure distributions along the cylinder height (Figure 4.11) as compared to the smooth surface case (Figure 4.9) as well as more constant wake pressures and clear separation angles. Thus again surface roughening seems to have some sort of stabilizing role on the pressure distribution along the cylinder height. Furthermore since the hollow finite cylinder model with an inlet height can be considered as a simple cylindrical CT structure an attempt was made to compare it to available pressure distributions from literature with the results correlating extremely well with data from Zao et al. (2012) who performed experiments on scaled NDCTs.

Lastly the efficacy of using a coarse mesh to represent the flow field and pressure distributions around the hollow finite cylinder is investigated. It is found that the coarse mesh with a smooth surface fails to adequately represent the flow field (Figure 4.12) and pressure distribution (Figure 4.13) when compared to the solution of the fine mesh. Specifically it is observed that the coarse model is unable to reproduce an adequate wake region behind the cylinder resulting in large deviations between the coarse and fine mesh results as shown in Figure 4.14. However, when surface roughening is applied to the coarse mesh the results correlated surprisingly well with the results of the fine mesh as shown in Figure 4.17. In addition a similar stabilizing effect is observed for the roughened case of the coarse model, as compared to the fine model, with more closely spaced  $C_p$  distributions along the height of the cylinder as well as more constant wake pressures as compared to the smooth cases. Furthermore when considering the reduction in cell count it is found that the roughened coarse mesh does indeed provide an adequate representation for the flow and can be used to conduct effective parametric studies for the flow past the cylindrical structure. In addition it is also shown that the use of a non-uniform velocity profile does indeed significantly impact the  $C_p$  distributions at varying heights of the cylinder and has a significant effect on the flow field in the wake region.

## 5 Conclusion and recommendations

This section provides a brief conclusion of all the work covered in the thesis as well as recommendations for possible future work. It should be noted that more detailed conclusions for each chapter can be found in the conclusion section of the applicable chapter and this section only serves as a brief overview of the work as a whole.

### 5.1 Conclusion

In Chapter 3 a 2-D CFD model for flow around an infinite circular cylinder is successfully developed using the Fluent® CFD package. Although some discrepancies were observed between the CFD results and experimentally measured results the majority of important characteristics correlated favourably to a wide range of data from literature and the CFD model was deemed fit for the use in an effective parametric study. The latter parametric study focussed on numerically re-creating the effect meridional ribs has on the pressure distribution around a CT. Specifically researchers in the past have shown that the addition of meridional ribs on the outer shell surface of a CT results in relieved suction pressures on the CT sides as well as larger negative wake pressures and earlier flow separation angles.

The method developed to represent meridional ribs consists of adjusting the momentum in the near wall region through manipulating the wall shear stress in various ways. More specifically three effective methods for momentum adjustment are identified namely: surface roughening using an equivalent sand grain roughness; rotating the cylinder wall and numerically increasing the laminar viscosity in the near wall region. Furthermore it is seen that both the surface roughness technique as well as the laminar viscosity technique resulted in effective manipulation of the pressure distribution around the cylinder with observed relieved suction pressures, earlier flow separation angles and lower negative wake pressures. In addition the resulting  $C_p$  distributions also correlated extremely well with data from literature based on  $C_p$  distributions with similar  $C_{p,min}$  values. Aside from numerically representing the effect of meridional ribs a 2-D CFD model including the physical ribbed structures is also successfully developed. It is found that creating the latter model is extremely time-consuming compared to the model with no ribs and leads to an increase in cell count due to the added resolution necessary in the near wall region. However, the model proved to be an effective method for representing the effect of meridional ribs and compared extremely favourable with the numerical techniques developed for the momentum adjustment as well as experimental results.

Furthermore through shear stress curve comparisons all models can be effectively calibrated such that for a specific set of parameters ( $k_s$ ,  $\mu_{lam}$  and  $k/a$ ) every individual variable generates the same  $C_p$  trend.

In addition to the investigation of effectively re-creating the effect of meridional ribs the sensitivity of the pressure distribution to mesh sizing is also investigated. It is found that the results are fairly sensitive to sizing changes in the radial direction with significant shifts in the minimum pressure as well as separation point observed. However, when considering the sensitivity to the cylinder wall sizing the results do not show a large sensitivity to significant increases in cell size with marginal changes observed in the  $C_p$  trend. Lastly it is also shown that for the current model the wake can be significantly coarsened with no visible alterations to the predicted  $C_p$  trend.

Furthermore at the end of Chapter 3 it is shown that although the CFD model cannot effectively predict the  $C_p$  distribution around a cylinder when compared to the measured experimental data it can however be calibrated with the developed momentum adjustment techniques to such a state that it can be deemed as an adequate representation for the flow.

In Chapter 4 the developed 2-D model is expanded to a 3-D model such that the flow around finite cylinders can be studied. For the smooth solid finite cylinder case it is found that the  $C_p$  distribution varies significantly as measurements are taken along the height of the cylinder. Furthermore when roughening is applied to the cylinder surface the flow behaviour in the wake is significantly affected with more constant/stable wake pressures observed. In addition it is observed that roughening also leads to  $C_p$  distribution stabilization along the cylinder height. Furthermore in addition to the smooth solid finite model a hollow cylinder with an inlet height is also investigated. It is found that the addition of surface roughening leads to significant changes in the wake region of the cylinder and provides stability to the  $C_p$  distributions along the cylinder as well as the cylinder wake pressure itself.

Lastly in Chapter 4 the efficacy of using a coarsened mesh is investigated. It is found that for the smooth surface case the coarsened model fails to accurately reproduce the flow conditions in the wake region when compared to the fine mesh solution. However, when surface roughening is applied the coarsened model compares extremely well with the fine model solution. In fact the comparison is so favourable that the coarsened model can be deemed fit for the adequate representation of the flow through and around the hollow cylindrical structure. The coarse model is also used to determine the effect a non-uniform wind profile and it is found that the latter does significantly affect the  $C_p$  distributions as measured along the cylinder height as well as the wake region.

## 5.2 Recommendations

Although the present research provided useful insight i.t.o the effect the investigated parameters have on the pressure distribution and general flow field around a cylinder as well as resulted in a viable method(s) for modelling meridional ribs the scope of the research can be further extended to:

- Include a full scale cooling tower model with the addition of thermal and plume effects, i.e. including heat exchanger bundles with heat transfer characteristics to induce a draft through the tower
- Perform a sensitivity analysis which includes the effect of using a velocity profile, as opposed to the use of a uniform velocity profile, and varying wind velocities such that the effect the latter has on the thermal performance and outlet plume can be effectively investigated
- Investigate possible methods of reducing the negative effect wind has on the measured pressure distribution around the tower through including additional elements such as varying the CT inlet and outlet geometries and adding wind shield-type structures to the outlet and inlet of the tower

In addition, to further confirm the validity of the shear stress calibration method developed in section 3.5, experimental tests consisting of measuring the shear stress distributions, or alternatively the drag force, on a flat plate should be conducted.

Furthermore wind tunnel experiments on finite cylinders with an inlet height and added surface roughness (consisting of both sand paper and ribbed structures) should be conducted to gain additional understanding of how the pressure distribution reacts for the case of a cylinder with a specified height to diameter ratio. The latter model can then also be extended to include a draft through the tower such that the plume effect can be studied experimentally. In addition to measuring the pressure distribution along the cylinder periphery PIV can also be utilized to investigate the flow patterns applicable to smooth and rough finite cylinders under the influence of a cross-wind.



## 6 References

- Achenbach, E., 1968. Distribution of local pressure and skin friction around a circular cylinder in cross-flow up to  $Re = 5 \times 10^6$ . *Journal of Fluid Mechanics*, Volume 34, pp. 625-639.
- Achenbach, E., 1970. Influence of surface roughness on the cross-flow around a circular cylinder. *Journal of Fluid Mechanics*, Volume 46, pp. 321-335.
- Al-Waked, R. & Behnia, M., 2004. The performance of natural draft dry cooling towers under crosswind: CFD study. *International Journal of Energy Research*, Volume 28, pp. 147-161.
- Al-Waked, R. & Behnia, M., 2006. CFD simulation of wet cooling towers. *Applied Thermal Engineering*, Volume 26, p. 382-395.
- Buresti, G., 1981. The effect of surface roughness on the flow regime around circular cylinders. *Journal of Wind Engineering and Industrial Aerodynamics*, Volume 8, pp. 105-114.
- Catalano, P., Wang, M., Iaccarino, G. & Moin, P., 2003. Numerical simulation of the flow around a circular cylinder at high Reynolds numbers. *International Journal of Heat and Fluid Flow*, Volume 24, pp. 463-469.
- Cengel, Y. & Cimbala, J., 2010. *Fluid Mechanics: Fundamentals and Applications*. 2 ed. New York: McGraw-Hill.
- du Buisson, J., 1988. *The effectiveness of commercially available components used to decrease the aerodynamic drag force on heavy motor vehicles*, Stellenbosch: University of Stellenbosch.
- du Preez, A. F., 1992. *The Influence of Cross-winds on the Performance of Natural Draft Dry-Cooling Towers*, Stellenbosch: Stellenbosch University.
- du Preez, A. & Kröger, D., 1995. The effect of the heat exchanger arrangement and wind-break walls on the performance of natural draft dry-cooling towers subjected to cross-winds. *Journal of Wind Engineering*, Volume 58, pp. 293-303.
- Farrel, C. & Arroyave, J., 1990. On uniform flow around rough circular cylinders at Critical Reynolds numbers. *Journal of Wind Engineering and Industrial Aerodynamics*, Volume 36, pp. 621-631.
- Fluent, A., 2013. *Fluent User Manual version 14.5.7*. s.l.:s.n.
- Goudarzi, M.-A. & Sabbagh-Yazdi, S.-R., 2008. Modeling wind ribs effects for numerical simulation external pressure load on a cooling tower of KAZERUN power plant-IRAN. *Wind and Structures*, Volume 11, pp. 479-496.



Gould, R., Raymer, W. & Ponsford, P., 1968. Wind tunnel tests on chimneys of circular section at High Reynolds numbers. *Proceeding of the Symposium on wind effects on buildings and structures, Loughborough.*

Guven, O., Farell, C. & Patel, V., 1980. Surface-roughness effects on the mean flow past circular cylinders. *Journal of Fluid Mechanics*, Volume 98, pp. 673-701.

Hill, R. J., 2014. *Experimental investigation of the flow patterns around an infinite cylinder in a wind tunnel.* Stellenbosch: University of Stellenbosch.

Jones, G., Cincotta, J. & Walker, R., 1969. *Aerodynamic forces on a stationary and oscillating circular cylinder at high Reynolds numbers.* Washington, D.C: NASA.

Krajnovic, S., 2011. Flow around a tall finite cylinder explored by large eddy simulation. *Journal of Fluid Mechanics*, Volume 676, pp. 294-317.

Kröger, D., 2004. *Air-cooled Heat Exchangers and Cooling Towers.* s.l.:s.n.

Lupi, F., 2013. *Stochastic aerodynamic effects in the design of ultra-high towers exposed to the atmospheric flow.* s.l.:University of Florence and University of Braunschweig.

Lu, Y., Guan, Z., Gurgenci, H. & Zou, Z., 2013. Windbreak walls reverse the negative effect of crosswind in short natural draft dry cooling towers into a performance enhancement. *International Journal of Heat and Mass Transfer*, Volume 63, p. 162–170.

Majumdar, S. & Rodi, W., 1989. Three-Dimensional Computation of Flow Past Cylindrical Structures and Model Cooling Towers. *Building an Environment*, Volume 24, pp. 3-22.

Nakamura, Y. & Tomonari, Y., 1982. The effects of surface roughness on the flow past circular cylinders at high Re numbers. *Journal of Fluid Mechanics*, Volume 123, pp. 363-378.

Niemann, H.-J., 1971. *Zur stationären Windbelastung rotationssymmetrischer Bauwerke im Bereich transkritischer Reynoldszahlen.* s.l.:s.n.

Niemann, H.-J. & Hölscher, N., 1990. A Review of Recent Experiments on the Flow past Circular Cylinders. *Journal of Wind Engineering and Industrial Aerodynamics*, Volume 33, pp. 197-209.

Niemann, H.-J. & Hölscher, N., 1990. A Review of Recent Experiments on the Flow past Circular Cylinders. *Journal of Wind Engineering and Industrial Aerodynamics*, Volume 33, pp. 197-209.

Pröper, H., 1977. *Zur aerodynamischen Belastung grosser Kühltürme.* s.l.:s.n.

- Reuter, H. C., 2010. *Performance Evaluation of Natural Draught Cooling Towers with Anisotropic Fills*, Stellenbosch: Stellenbosch University.
- Ribeiro, J., 1991. Effects of surface roughness on the 2-D flow past circular cylinders I: mean forces and pressure. *Journal of Wind Engineering and Industrial Aerodynamics*, Volume 37, pp. 299-309.
- Ribeiro, J., 1991. Effects of surface roughness on the two-dimensional flow past circular cylinders I: mean forces and pressures. *Journal of Wind Engineering and Industrial Aerodynamics*, Volume 37, pp. 299-309.
- Roshko, A., 1960. Experiments on the flow past a circular cylinder at very high Reynolds number.
- Rostamy, N., Sumner, D., Bergstrom, D. & Bugg, J., 2012. Local flow field of a surface-mounted finite circular cylinder. *Journal of Fluids and Structures*, pp. 105-122.
- Schlichting, H., 1979. *Boundary Layer Theory*. 7 ed. s.l.:McGraw Hill.
- Störm, H. C., 2010. *CFD investigation of flow in and around a natural draft cooling tower*. s.l.:University of Stellenbosch.
- Sumner, D., 2013. Flow aboe the free end of a surface-mounted finite-height circular cyliinder: A Review. *Journal of Fluids and Structures*, Volume 43, pp. 41-63.
- Su, M., Tang, G. & Fu, S., 1999. Numerical simulation of fluid flow and thermal performance of a dry-cooling tower under cross wind condition. *Journal of Wind Engineering and Industrial Aerodynamics*, Volume 79, pp. 289-306.
- Uematsu, Y. & Yamada, M., 1994. Aerodynamic forces on circular cylinders of finite height. *Journal of Wind Engineering and Industrial Aerodynamics*, Volume 51, pp. 249-265.
- Versteeg, H. & Malalasekera, W., 2007. *An Introduction to Computational Fluid Dynamics: The Finite Volume Method*. 2nd ed. Harlow: Pearson Education Limited.
- Viollet, P., 1977. *Etude de jest dans des courants transversiers et dans des milieux stratifies..* Paris: Universite Pierre et Marie Curie.
- Wei, Q.-d.et al., 1995. A study of the unfavourable effects of wind on the cooling efficiency of dry cooling towers. *Journal of Wind Engineering and Industrial Aerodynamics*, Volume 54/55, pp. 633-643.
- Yang, L., Chen, L., Du, X. & Yang, Y., 2013. Effects of ambient winds on the thermo-flow performances of indirect dry cooling system in a power plant. *International Journal of Thermal Sciences*, Volume 64, pp. 178-187.

Zhao, L., Cheng, X.-X., Dong, R. & Ge, Y.-J., 2012. Investigation of Surface Roughness and its Influence to Flow Dynamic Characteristics of Hyperbolic Cooling Tower. *6th International Symposium on Cooling Towers*.

## Appendix A: UDF for the wall viscosity technique

```
#include "udf.h"

#define WALL_ID 10

DEFINE_PROPERTY(viscosity,c,t)
{
    face_t f;
    Thread *tf;
    int n;
    real mu_lam;
    real factor = 23;
    mu_lam = 1.846e-05;

    /* Loop over all the faces of the current cell and check if one of the faces
    belong to WALL_ID */
    c_face_loop(c, t, n)
    {
        tf = C_FACE_THREAD(c,t,n);
        if (THREAD_ID(tf) == WALL_ID ) mu_lam = factor*1.846e-05;
    }

    return mu_lam;
}
```

## Appendix B: 2-D CFD pressure distribution data

This appendix contains select raw static pressure distribution data as obtained from the various numerical models. All distance positions are as measured from the windward cylinder stagnation point.

**Table B.1: Smooth cylinder data**

<b>x-Position [m]</b>	<b>Static Pressure [Pa]</b>	<b>x-Position [m]</b>	<b>Static Pressure [Pa]</b>
-0.2286	12735.3	-0.182087	-4266.99
-0.22855	12713.3	-0.179152	-5192.33
-0.228399	12656	-0.176139	-6124.64
-0.228149	12557.7	-0.173049	-7062.71
-0.227798	12417.8	-0.169883	-8002.94
-0.227348	12236.9	-0.166642	-8943.13
-0.226797	12015.2	-1.63E-01	-9882.46
-0.226148	11753.2	-0.159943	-10819.2
-0.225399	11451.3	-0.156487	-11750.5
-0.224551	11109.9	-0.152963	-12674.5
-0.223605	10729.8	-0.149372	-13589.5
-0.22256	10312.2	-0.145715	-14493.7
-0.221418	9856.61	-0.141994	-15385.1
-0.220179	9364.05	-0.138211	-16261.7
-0.218843	8836.76	-0.134368	-17121.8
-0.217412	8275.36	-0.130465	-17963.6
-0.215884	7680.9	-0.126505	-18785
-0.214263	7054.44	-0.12249	-19583.7
-0.212547	6397.21	-0.118421	-20359.5
-0.210738	5710.77	-0.1143	-21111
-0.208836	4996.47	-0.110129	-21834.5
-0.206843	4255.79	-0.105909	-22528.6
-0.20476	3490.37	-0.101644	-23192
-0.202586	2701.19	-0.0973331	-23823.1
-0.200324	1889.41	-0.09298	-24420.1
-0.197973	1057.2	-0.0885861	-24981.4
-0.195536	206.472	-0.0841533	-25505.5
-0.193013	-661.273	-0.0796836	-25990.5
-0.190406	-1544.33	-0.0751789	-26437
-0.187715	-2440.87	-0.0706413	-26843.9
-0.184941	-3349.06	-0.0660727	-27207.5

<b>x-Position [m]</b>	<b>Static Pressure [Pa]</b>	<b>x-Position [m]</b>	<b>Static Pressure [Pa]</b>
-0.0614751	-27526.8	0.108149	-5105.24
-0.0568505	-27800.7	0.112261	-4743.45
-0.052201	-28028	0.116326	-4515.83
-0.0475286	-28209.2	0.120342	-4373.51
-0.0428354	-28342.6	0.124308	-4283.88
-0.0381233	-28425.7	0.12822	-4226.38
-0.0333946	-28458.7	0.132079	-4188.72
-0.0286512	-28440.4	0.135882	-4163.78
-0.0238952	-28372	0.139628	-4145.42
-0.0191288	-28251.6	0.143315	-4130.84
-0.0143539	-28075.4	0.146941	-4119.51
-0.00957277	-27844.4	0.150548	-4109.24
-0.00478744	-27558.2	0.154089	-4099.69
1.39977E-17	-27218.2	0.157564	-4090.98
0.00469358	-26827.6	0.160971	-4083.13
0.00938518	-26384	0.164309	-4076.23
0.0140728	-25884	0.167576	-4070.34
0.0187545	-25327.9	0.17077	-4065.42
0.0234283	-24715	0.17389	-4061.44
0.0280923	-24044.3	0.176936	-4058.31
0.0327443	-23315	0.179905	-4055.9
0.0373826	-22525.6	0.182797	-4054.06
0.0420051	-21675.7	0.185609	-4052.58
0.0466099	-20764	0.188341	-4051.28
0.0511951	-19788.2	0.190993	-4049.95
0.0557587	-18747.1	0.193561	-4048.38
0.0602987	-17638.9	0.196046	-4046.33
0.0648134	-16462.8	0.198447	-4043.56
0.0693007	-15219.4	0.200761	-4039.81
0.0737588	-13912.4	0.20299	-4034.86
0.0781858	-12552.9	0.20513	-4028.52
0.0825798	-11162.6	0.207182	-4020.8
0.0869391	-9783.54	0.209144	-4011.74
0.0912616	-8484.63	0.211017	-4000.42
0.0955457	-7341.63	0.212798	-3987.53
0.0997895	-6395.89	0.214487	-3974.28
0.103991	-5650.45	0.216084	-3960.02

x-Position [m]	Static Pressure [Pa]
0.217587	-3944.7
0.218996	-3928.77
0.220311	-3912.56
0.221531	-3896.27
0.222655	-3880.18
0.223683	-3864.48
0.224615	-3849.41
0.225449	-3835.24
0.226186	-3822.24
0.226826	-3810.66
0.227367	-3800.76
0.227811	-3792.81
0.228156	-3786.97
0.228403	-3783.5
0.228551	-3784.98
0.2286	-3788.36

Table B.2: Rough cylinder data;  $k_s = 500\mu\text{m}$ 

x-Position [m]	Static Pressure [Pa]	x-Position [m]	Static Pressure [Pa]
-0.2286	13169	-0.212547	7272.18
-0.22855	13146.3	-0.210738	6641.59
-0.228399	13089.4	-0.208836	5985.86
-0.228149	12994.1	-0.206843	5306.99
-0.227798	12861	-0.20476	4606.36
-0.227348	12690.2	-0.202586	3885.41
-0.226797	12481.1	-0.200324	3146.12
-0.226148	12233.9	-0.197973	2390.66
-0.225399	11950.3	-0.195536	1619.77
-0.224551	11630.9	-0.193013	834.096
-0.223605	11276.4	-0.190406	36.1789
-0.22256	10887.6	-0.187715	-771.506
-0.221418	10464.7	-0.184941	-1587.14
-0.220179	10008.4	-0.182087	-2409.04
-0.218843	9520.29	-0.179152	-3235.17
-0.217412	9001.31	-0.176139	-4063.87
-0.215884	8452.57	-0.173049	-4894.02
-0.214263	7875.94	-0.169883	-5723.13

<b>x-Position [m]</b>	<b>Static Pressure [Pa]</b>	<b>x-Position [m]</b>	<b>Static Pressure [Pa]</b>
-0.169883	-5723.13	-0.00957277	-16985.5
-0.166642	-6548.47	-0.00478744	-16281.4
-0.163328	-7368.64	1.39977E-17	-15518.7
-0.159943	-8181.45	0.00469358	-14710.1
-0.156487	-8985.44	0.00938518	-13861.6
-0.152963	-9778.8	0.0140728	-12982.9
-0.149372	-10558.4	0.0187545	-12093.2
-0.145715	-11322.3	0.0234283	-11213.6
-0.141994	-12068.8	0.0280923	-10371.4
-0.138211	-12795.8	0.0327443	-9589.75
-0.134368	-13501.3	0.0373826	-8887.52
-0.130465	-14183	0.0420051	-8281.91
-0.126505	-14840.9	0.0466099	-7777.27
-0.12249	-15473.1	0.0511951	-7369.64
-0.118421	-16074.8	0.0557587	-7048.86
-0.1143	-16644.5	0.0602987	-6800.56
-0.110129	-17180.8	0.0648134	-6609.47
-0.105909	-17681.6	0.0693007	-6461.98
-0.101644	-18145.6	0.0737588	-6347.57
-0.0973331	-18573.4	0.0781858	-6259.1
-0.09298	-18962	0.0825798	-6190.88
-0.0885861	-19306.5	0.0869391	-6138.13
-0.0841533	-19605.9	0.0912616	-6097.04
-0.0796836	-19858.2	0.0955457	-6065.5
-0.0751789	-20064.5	0.0997895	-6041.39
-0.0706413	-20223.8	0.103991	-6020.77
-0.0660727	-20330.7	0.108149	-6003.3
-0.0614751	-20383.1	0.112261	-5989.06
-0.0568505	-20381.4	0.116326	-5976.16
-0.052201	-20324.8	0.120342	-5964.3
-0.0475286	-20209.4	0.124308	-5953.42
-0.0428354	-20034.1	0.12822	-5943.52
-0.0381233	-19797.1	0.132079	-5934.59
-0.0333946	-19495.6	0.135882	-5926.59
-0.0286512	-19128	0.139628	-5919.51
-0.0238952	-18693.7	0.143315	-5913.3
-0.0191288	-18192.2	0.146941	-5907.88
-0.0143539	-17622.7	0.150548	-5903.18



<b>x-Position [m]</b>	<b>Static Pressure [Pa]</b>	<b>x-Position [m]</b>	<b>Static Pressure [Pa]</b>
0.154089	-5899.12	0.228403	-5601.73
0.157564	-5895.6	0.228551	-5602.94
0.160971	-5892.51	0.2286	-5605.29
0.167576	-5887.04		
0.17077	-5884.42		
0.17389	-5881.69		
0.176936	-5878.72		
0.179905	-5875.38		
0.182797	-5871.53		
0.185609	-5867.05		
0.188341	-5861.82		
0.190993	-5855.75		
0.193561	-5848.78		
0.196046	-5840.91		
0.198447	-5832.2		
0.200761	-5822.53		
0.20299	-5811.85		
0.20513	-5800.67		
0.207182	-5789.08		
0.209144	-5776.88		
0.211017	-5764.28		
0.212798	-5751.43		
0.214487	-5738.46		
0.216084	-5725.43		
0.217587	-5712.47		
0.218996	-5699.69		
0.220311	-5687.19		
0.221531	-5675.11		
0.222655	-5663.56		
0.223683	-5652.61		
0.224615	-5642.44		
0.225449	-5633.15		
0.226186	-5624.81		
0.226826	-5617.57		
0.227367	-5611.54		
0.227811	-5606.85		
0.228156	-5603.6		

**Table B.3: Rough cylinder data; angular velocity of 275 rad/sec**

x-Position [m]	Static Pressure [Pa]	x-Position [m]	Static Pressure [Pa]
-0.2286	13602.3	-0.159943	-7507.5
-0.22855	13232.3	-0.156487	-8278.21
-0.228399	13180.2	-0.152963	-9036.11
-0.228149	13115.6	-0.149372	-9779.39
-0.227798	12982.8	-0.145715	-10506.1
-0.227348	12814.9	-0.141994	-11214
-0.226797	12614.7	-0.138211	-11901.2
-0.226148	12375.7	-0.134368	-12565.5
-0.225399	12100.2	-0.130465	-13204.7
-0.224551	11789.1	-0.126505	-13817.5
-0.223605	11443.2	-0.12249	-14402.2
-0.22256	11062.9	-0.118421	-14955.9
-0.221418	10648.9	-0.1143	-15476.7
-0.220179	10202.1	-0.110129	-15962.6
-0.218843	9723.87	-0.105909	-16411.5
-0.217412	9215.23	-0.101644	-16821.6
-0.215884	8677.33	-0.0973331	-17191.9
-0.214263	8111.39	-0.09298	-17520.3
-0.212547	7518.67	-0.0885861	-17803.9
-0.210738	6900.52	-0.0841533	-18040.5
-0.208836	6258.36	-0.0796836	-18228.8
-0.206843	5593.73	-0.0751789	-18367.7
-0.20476	4908.02	-0.0706413	-18453.9
-0.202586	4202.84	-0.0660727	-18485.5
-0.200324	3480.03	-0.0614751	-18460.9
-0.197973	2741.39	-0.0568505	-18377.7
-0.195536	1988.33	-0.052201	-18234
-0.193013	1222.2	-0.0475286	-18027.8
-0.190406	445.024	-0.0428354	-17755.4
-0.187715	-341.218	-0.0381233	-17412.9
-0.184941	-1134.7	-0.0333946	-16999
-0.182087	-1933.44	-0.0286512	-16510.8
-0.179152	-2735.19	-0.0238952	-15945.5
-0.176139	-3538.06	-0.0191288	-15301.3
-0.173049	-4340.69	-0.0143539	-14578.6
-0.169883	-5140.82	-0.00957277	-13781.2
-0.166642	-5936.34	-0.00478744	-12919.7
-0.163328	-6725.98	1.39977E-17	-12022

<b>x-Position [m]</b>	<b>Static Pressure [Pa]</b>	<b>x-Position [m]</b>	<b>Static Pressure [Pa]</b>
1.39977E-17	-12022	0.160971	-6224.04
0.00469358	-11130.5	0.164309	-6223.18
0.00938518	-10278	0.167576	-6222.11
0.0140728	-9478.75	0.17077	-6220.71
0.0187545	-8742.26	0.17389	-6218.83
0.0234283	-8089.9	0.176936	-6216.34
0.0280923	-7549.8	0.179905	-6213.11
0.0327443	-7131.1	0.182797	-6209.03
0.0373826	-6820.45	0.185609	-6204
0.0420051	-6596.66	0.188341	-6197.94
0.0466099	-6441.56	0.190993	-6190.79
0.0511951	-6343.59	0.193561	-6182.52
0.0557587	-6293.46	0.196046	-6173.14
0.0602987	-6278.3	0.198447	-6162.66
0.0648134	-6282.01	0.200761	-6151.15
0.0693007	-6291.02	0.20299	-6138.69
0.0737588	-6298.54	0.20513	-6125.4
0.0781858	-6302.3	0.207182	-6111.38
0.0825798	-6301.58	0.209144	-6096.8
0.0869391	-6297.52	0.211017	-6081.8
0.0912616	-6291.96	0.212798	-6066.55
0.0955457	-6285.86	0.214487	-6051.18
0.0997895	-6279.53	0.216084	-6035.85
0.103991	-6273.17	0.217587	-6020.7
0.108149	-6266.95	0.218996	-6005.87
0.112261	-6260.99	0.220311	-5991.49
0.116326	-6255.37	0.221531	-5977.7
0.120342	-6250.16	0.222655	-5964.62
0.124308	-6245.42	0.223683	-5952.36
0.12822	-6241.2	0.224615	-5941.08
0.132079	-6237.51	0.225449	-5930.91
0.135882	-6234.38	0.226186	-5921.95
0.139628	-6231.77	0.226826	-5914.47
0.143315	-6229.68	0.227367	-5908.85
0.146941	-6228.03	0.227811	-5905.19
0.150548	-6226.69	0.228156	-5905.18
0.154089	-6225.67	0.228403	-5901.63
0.157564	-6224.83	0.228551	-5924.66

**Table B.4: Rough cylinder data;  $\mu = 72\mu_{lam}$** 

x-Position [m]	Static Pressure [Pa]	x-Position [m]	Static Pressure [Pa]
-0.2286	13207.3	-0.156487	-8724.13
-0.22855	13184.3	-0.152963	-9502.97
-0.228399	13126.8	-0.149372	-10267.6
-0.228149	13031.3	-0.145715	-11016.4
-0.227798	12898.1	-0.141994	-11749
-0.227348	12727.4	-0.138211	-12461.5
-0.226797	12518.9	-0.134368	-13150.3
-0.226148	12273.2	-0.130465	-13814.6
-0.225399	11991.4	-0.126505	-14452.8
-0.224551	11673.8	-0.12249	-15062.9
-0.223605	11320.9	-0.118421	-15643.6
-0.22256	10933.6	-0.1143	-16191.7
-0.221418	10512.8	-0.110129	-16708.8
-0.220179	10059.3	-0.105909	-17193.7
-0.218843	9574.55	-0.101644	-17639.1
-0.217412	9060.25	-0.0973331	-18043.1
-0.215884	8516.42	-0.09298	-18404.8
-0.214263	7942.86	-0.0885861	-18722.1
-0.212547	7342.08	-0.0841533	-18995.9
-0.210738	6715.66	-0.0796836	-19225.5
-0.208836	6064.68	-0.0751789	-19405.8
-0.206843	5391.17	-0.0706413	-19533.4
-0.20476	4696.72	-0.0660727	-19607.7
-0.202586	3982.77	-0.0614751	-19629.7
-0.200324	3250.84	-0.0568505	-19596.2
-0.197973	2502.53	-0.052201	-19503.9
-0.195536	1739.63	-0.0475286	-19351.9
-0.193013	963.853	-0.0428354	-19138.7
-0.190406	176.216	-0.0381233	-18861.3
-0.187715	-621.947	-0.0333946	-18517.6
-0.184941	-1428.25	-0.0286512	-18107.3
-0.182087	-2239.91	-0.0238952	-17630.1
-0.179152	-3056.53	-0.0191288	-17085.8
-0.176139	-3875.74	-0.0143539	-16475.2
-0.173049	-4693.98	-0.00957277	-15801.1
-0.169883	-5510.56	-0.00478744	-15068.8
-0.166642	-6323.96	1.39977E-17	-14290.3
-0.163328	-7132.33	0.00469358	-13483.2
-0.159943	-7933.3	0.00938518	-12659.6

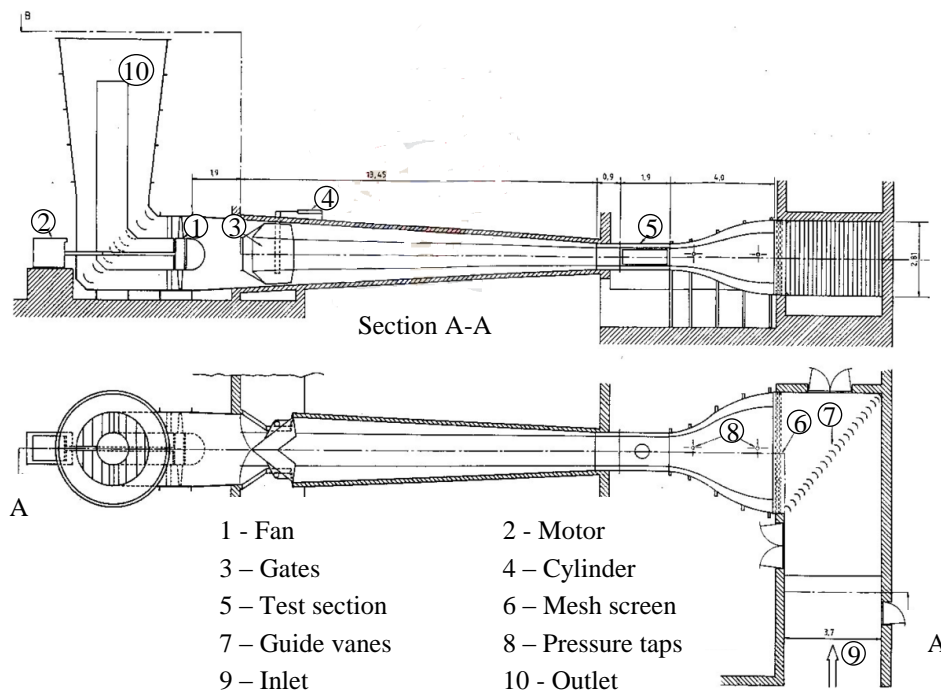
<b>x-Position [m]</b>	<b>Static Pressure [Pa]</b>	<b>x-Position [m]</b>	<b>Static Pressure [Pa]</b>
0.0140728	-11833	0.17077	-5925.69
0.0187545	-11024.9	0.17389	-5921.81
0.0234283	-10257.8	0.176936	-5917.64
0.0280923	-9551.71	0.179905	-5913.05
0.0327443	-8921.44	0.182797	-5907.93
0.0373826	-8375.74	0.185609	-5902.17
0.0420051	-7916.23	0.188341	-5895.69
0.0466099	-7537.76	0.190993	-5888.43
0.0511951	-7230.53	0.193561	-5880.36
0.0557587	-6983.04	0.196046	-5871.5
0.0602987	-6783.89	0.198447	-5861.84
0.0648134	-6623.09	0.200761	-5851.39
0.0693007	-6493.69	0.20299	-5840.42
0.0737588	-6390.68	0.20513	-5828.95
0.0781858	-6309.4	0.207182	-5817.01
0.0825798	-6245.08	0.209144	-5804.71
0.0869391	-6194.74	0.211017	-5792.16
0.0912616	-6155.82	0.212798	-5779.44
0.0955457	-6125.2	0.214487	-5766.65
0.0997895	-6100.35	0.216084	-5753.89
0.103991	-6079.12	0.217587	-5741.24
0.108149	-6061.1	0.218996	-5728.79
0.112261	-6045.43	0.220311	-5716.69
0.116326	-6031.09	0.221531	-5705.04
0.120342	-6018.01	0.222655	-5693.9
0.124308	-6006.07	0.223683	-5683.38
0.12822	-5995.21	0.224615	-5673.6
0.132079	-5985.41	0.225449	-5664.63
0.135882	-5976.62	0.226186	-5656.65
0.139628	-5968.78	0.226826	-5649.75
0.143315	-5961.83	0.227367	-5643.97
0.146941	-5955.66	0.227811	-5639.46
0.150548	-5950.19	0.228156	-5636.3
0.154089	-5945.31	0.228403	-5634.57
0.157564	-5940.92	0.228551	-5635.67
0.160971	-5936.9	0.2286	-5637.61
0.164309	-5933.11		
0.167576	-5929.42		

## Appendix C: Wind tunnel experiment

This appendix contains information pertaining to the wind tunnel test facility used and the procedure for obtaining data. The wind tunnel under consideration here is a suction type tunnel located at the University of Stellenbosch. The tunnel has the capacity to generate wind speeds of up to  $V = 90$  m/s through the use of a 373kW fan. Specifications of the wind tunnel test facility and the general facility layout is provided in Table C.1 and Figure C.1 respectively.

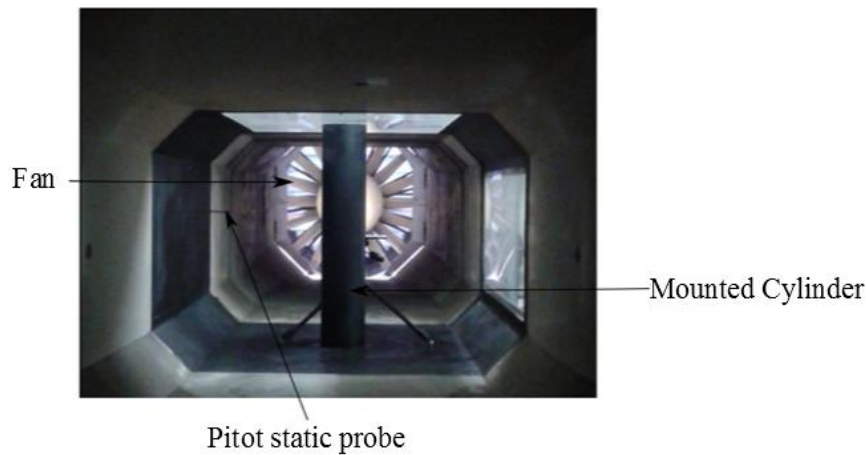
**Table C.1: Wind tunnel dimensions**

Main section	Sub-section	Specification
Inlet	Initial inlet area [m <sup>2</sup> ]	10.6
	Nozzle inlet area [m <sup>2</sup> ]	12.3
	Height [m]	1
Test section	Width [m]	1.4
	Length [m]	1.9
	Cross sectional area [m <sup>2</sup> ]	1.4
Diffuser	Length [m]	15.35
Fan	Diameter [m]	2.7
	Motor [kW]	373



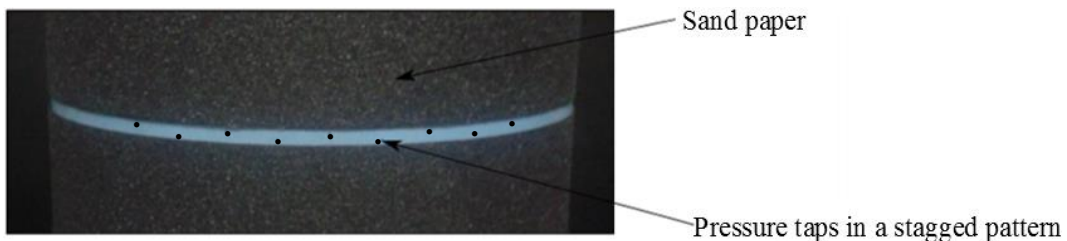
**Figure C.1: Wind tunnel layout (du Buisson, 1988)**

Experiments were conducted with a  $d = 200$  mm diameter cylindrical PVC pipe ( $k_s = \sim 7 \mu\text{m}$ ) spanning the whole test section height (Figure C.2) resulting in a blockage ratio of 0.1429.



**Figure C.2: Mounted cylinder**

In order to measure pressure along the cylinder circumference twenty-one 1 mm diameter holes are drilled with a spacing of  $a = 9^\circ$  between each hole along with a vertically staggered off-set of 2 mm between holes in order to limit interference between holes. Furthermore when sand paper (or meridional ribs) is fixed to the cylinder surface two paper sections are used with one section just above the upper most pressure taps and another section just below the bottom most pressure taps as shown in Figure C.3.

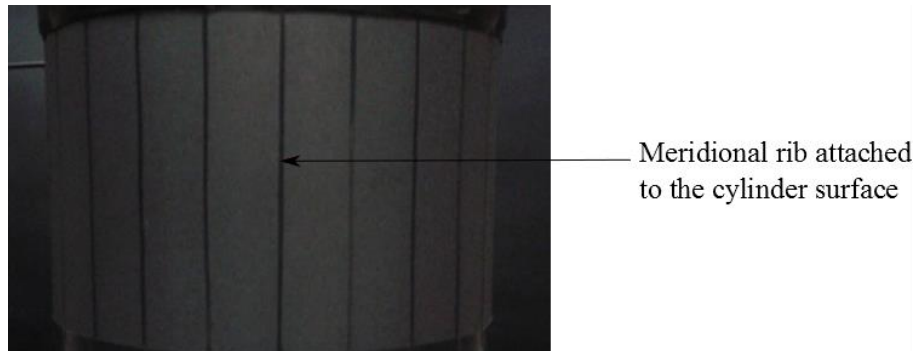


**Figure C.3: Sand paper applied to the cylinder surface**

The latter is based on a procedure followed by Cüven et al. (1980) who also applied sand paper roughening to cylinders. This spacing of the sand paper below and above the pressure taps is mainly done in order to avoid potential blockage of pressure taps through misaligning the paper and potential shifting of the paper once air is forced past the cylinder.

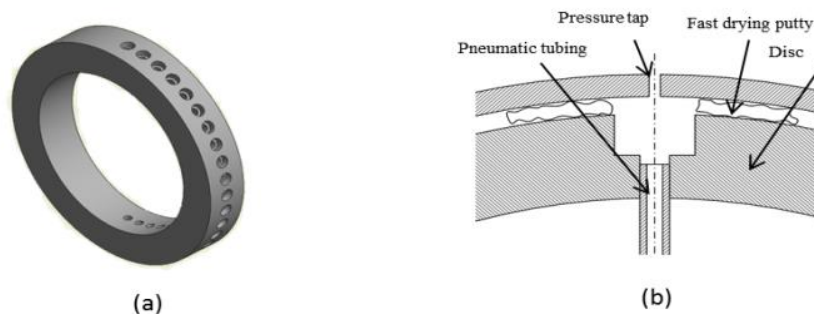
In addition to the sandpaper, ribs were also attached to the cylinder surface. The ribs were constructed from smooth insulation tape approximately 0.4 mm in height and cut to the required rib width. In order to ensure that the ribs are equally spaced and placed accurately on the cylinder surface such that the first rib is aligned with the cylinder centreline it was decided to first apply the ribbed

structures on a paper sheet and follow a similar procedure as the sand paper case when adding the ribs to the cylinder surface itself. Figure C.4 shows an example of the ribs attached to the paper and subsequently the cylinder. Furthermore to ensure that the surface roughness of the paper ( $\sim 4.58 \mu\text{m}$ ) itself does not impede on the results a pressure measurement with only the paper attached to the cylinder was measured and subsequently used as the smooth case for the rib investigations.



**Figure C.4: Ribs applied to the cylinder surface**

Furthermore in order to ensure no misalignment or leakage with regard to pressure measurements the pneumatic tubes of each pressure tap was connected to a PVC disc as shown in Figure C.5. The PVC disc is then fixed to the cylinder through using a combination of fast drying putty and Prestick® such that there is no leakage between the disc and the cylinder surface itself effectively creating an airtight seal.



**Figure C.5: PVC disc: (a) Disc; (b) Disc attached to the cylinder surface (Hill, 2014)**

Furthermore pressure taps are only drilled along one half of the cylinder ranging from the windward stagnation ( $0^\circ$ ) point to the downstream centre of the cylinder at  $180^\circ$ . With the latter setup it is assumed that the flow around the cylinder is symmetrical, which is a reasonable assumption when considering the fairly symmetrical behaviour of measured flows past infinite cylinders in Figure 3.7 (c) and the fact that in the experimental setup three dimensional effects play no role.

Pressure measurements are ultimately achieved through routing the pneumatic tubes from each pressure tap via a twenty-way FCO 91 Mk II multiplexer to a pressure transducer. The pressure transducer outputs a voltage which is then



recorded by a two channel DAQ system connected to a computer. An additional pressure transducer connected to a pitot static probe in the test section is also utilized to measure velocity in the test section. Furthermore prior to conducting experiments the pressure transducers were calibrated against a Van Essen 5000 Betz manometer in order to convert the voltage reading to a usable pressure value.

The general test procedure followed is summarized as follows:

- Secure the cylinder in the test section
- Apply the desired surface roughness to the cylinder surface, i.e. attach the desired sand paper or ribbed paper
- Ensure that the first pressure tap (hole) is correctly aligned such that the first measurement point represents the upstream stagnation point
- Close and secure the test section wall
- Set the variable speed drive to the desired wind speed
- Provide sufficient time for the system to settle and record the pressure of all 21 pressure taps.

Additional data measured during testing is now provided for completeness and can be regarded as complimentary data for section 3.6.

**Table C.2: Rib geometries investigated**

Rib case #	Rib height, $k$ [mm]	Rib Width, $b$ [mm]	$b/k$	Rib spacing, $a$ [mm]	$k/a$
1	0.4	1	2.5	26.24	0.01526
2	0.4	6	15	26.40	0.01515
3	0.4	13.12	32.8	26.24	0.01524

**Table C.3: Data for ribbed cases and smooth case with paper,  $Re = 3.3 \times 10^5$** 

	Rib case 1	Rib case 2	Rib case 3	Smooth paper (4.58 $\mu\text{m}$ )
Degrees	$C_p$	$C_p$	$C_p$	$C_p$
0	0.979785	0.943025	0.947517	1.002793
9	0.902772	0.893874	0.877794	0.896348
18	0.909598	0.905259	0.892912	0.911049
27	0.30304	0.32441	0.280569	0.216715
36	-0.0756	-0.02281	-0.08525	-0.33765
45	-0.61463	-0.71881	-0.60365	-0.91493
54	0.325433	-0.72066	0.296228	-0.54863
63	-1.31148	-1.43455	-1.33457	-1.90996
72	-1.40311	-1.3428	-1.35927	-2.23914
81	-1.23903	-1.19591	-1.24964	-2.22681
90	-0.75315	-0.68208	-0.7234	-2.06722
99	-0.47732	-0.52124	-0.54453	-1.15934
108	-0.46191	-0.47421	-0.47529	-0.76145
117	-0.46948	-0.46409	-0.46123	-0.82373
126	-0.48318	-0.48074	-0.47996	-0.73475
135	-0.49926	-0.50902	-0.49916	-0.66649
144	-0.5148	-0.5185	-0.49649	-0.61535
153	-0.50623	-0.49795	-0.4969	-0.5851
162	-0.50418	-0.51294	-0.4969	-0.5851
171	-0.5062	-0.51294	-0.4969	-0.5851
180	-0.5042	-0.51294	-0.4969	-0.5851

**Table C.4: Data for sand paper and smooth case,  $Re = 3.3 \times 10^5$** 

	Smooth PVC	40 Grit	60 grit	80 grit	100 grit
Degrees	$C_p$	$C_p$	$C_p$	$C_p$	$C_p$
0	0.993856	0.98265	0.987274	0.986108	0.985587
9	0.913851	0.93333	0.956747	0.937288	0.886767
18	0.912642	0.934333	0.957540	0.938299	0.898888
27	0.253558	0.37419	0.376038	0.371149	0.216842
36	-0.19681	-0.00914	-0.00656	-0.03898	-0.20527
45	-0.74012	-0.44902	-0.43525	-0.46306	-0.69809
54	0.299484	-	-	-	-
63	-1.71683	-0.99356	-1.0839	-1.16357	-1.40809
72	-1.9528	-1.04878	-1.13643	-1.2919	-1.54032
81	-2.01603	-0.75584	-0.87773	-1.12848	-1.39308
90	-1.7542	-0.59798	-0.60596	-0.76351	-0.82502
99	-0.75353	-0.52576	-0.54569	-0.62073	-0.63894
108	-0.4439	-0.51777	-0.5315	-0.60147	-0.5519
117	-0.43364	-0.5214	-0.53938	-0.59255	-0.54795
126	-0.45098	-0.52281	-0.55738	-0.5918	-0.54118
135	-0.45201	-0.54012	-0.58093	-0.61785	-0.55361
144	-0.45402	-0.55555	-0.56243	-0.6195	-0.56697
153	-0.4607	-0.55412	-0.59967	-0.60904	-0.57784
162	-0.4607	-0.55412	-0.59967	-0.60904	-0.57784
171	-0.4607	-0.55412	-0.59967	-0.60904	-0.57784
180	-0.4607	-0.55412	-0.59967	-0.60904	-0.57784

**Table C.5: Data for sand paper and smooth case,  $Re = 4.3 \times 10^5$** 

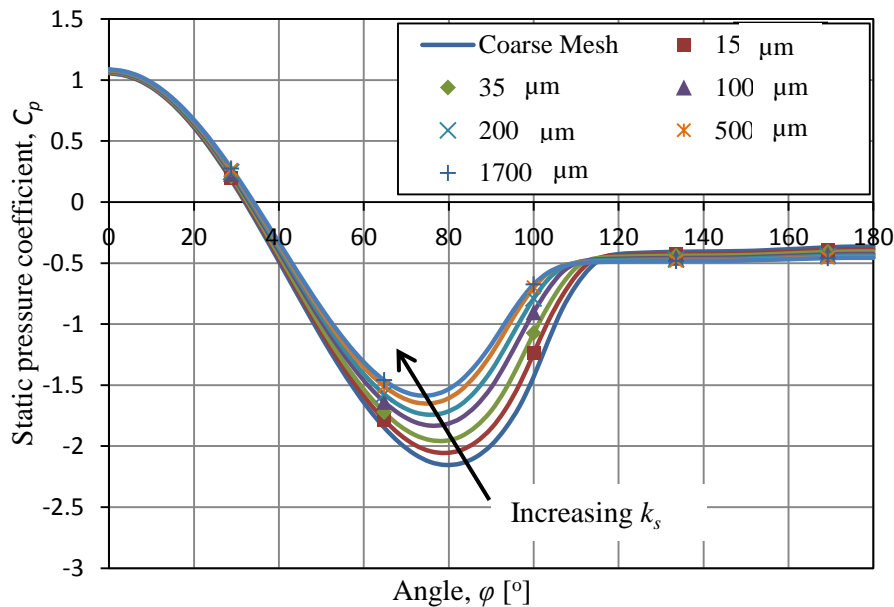
	Smooth PVC	40 Grit	60 grit	80 grit	100 grit
Degrees	$C_p$	$C_p$	$C_p$	$C_p$	$C_p$
0	0.996739	0.995504	0.996206	0.995052	0.982687
9	0.93957	0.946209	0.952325	0.948583	0.91996
18	0.934645	0.943346	0.944592	0.943753	0.937307
27	0.260115	0.400932	0.38349	0.383661	0.278824
36	-0.20814	-0.01454	-0.01227	-0.02113	-0.12023
45	-0.74345	-0.38174	-0.44694	-0.46958	-0.55163
54	0.176439	0.176763	0.17475	-0.47459	0.174605
63	-1.67317	-0.9836	-1.08311	-1.13771	-1.18761
72	-1.92395	-0.9815	-1.13143	-1.25996	-1.27176
81	-1.96035	-0.73651	-0.84909	-1.09476	-0.97677
90	-1.64675	-0.57508	-0.63254	-0.73236	-0.66555
99	-0.666	-0.53672	-0.57136	-0.64927	-0.59954
108	-0.47004	-0.5334	-0.56021	-0.62525	-0.56416
117	-0.47022	-0.54357	-0.57587	-0.62758	-0.57656
126	-0.48058	-0.55962	-0.57887	-0.63515	-0.57157
135	-0.48945	-0.57977	-0.61186	-0.65464	-0.59464
144	-0.49655	-0.57728	-0.61108	-0.64796	-0.58959
153	-0.49291	-0.57617	-0.61342	-0.65807	-0.60176
162	-0.49291	-0.57617	-0.61481	-0.65903	-0.60176
171	-0.49291	-0.57617	-0.61574	-0.65903	-0.58959
180	-0.49291	-0.57617	-0.61574	-0.65903	-0.60176

## Appendix D: Applying $k_s$ to an arbitrary mesh

In order to substantiate the statement Fluent® made about the rough wall model being applicable on arbitrary fine meshes an arbitrary coarse BL mesh was generated. The edge sizing and cell count for the coarse mesh is given in Table D.1. Figure D.1 shows the results obtained from the coarse mesh. The data shows a similar increasing trend for the  $C_p$  curve which is again consistent with observations made by Niemann (1971) and Cüven et al. (1980). This result is extremely favourable since it implies that a coarse mesh can be used to efficiently and effectively investigate pressure distribution trends due to alterations around a cylinder without the need for a computationally expensive mesh. Furthermore comparing Figure D.1 to Figure 3.14 the only major difference is an upward shift in the general  $C_p$  curve.

**Table D.1: Coarse mesh edge sizings**

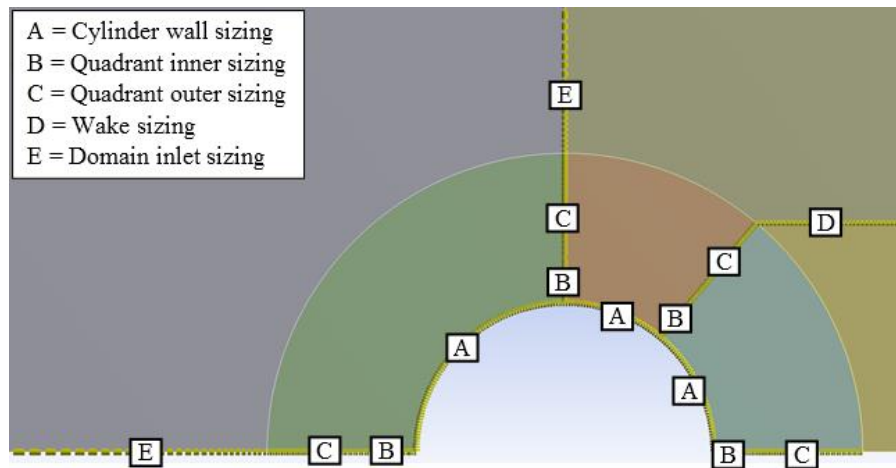
Edge	Element size (m)	Bias
A	0.014363	-
B	0.0028	8
C	0.0064	-
D	0.0075	-
E	0.04	16
Total cell count	63 427 cells	



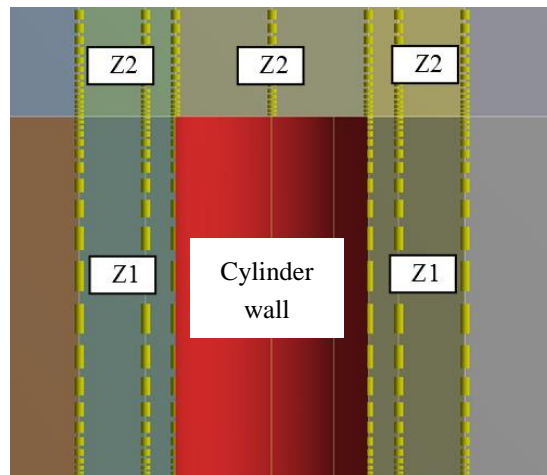
**Figure D.1: Effect of surface roughness using a coarse mesh**

## Appendix E: Mesh information for 3-D simulations

This section contains edge sizing details as well as total cell counts used for the cases investigated in Chapter 4. Furthermore there is a necessary additional increase in cell count once the inlet height is added to the solid finite cylinder in order to retain the distances from domain boundaries. In addition the edges referred to in the tables are defined in Figure E.1 with the regions defined in Figure 3.2.



(a)



(b)

**Figure E.1: Edges used for sizing: (a) x-y plane; (b) z-x plane**

**Table E.1: Domain sizing for solid finite cylinder**

Description (region)	Boundary condition	Distance from cylinder centre
Inlet (A)	Velocity inlet	6D
Outlet (B)	Pressure outlet	14D
Domain Top (C)	Slip-wall	6D
Mid-plane Domain (D)	Symmetry	-
Cylinder Wall (E)	No-slip Wall	-
Boundary mesh	-	2D
Domain Bottom	No-slip Wall	-
Cylinder height	-	1.88D
Domain height	-	4D

**Table E.2: Mesh edge sizing for solid finite cylinder**

Edge	Element size (m)	Bias
A	0.004788	-
B	0.0015	8
C	0.0042	-
D	0.025	-
E	0.04	26
Z1	0.008	12
Z2	0.008	12
Total cell count	8 779 920 cells	

**Table E.3: Domain sizing for hollow finite cylinder with an inlet height, fine mesh**

Description (region)	Boundary condition	Distance from cylinder centre
Inlet (A)	Velocity inlet	6D
Outlet (B)	Pressure outlet	14D
Domain Top (C)	Slip-wall	6D
Mid-plane Domain (D)	Symmetry	-
Cylinder Wall (E)	No-slip Wall	-
Boundary mesh	-	2D
Domain bottom	No-slip Wall	-
Cylinder height	-	1.88D
Domain height	-	4D
Inlet height	-	~0.214D

**Table E.4: Mesh edge sizing for hollow finite cylinder with an inlet height, fine mesh**

Edge	Element size (m)	Bias
A	0.004788	-
B	0.0015	8
C	0.0042	-
D	0.025	-
E	0.04	26
Z1	0.008	12
Z2	0.008	12
Inlet height	0.003	6
Total cell count	10 427 424 cells	



**Table E.5: Domain sizing for hollow finite cylinder with an inlet height, coarse mesh**

Description (region)	Boundary condition	Distance from cylinder centre
Inlet (A)	Velocity inlet	6D
Outlet (B)	Pressure outlet	10D
Domain Top (C)	Slip-wall	6D
Mid-plane Domain (D)	Symmetry	-
Cylinder Wall (E)	No-slip Wall	-
Boundary mesh	-	2D
Domain bottom	No-slip Wall	-
Cylinder height	-	1.88D
Domain height	-	4D
Inlet height	-	~0.214D

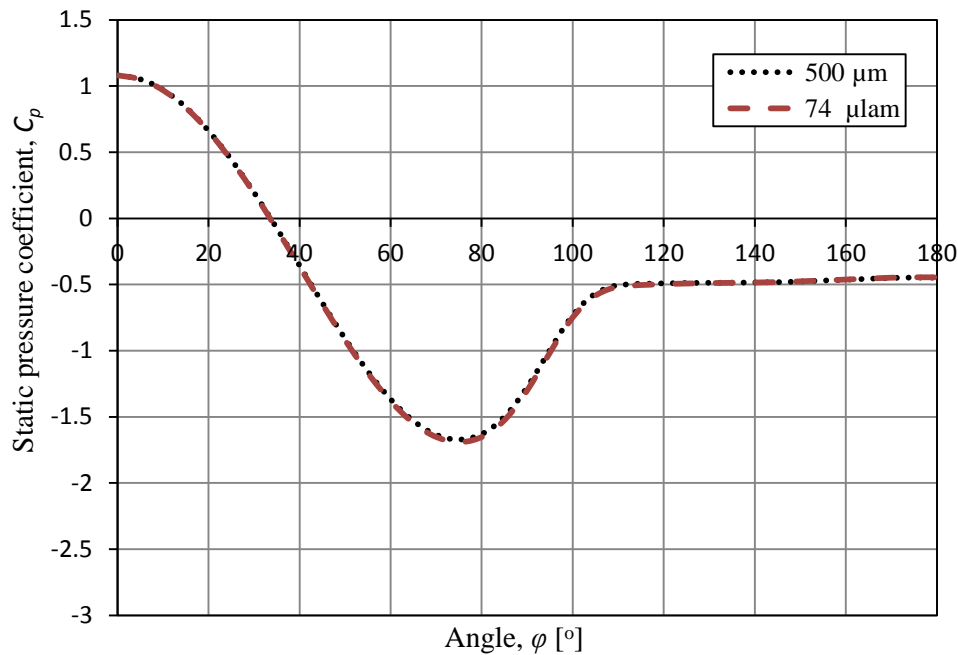
**Table E.6: Mesh edge sizing for hollow finite cylinder with an inlet height, coarse mesh**

Edge	Element size (m)	Bias
A	0.017954	-
B	0.0026	8
C	0.008	-
D	0.025	-
E	0.06	26
Z1	0.014	12
Z2	0.014	12
Inlet height	0.006	6
Total cell count	1 623 206 cells	

## Appendix F: Effect of using $\mu_{lam}$ instead of $k_s$

This section investigates the use of specifying an increased  $\mu_{lam}$  in the wall adjacent cells (i.e. the technique developed in section 3.3.5) as opposed to the  $k_s$  technique (i.e. the technique developed in section 3.3.3) used in Chapter 4. Furthermore since the coarse model developed in section 4.3 provided an adequate representation when surface roughening was applied it will be used in the current investigation. In addition the use of the coarse mesh will also lead to faster simulation execution compared to the fine mesh with significantly more cells.

In order to effectively investigate the effect of using  $\mu_{lam}$  rather than  $k_s$  the 2-D half cylinder model was used to generate similar  $C_p$  distributions as shown in Figure F.1. Since the 2-D distributions result in the same solution it is expected that the effect the individual parameters have on the  $C_p$  distribution at varying heights along a finite cylinder will also be similar.

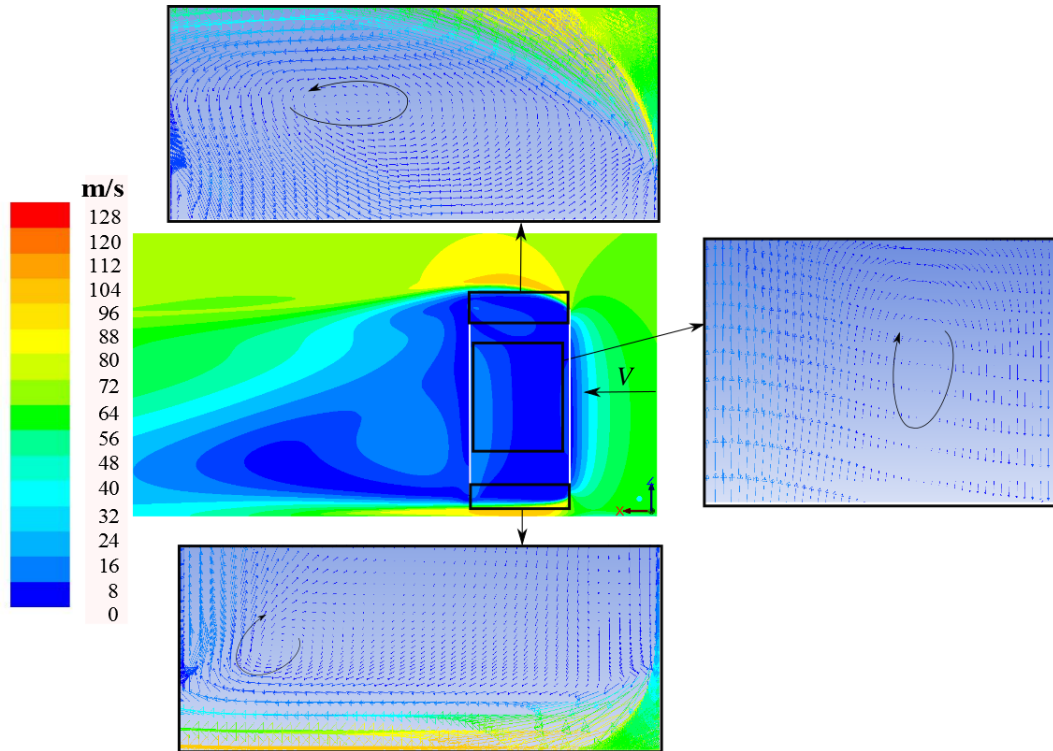


**Figure F.1: Matching  $C_p$  distributions for  $k_s$  and  $\mu_{lam}$**

The resulting velocity contours and vectors for the case of specifying  $\mu = 74\mu_{lam}$  can be found in Figure F.2 followed by the obtained pressure distributions measured at varying heights along the cylinder wall in Figure F.3.

Comparing Figure F.2 to Figure 4.15 it can be clearly seen that both methods result in similar velocity contours both in the windward and leeward region suggesting that the effect the  $\mu_{lam}$  method has on the pressure distribution is the same as the effect  $k_s$  has. Furthermore other flow phenomena such as the recirculation zone at the cylinder top end, small recirculation zone at the cylinder

bottom end and the larger recirculation zone inside the cylindrical structure are also similar to the  $k_s$  case.



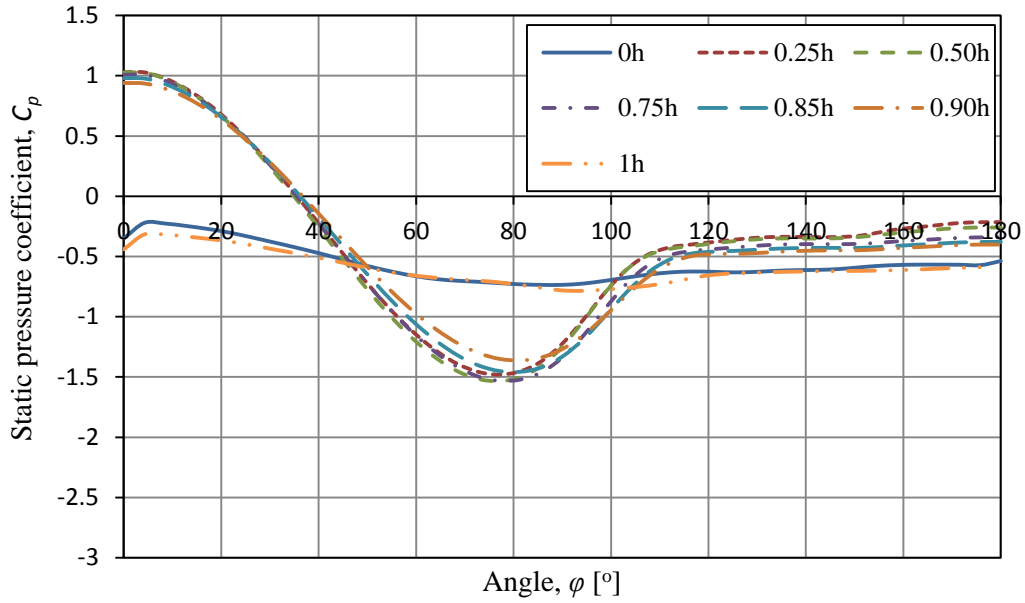
**Figure F.2: Velocity contours and vectors along the centreline for the coarse mesh using  $\mu = 74 \mu_{lam}$**

The  $\mu_{lam}$  method also seems to result in the same wake structure as in the  $k_s$  case. However, to more accurately assess this consider the obtained  $C_p$  distributions and the deviation plot in Figure F.3 and Figure F.4 respectively. Note that in this case the deviation is calculated according to:

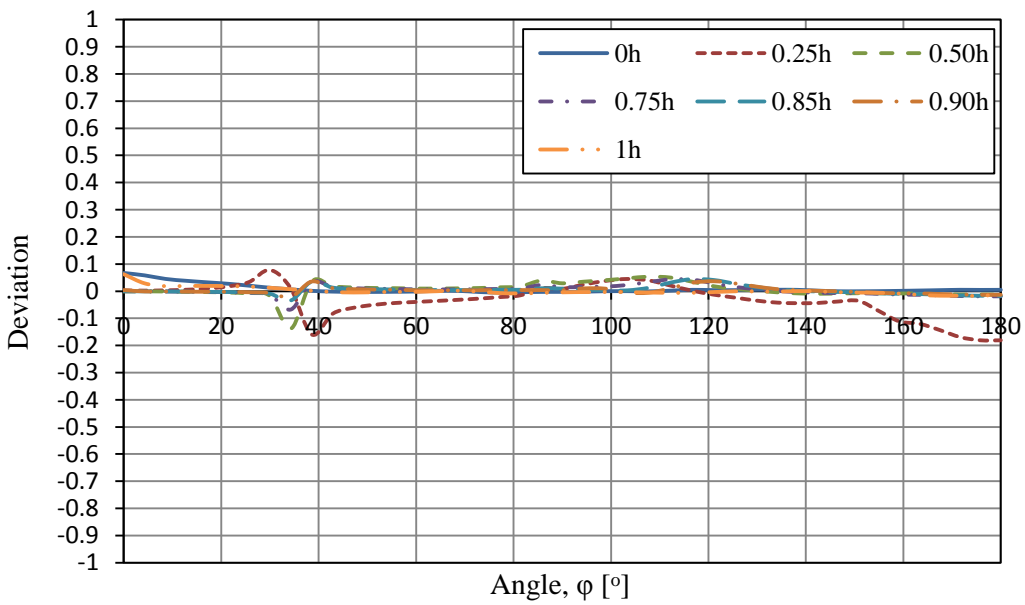
$$Deviation = \frac{(C_{p,78\mu_{lam}} - C_{p,500\mu m})}{C_{p,500\mu m}} \quad (F.1)$$

From the error plot it is clear that for all practical purposes the use of either  $\mu = 74\mu_{lam}$  or  $k_s = 500 \mu m$  result in exactly the same predicted pressure distributions.

Thus in conclusion it is shown that both the  $\mu_{lam}$  and  $k_s$  techniques result in the same pressure distribution and flow field predictions, if the 2-D model predicts similar  $C_p$  distributions, and can subsequently be considered as interchangeable.



**Figure F.3:**  $C_p$  distribution around a rough ( $\mu = 74 \mu_{lam}$ ) hollow finite cylinder using a coarse mesh



**Figure F.4:** Deviation plot for the rough hollow finite cylinder with  $\mu = 74 \mu_{lam}$  and  $k_s = 500 \mu m$